UNIVERSITÀ DELLA CALABRIA

UNIVERSITÀ DELLA CALABRIA
Dipartimento di Fisica

Dottorato di Ricerca in
Scienze e Tecnologie Fisiche, Chimiche e dei Materiali

CICLO
XXXII

Monte Carlo neutronic calculations for the design of VESPA shielding at the European Spallation Source

FIS/01 - FISICA SPERIMENTALE

Coordinatore: Ch.ma Prof.ssa Gabriella Cipparrone
Firma ____ [redacted]
Firma oscurata in base alle linee guida del Garante della privacy

Supervisore: Ch.mo Prof. Raffaele Giuseppe Agostino
Firma ____ [redacted] Firma oscurata in base alle linee guida del Garante della privacy

Supervisore: Ch.mo Prof. [redacted] Firma oscurata in base alle linee guida del Garante della privacy
Firma ____ [redacted]

Dottorando: Dott. Jimmy Scionti
Firma Firma oscurata in base alle linee guida del Garante della privacy

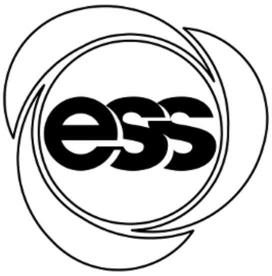

ess

Electra
Zelda

Contents

Abstract (in italiano) 1

Introduction 3

1 Monte Carlo simulations 5
- 1.1 Monte Carlo method . . . 5
- 1.2 Functions of a random variable . . . 7
- 1.3 Errors . . . 9
- 1.4 Variance reduction . . . 10
  - 1.4.1 Biasing the density function . . . 12
- 1.5 MCNP . . . 13
  - 1.5.1 Basic input file structure . . . 13
  - 1.5.2 Tallies . . . 14
  - 1.5.3 Variance reduction cards . . . 15
    - 1.5.3.1 Weight windows . . . 16
- 1.6 Dose . . . 17
  - 1.6.1 Transmittance through thick means . . . 21

2 European Spallation Source 22
- 2.1 The facility . . . 22
  - 2.1.1 Source and target . . . 22
  - 2.1.2 Target-Moderator-Reflector . . . 24
  - 2.1.3 Monolith . . . 25
  - 2.1.4 Bunker . . . 28
  - 2.1.5 Halls . . . 28

3 VESPA 31
- 3.1 Scientific case . . . 31
- 3.2 Instrument . . . 32
  - 3.2.1 Inside the bunker . . . 34
  - 3.2.2 Outside the bunker . . . 37
- 3.3 MCNP model . . . 39

4 Fictive neutron sources **44**
4.1 ESS source terms 44
4.2 Primary source term 48
4.2.1 Setting up the primary source term 50
4.3 Secondary fictive neutron source 53
4.3.1 Suitable positions 56
4.3.2 Angular binning 56
4.3.3 Secondary source term candidates 57
4.3.4 Benchmarks for selecting the secondary source term . 61
4.3.5 Selection of the secondary source term 63
4.3.6 Effects of a gamma source term 66

5 Beam-line Shielding **69**
5.1 Common Shielding Project 69
5.2 Geometry 70
5.2.1 Preliminary model 70
5.2.2 Common shielding model 76
5.2.3 Common shielding model without borated concrete . . 82
5.2.4 sFOC in closed configuration 82
5.2.5 Super-mirror for gamma doses 89
5.2.6 Proposed shielding design for VESPA 89
5.2.7 Heavy concrete layer 95
5.2.8 Guide gaps and steel activation 97

6 Heavy Shutter **104**
6.1 Beam attenuator 104
6.2 Geometrical constraints 104
6.3 Material selection 105
6.4 Model 106
6.5 Neutron and photon dose rates 107
6.6 Future studies 108

Conclusions **110**

Appendix A Fluence to dose conversion functions **112**

Appendix B Input materials **115**

List of Acronyms **118**

List of Figures **124**

List of Tables **125**

Bibliography **132**

Acknowledgements **133**

Abstract (ITA)

L'European Spallation Source (ESS) è la prossima più potente sorgente pulsata di neutroni al mondo, in costruzione a Lund, nel sud della Svezia.

Molti ambiti nella scienza e nell'industria beneficeranno della costruzione di ESS, come i prodotti farmaceutici, manifattura, biotecnologie, tecnologie informatiche, chimica, e così via. La facility produrrà neutroni da reazioni di spallazione, indotte da protoni ad alta energia, accelerati fino all'energia di 2 GeV e dunque convogliati a urtare un bersaglio rotante di tungsteno. I neutroni così prodotti passano attraverso un complesso sistema di moderazione e sono dunque convogliati alle stazioni sperimentali di una suite di strumenti, per mezzo di linee di fascio dedicate. Ogni strumento ha un stazione sperimentale unica al mondo, guide neutroniche e un design che sono concepiti e ottimizzati per un particolare campo di ricerca scientifica.

ESS sarà in grado di produrre neutroni con energie fino a quella del fascio di protoni incidente. Tali neutroni tanto energetici costituiscono un motivo di particolare attenzione per la radio-protezionistica. I neutroni rappresentano infatti un motivo di maggiore preoccupazione rispetto alle particelle cariche proprio a causa del fatto che non trasportano alcuna carica. Per questo motivo, non possono interagire con la materia per mezzo della forza coulombiana, che domina il meccanismo di perdita di energia per le particelle cariche. In particolare i neutroni lenti, di energia fino a pochi eV, sono tipicamente assorbiti dai nuclei atomici tramite reazioni di cattura radiativa, che portano all'emissione di raggi gamma. Similmente ai neutroni, i gamma non trasportano carica elettrica, ma il loro meccanismo di interazione nella materia differisce da quello dei neutroni, e dipende dal numero atomico Z del nucleo atomico [1].

Le radiazioni gamma e di neutroni sono entrambe oggetto principale di attenzione in facility neutroniche, a causa della loro maggior penetrabilità rispetto alle particelle cariche. In particolare, essere in grado di attenuare e schermare tale radiazione fino a limiti accettabile è un aspetto cruciale nel progetto ESS La schermatura radiologica di ogni componente della facility, dall'acceleratore fino alle linee di fascio, è un campo di studi e di progettazione essenziale a ESS.

Gli studi sulle schermature radiologiche possono essere considerate come studi di ottimizzazione. Infatti, l'obiettivo tipico è di ridurre una quantità

radiologica, in genere la dose, in certe particolari aree d'interesse, tramite la selezione di materiali appropriati. La scelta è vincolata alle capacità attenuanti dei materiali selezionati nei confronti della radiazione, ai costi e allo spazio disponibile che impone vincoli geometrici.

Gli studi descritti in questa tesi sono focalizzati sul design di una schermatura appropriata per la linea di fascio di VESPA, uno degli strumenti in costruzione a ESS. VESPA è una joint venture tra il Consiglio Nazionale delle Ricerche (CNR, in Italia) e lo Science and Technology Facilities Council (STFC, Regno Unito). L'acronimo VESPA sta per Spettrometro per Eccitazioni Vibrazionali tramite Analizzatore di grafite Pirolitica. Come il nome suggerisce, si tratta di un spettrometro ad alta risoluzione e ad ampio spettro, equipaggiato con un diffrattometro, completamente dedicato alla ricerca in-situ. Lo strumento sarà capace di produrre simultaneamente dati strutturali e sulla dinamica dei legami chimici, sulle interazioni intra-molecolari e inter-molecolari su sulle dinamiche vibrazionali.

VESPA è uno strumento lungo $\sim 60\,\mathrm{m}$, con visibilità diretta del moderatore di ESS. La maggior parte dello strumento, circa $\sim 45\,\mathrm{m}$, sarà costruita in un'area che sarà di libero accesso per tecnici, scienziati, personale ESS e così via. Per questa ragione, la radiazione dallo strumento deve essere fortemente attenuata da una struttura schermante adeguata, così da rappresentare un rischio radiologico.

Gli studi per la schermatura di VESPA presentati in questa tesi sono stati prodotti dal codice Monte Carlo per trasporto MCNP e tramite codici ausiliari come CombLayer e ADVANTG. Lo studio ha beneficiato del progetto Common Shielding a ESS, che punta a standardizzare le strutture schermanti per tutti gli strumenti partecipanti, così come a produrre un squadra di lavoro comunque per promuovere la discussione e la validazione dei risultati prodotti.

Parte di questa tesi punta a descrivere il metodo Monte Carlo, con particolare attenzione per le tecniche di riduzione della varianza, specialmente quelle che sono state usate per i calcoli MCNP qui presentati. Un grossa parte della tesi è dedicata alla caratterizzazione delle sorgenti usate nelle simulazioni. La schermatura per VESPA è stata determinata dagli studi sulle mappe dei tassi di dose neutronica e fotonica. Il design proposto, in conformità con i requisiti del progetto Common Shielding e i requisiti sui livelli di dose, è presentato al termine della tesi. Un ultimo capitolo della tesi è addendum che presenta le simulazioni preliminari per il design di altro componente essenziale per lo strumento.

Abstract (ENG)

The European Spallation Source (ESS) is the next world's most powerful pulsed neutron source, under construction in Lund, in the south of Sweden. Many scientific and industrial fields will benefit from ESS, like pharmaceutical drugs, manufacturing, biotechnology, information technology, chemistry, and so on. The facility will produce neutrons by spallation reactions, induced by high energetic protons, accelerated up to the energy of 2 GeV and eventually conveyed to impinge on a rotating tungsten target. Neutrons will then pass through a complex moderator system and will be delivered to the experimental stations of a suite of instruments through dedicated beam-lines. Each instrument has a unique experimental station, neutron guide and design that are optimized and conceived for a specific scientific research field.

ESS will be capable of producing neutrons with energies up to that of the incident proton beam. Such high energetic neutrons constitute a matter of particular care for radiological protection purposes. In fact, neutrons represent a higher concern respect to charged particles due to the fact that they carry no electric charge. Therefore, they can't interact with matter by mean of the coulomb force, which dominates the energy loss mechanism for charged particles. In particular slow neutrons, of energy up to a few eV, are likely to be absorbed by the atomic nuclei by radiative capture reactions, that lead to the emission of gamma particles. Similarly to neutrons, gammas carry no electric charge, but their interaction mechanisms in matter differ from those of neutrons, and depend on the atomic number Z of the nuclei [1].

Both neutron and gamma radiations are an issue for radiological protection in neutron facilities, due to their higher penetrability respect to charged particles. In particular, being able to attenuate and shield that radiation down to acceptable limits is a crucial aspect within the ESS project. The radiological shielding of each component of the facility, from the accelerator down to the beam-lines, is an essential matter of studies and investigations at ESS.

Shielding studies can be thought as a type of optimization studies. In fact, the typical purpose is to minimize a radiological quantity, usually the dose, in some particular area of interest, by choosing appropriate materials.

The choice is bound to the attenuating capability of the selected materials for the given radiation, to the cost and to the available space that set geometrical constraints.

The studies described in this thesis are focused on the design of an appropriate shielding for the beam-line of VESPA, one of the instruments under construction at ESS. VESPA is a joint venture between Consiglio Nazionale delle Ricerche (CNR, Italy) and Science and Technology Facilities Council (STFC, United Kingdom). The acronym VESPA stands for Vibrational Excitation Spectrometer using Pyrolytic-graphite Analyser. As the name suggest, it is a high-resolution broadband chemical spectrometer, enhanced with diffraction capabilities, fully dedicated for in-situ research. It will be capable of providing simultaneous dynamic and structural data on chemical bondings, intra-molecular and inter-molecular interactions and on the vibrational dynamics.

VESPA is a $\sim 60\,\mathrm{m}$ long straight instrument, in line of sight with ESS moderator. Most of the instrument, about $\sim 45\,\mathrm{m}$, will be built in an area that will be frequently accessed by workers, scientists, ESS personnel and so on. Therefore, the radiation coming from the instrument has to be strongly attenuate by an adequate shielding structure, so to not constitute a radiological hazard.

The studies for the shielding of VESPA presented here, were performed by mean of the Monte Carlo transport code MCNP and auxiliary codes like CombLayer and ADVANTG. The investigation benefited from the Common Shielding Project at ESS, that aims to standardize the shielding structures for all the participating instruments, as well as to provide a common teamwork for discussing and validating the investigations.

Part of this thesis aims to describe the Monte Carlo method, with a particular care for the variance reduction techniques, especially those that were used in the MCNP calculations. A large part of the thesis is related to the characterization of the sources used in the simulations. The shielding for VESPA is investigated through studying the neutron and photon dose rate maps. The proposed design, in compliance with the Common Shielding requirements and the dose requirements, is given toward the end of the thesis. The last chapter of the thesis is an addendum about the early simulations aimed to design an essential component of the instrument.

Chapter 1

Monte Carlo simulations

The purpose of this chapter is to briefly introduce the methodology and the basics of the tools used as well as the quantities investigated in the present work.

Most of this chapter is inspired by the book by Lewis and Miller [2], as well as by the book by Haghighat [3] and by the MCNP [4] user manual [5]. The sections on the radiation dose are taken mainly from the ICRP publication 116 [6], the book from Attix [7] and the book by Knoll [1]. Additional references are given throughout the text when needed.

1.1 Monte Carlo method

In its simplest form, a Monte Carlo method is a statistical process that makes use of random sampling in order to provide numerical estimations of unknown quantities [3]. In Physics, it consists of simulating and transporting a finite number of particles so to estimate some quantity of interest [2]. Pseudo random number generators are used to sample appropriate probability distributions for the entire history of each particle.

In order to perform a Monte Carlo simulation, the user has to provide a complete geometry, as well as the detailed material composition and the prescription of the particle source for the given problem. When generating a particle from the source, a set of random numbers defines its initial position, energy, trajectory, type, etc, following suitable distributions and user defined constraints. In fact, some of these quantities might not be needed, depending on the source itself. For example, if the simulation is set so that all source particles have the same energy, then no random number is needed in order to determine such quantity. On the other hand, if the source is defined so to produce particles according to a given energy spectrum, then a random number is generated to sample that spectrum and the outcome is set as the initial energy for the particle. The same mechanism is used for determining the position, in case of a particle being emitted by a surface or in a volume, as well as all the other initial parameters: they are all sampled according to the user distributions (if defined) or an uniform distribution (otherwise).

Once the initial parameters of the new particle are set, the entire particle history is followed till its death (by absorption, by escaping the geometry, etc). The history of a particle is a collection of events which are determined using other pseudo random numbers and the transport data.

Already among the initial parameters, the mean free path till the next event is also determined using the total cross section σ in the particular material means and the associated probability distribution [2]. Such cross section σ is the sum of all the cross sections σ_i related to all the possible events that can occur according to the particle and the means. It can be written as

$$\sigma = \sum_{i}^{N} \sigma_i. \tag{1.1}$$

In order to determine which event occurs after travelling the mean free path, a unit line is divided into intervals of length σ_i/σ and a random number ξ is generated uniformly between 0 and 1. The outcome for ξ uniquely selects the event by comparing its value to the unit line, as sketched in figure 1.1 [2].

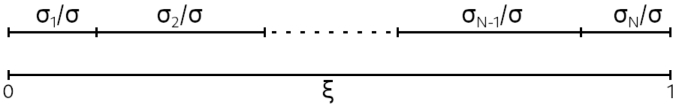

Figure 1.1: A uniformly generated random number selects the type of event that takes place, according to where its value lies in a unit line.

Depending on the type of interaction, a set of subsequent physical quantities has to be determined. If it is a scattering reaction, for example, quantities like the scattering angle, direction, energy and momentum after the collision will be determined. If the interaction is a capture, the history of that particle terminates. In the case in which the event can lead to the emission of secondary particles, other random numbers sample the probability of that to happen and also the initial set of parameters of such particles, according to the physical conditions of the reaction.

In MCNP code, which is the main Monte Carlo code used in this thesis that will be more extensively described later in this chapter, the secondary particles are temporarily stored while the history of the parent particle is being followed until its death. When that happens, the code starts following the history of the last born secondary particle until its death, using the very same procedure described so far. In the moment in which the latter dies, the code starts following the next secondary particle of the same progeny. This mechanism goes on sequentially, following a LIFO logic, until the stack of secondary particles is empty. If any secondary particle happens to produce other daughter particle, then the history of the latter is followed using the same procedure described so far [8].

For any particle history, some quantity requested by the user is tallied. A Monte Carlo simulation relies on a repetitive random sampling in order to provide results with a small statistical uncertainty of those quantities [3]. Such process may require large simulation times depending on the level of detail and complexity of the simulation, as well as on the available computational power. When simulating a physical experiment, the simulation can be set up so to mitigate that demand. It is possible, for example, to set up the particle source to be a line, thus avoiding the need of sampling the particle emission angle, or to set the source to generate mono-energetic particles, so to avoid sampling the initial energy.

In some cases, the complexity of the experiment can't be further reduced and might require excessively long computational times. To overcome such difficulty, additional techniques can be used. They are called *variance reduction techniques* and have the purpose to alter the random sampling in favour of a semi-deterministic sampling. When they are used, the simulation is said to be a *non-analog* simulation, in contrast with the random sampling procedure for which the term *analog* is used.

1.2 Functions of a random variable

The quantity x that a Monte Carlo simulation estimates is a *random variable.* It is a variable which assumes particular values with frequencies given by an underlying probability density function. Examples of that quantity can be flux, current, reaction rate and so on, if the calculation has the purpose to estimate some physical quantity. The underlying function must exist for each of those quantities and for each Monte Carlo simulation, but usually it's not determined exactly unless the problem is so simple that it can be solved analytically.[2].

Each particle history in a Monte Carlo simulation carries a contribution x_n to the quantity x. If the simulation generates N particle histories, the simulation will return the mean value for such quantity as

$$\widehat{x} = \frac{1}{N}\sum_{n}^{N} x_n. \tag{1.2}$$

It can be rewritten in terms of the *probability density function* f as

$$\widehat{x} = \sum_{n'}^{N'} f(x_{n'})x_{n'}. \tag{1.3}$$

where now the sum is weighted over the subset of all distinct values x'_n, which are weighted by the frequency f with which they appears.

In the ideal case of a simulation that generates an infinite number of particles, the sum over each contribution can be replaced by an integral. The set of frequencies f is replaced by a function, called *probability density function* $f(x)$, which is defined by the following equation

$$P(x^- < x < x^+) = \int_{x^-}^{x^+} \mathrm{d}x\, f(x), \tag{1.4}$$

where P is the probability that the random variable x assumes values in a range $[x^-; x^+]$.

Depending on the type of problem, the quantity x can assume only particular values. The complete set of all the possible values is the domain $\mathcal{D}$ of the quantity.

The requirement that the probability P of x assuming any value in its domain $\mathcal{D}$ shall be equal to 1 [9], leads to the following normalization requirement for the probability density function $f(x)$

$$P(x \in \mathcal{D}) = \int_{\mathcal{D}} \mathrm{d}x\, f(x) = 1. \tag{1.5}$$

If the probability density function for the specific quantity of interest x is known, it is not necessary to use a Monte Carlo calculation in order to estimate its mean value as in equation 1.2. It is possible, instead, to calculate its *true mean value*, defined as

$$\overline{x} = \int_{\mathcal{D}} \mathrm{d}x\, x f(x). \tag{1.6}$$

A good Monte Carlo simulation is not affected by systematic errors that would bias the mean values. It means that the outcomes are expected to be equal to the true mean values. In a more general case, the *expectation value* $\mathbb{E}[x]$ for a quantity x is defined as [9]

$$\mathbb{E}[x] = \int_{\mathbb{D}} \mathrm{d}x\, x f(x), \tag{1.7}$$

which clearly coincides with the definition of the true mean value given in equation 1.6.

A priori, we could require that each of the contributions x_n that make up the simulation outcome is equal to the true mean value

$$\mathbb{E}[x_n] = \mathbb{E}[x]. \tag{1.8}$$

This relation proves that the mean value 1.2 is an unbiased estimator of the true mean value 1.6, since the following chain of equalities holds

$$\mathbb{E}[\widehat{x}] = \frac{1}{N} \sum_{n}^{N} \mathbb{E}[x_n] = \mathbb{E}[x] = \overline{x}. \tag{1.9}$$

The outcome $\widehat{x}$ is thus the best expectation value [10] for the quantity x. Hence, Monte Carlo simulations are a reliable method of providing unbiased results.

1.3 Errors

The definition of the mean value in equation 1.2 clearly shows a dependence on the number N of contributions. It means that the outcome of a Monte Carlo simulation depends on that number. On the other hand, the previous section has shown that the outcome is expected to be equal to the true mean value. The latter is an analytical quantity and it doesn't depend on the number of contributions. Hence, it is reasonable to question how distant the simulation outcome can be from the true mean value and which spread of values is to be expected.

The mathematical object that calculates the expected *distance* between a generic variable x and the true mean value $\overline{x}$ is called the *variance* $\sigma^2(x)$ of x. It is defined as follows

$$\sigma^2(x) = \mathbb{E}[(x - \overline{x})^2] = \int_{\mathbb{D}} \mathrm{d}x \, (x - \overline{x})^2 f(x), \tag{1.10}$$

and can be shown to be identically equal to

$$\sigma^2(x) = \mathbb{E}[x^2] - \mathbb{E}[x]^2 = \overline{x^2} - \overline{x}^2. \tag{1.11}$$

The square root of such quantity is the *standard deviation* σ of x about $\overline{x}$.

In order to determine the spread of values of $\widehat{x}$ about $\overline{x}$, the variance of $\widehat{x}$ has to be considered:

$$\sigma^2(\widehat{x}) = \mathbb{E}[(\widehat{x} - \overline{x})^2], \tag{1.12}$$

which can be proved to lead to

$$\sigma(\widehat{x}) = \frac{1}{\sqrt{N}} \sigma(x), \tag{1.13}$$

using the linearity of the expectation values and the definition for the variance of equations 1.10 and 1.11, as well as the mean value 1.2 and true mean value 1.6 definitions.

The standard deviation $\sigma(\widehat{x})$ still requires to evaluate $\sigma(x)$ which in turn requires the knowledge of the usually unknown probability density function. A viable alternative is to use the *sample variance* S^2

$$S^2 = \frac{1}{N-1} \sum_{n}^{X} (x_n - \widehat{x})^2, \tag{1.14}$$

which can be proved to be an unbiased estimator for the variance of the mean value [10]. It means that it converges to the variance 1.11 for large values of N or, in terms of expectation values, the following holds:

$$\mathbb{E}[S^2] = \sigma^2(x). \tag{1.15}$$

The outcome of a Monte Carlo simulation for each of the quantities required by the user, is the estimated mean value of such quantity with its relative error calculated as $S^2/\widehat{x}$. Equations 1.13 and 1.2 show that such error is proportional to the number of particles that contributed to that estimation as $\sim N^{-1/2}$. This is indeed a major drawback of using Monte Carlo methods which, despite of the reliability of their results, the outcome can be affected by very large errors. Furthermore, it also means that increasing the number of particles by an order of magnitude, result in an improved precision by only a factor of $\sqrt{10} \simeq 3$, while the time required by the simulation increases linearly by a factor of 10.

It is still possible to use Monte Carlo simulations despite such notable limitation. The trade-off is to use appropriate techniques that depart from *analog* Monte Carlo by means of semi-deterministic methods or various procedures that distort the statistical sampling in a convenient and unbiased manner.

1.4 Variance reduction

Depending on the type of problem under consideration, an analog Monte Carlo simulation might not be sufficiently efficient in order to return results in short and reasonable times and without using much computing power. One of these kind of problems is shielding calculations, where the purpose is to minimize the radiation in some regions of space translates to the demand to minimize the number of particles in those volumes. This competes with the need of having a large number of particles in those regions so to have good estimators and variances for the quantity of interest.

In a typical shielding simulation quantities like dose rates, currents or fluxes have to be estimated in some region of space. Particles can usually reach those volumes only by crossing a thick bulk of some specifically chosen absorbent material. A typical attenuation factor for a shielding simulation is of about $10^6 - 10^9$ [2], which means that only one particle out of one million or one billion can contribute to the estimation of the desired quantity. Even if a relatively good computing power is available, such kind of simulations might take days or even weeks. Depending on the user request, an analog simulation might even require months before terminating. In practice, there might be cases in which there's no way to obtain a solution in a reasonable amount of time. In other cases, although there might be a chance to eventually obtain the desired estimation with an acceptable error, it would be at the great expense of time and computing resources.

It is still possible to use Monte Carlo simulations in these cases, provided they can be modified to be sufficiently efficient, that is making them return better results in a shorter time while possibly generating even less source particles. To achieve that aim, some non-analog techniques have to be used when setting up the simulation. Several approach are possible, like terminating the histories of those particle that reach regions that are supposed to have only a very little chance to contribute and by a fair small extent. Another possibility is to set an energy threshold so to terminate the histories of particles when their energy drops below it.

A possible approach is to modify the Monte Carlo simulation so to sample a biased probability density function $\widetilde{f}$ for the desired quantity. In the previous sections, not a single hypothesis was considered on the shape of the probability density function f of the quantity to be estimated by the Monte Carlo simulation. In most realistic problems, only some of the source particles have a chance to reach the region in which the tally was set in the simulation. Those which don't contribute to the estimation can be seen as if they sampled a delta function δ centred about the origin $\delta(x)$. Those particles that contribute to the estimation, follow the true probability density function $g(x)$. The entire probability density function can thus be written as

$$f(x) = a\delta(x) + g(x), \tag{1.16}$$

and it can be represented as in figure 1.2.

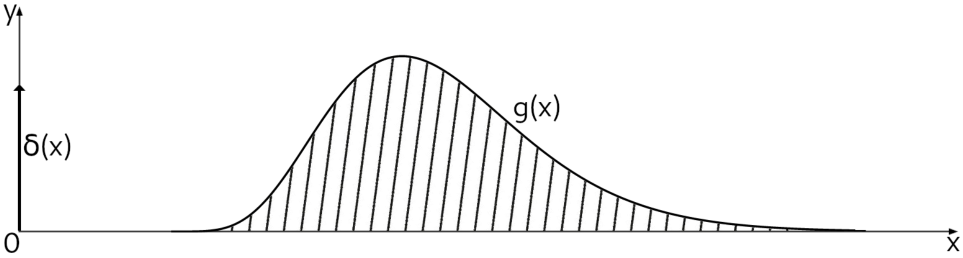

Figure 1.2: Sketch of a generic probability density function used in Monte Carlo simulations.

The mean value of equation 1.16 is the same as that of $g(x)$, due to the property of the delta function:

$$\overline{x} = \int_{\mathbb{D}} \mathrm{d}x \, x f(x) = \int_{\mathbb{D}} \mathrm{d}x \, x(a\delta(x) + g(x)) = \int_{\mathbb{D}} \mathrm{d}x \, x g(x). \tag{1.17}$$

The factor a in equation 1.16 is the fraction of particles that do not contribute to the estimation of the mean value. The fraction of particles that contribute is the integral area under the curve $g(x)$. The property of the delta function and the normalization requirement of equation 1.5 for the function $f(x)$ show that such area is equal to $1 - a$:

$$\int_{\mathbb{D}} \mathrm{d}x \, f(x) = a \int_{\mathbb{D}} \mathrm{d}x \, \delta(x) + \int_{\mathbb{D}} \mathrm{d}x \, g(x) = 1 = a + \int_{\mathbb{D}} \mathrm{d}x \, g(x). \tag{1.18}$$

Such factor a has to be reduced in order to promote more particles to contribute to the estimation of the mean value.

When the variance for the function f is considered, it can be split into two parts, one for the delta and the other for the function $g(x)$:

$$\sigma_f^2(x) = \sigma_\delta^2(x) + \sigma_g^2(x). \tag{1.19}$$

The first term on the right can be seen as a factor that quantifies the inefficiency of the Monte Carlo simulation, while the second represents the intrinsic variance of the function g. Several techniques have been introduced in order to improve the fraction of particles that contribute to the estimation of the quantity of interest. Since their purpose is to reduce the term $\sigma_\delta^2(x)$, they are called *variance reduction techniques.*

1.4.1 Biasing the density function

One type of variance reduction techniques consists of sampling from a different probability density function $\widetilde{f}$. If no other care is taken, that would simply lead to biased results, because the simulation would not sample the mean value for the original underlying probability density function f. Each particle contribution is thus weighted by a statistical factor w. Such factors have to follow a particular weighting function w that satisfies

$$f(x) = w(x)\widetilde{f}(x), \tag{1.20}$$

so that any increase or decrease in the biased function $\widetilde{f}$ is compensated by a proportional decrease or increase in the weight factor $w(x)$ for each particle contribution.

The equation 1.6 for the true mean value is now to be written as

$$\overline{x} = \int_{\mathbb{D}} \mathrm{d}x\, x(w(x)\widetilde{f}(x)). \tag{1.21}$$

It is clear that, if equation 1.20 holds, the true mean value is preserved. In the discrete and real case, this means that instead of evalauting the mean value $\widehat{x}$ as in equation 1.2, the simulation samples by $\widetilde{f}$ and thus it evaluates the following

$$\widehat{wx} = \frac{1}{N}\sum_{n}^{N} w_n x_n, \tag{1.22}$$

If the sampling is unbiased, the expectation value for the mean value $\mathbb{E}[\widehat{x}]$ converges to the true mean value $\widehat{x}$. It is worth stressing the latter statement, that equations 1.22 and 1.2 do not provide the same identical values for each number of histories N. A sufficiently high number of particles has to be generated so to let them converge.

The ultimate purpose for biasing the probability density function is to minimize the equation 1.19 and, in particular, the contribution to the delta function. The notable benefit of this technique is that, apart from preserving the expectation values for the mean values, it doesn't preserve the variance. In fact, the evaluated variance when sampling by a biased probability density function is:

$$\sigma^2(w(x)x) = \int_{\mathbb{D}} \mathrm{d}x\, (w(x)x - \widehat{x})^2 \widetilde{f}(x), \tag{1.23}$$

which can be written as

$$\sigma^2(w(x)x) = \int_{\mathbb{D}} \mathrm{d}x\, (xw(x))^2 \widetilde{f}(x) - \left(\int_{\mathbb{D}} \mathrm{d}x\, w(x)x\widetilde{f}(x) \right)^2, \tag{1.24}$$

or, in a more compact form:

$$\sigma^2(wx) = \widehat{(wx)^2} - (\widehat{wx})^2, \tag{1.25}$$

where the latter term in this equation is equal to the square of true mean value $\widehat{x}$.

If the biased function $\widetilde{f}$, and hence the weight function $w(x)$, could thus be chosen so to satisfy

$$w(x)x = \widehat{x}, \tag{1.26}$$

the variance in equation 1.25 becomes identically zero. Unfortunately, finding that function $w(x)$ that solves the equation is a non trivial problem, but it leads one to look for approximate solutions.

1.5 MCNP

Monte Carlo N-Particle, or simply MCNP, is a Monte Carlo particle transport code developed and maintained by Los Alamos National Laboratory. It is capable of simulating the interactions of an extensive number of particle types, ranging from nucleons and photons to heavy ions. Due to its great versatility, it finds applications in a variety of fields like criticality calculations, radiation protection, radiography, medical physics, dosimetry, radiation shielding, accelerator target design, etc.

MCNP was chosen for licensing reasons as the main tool for producing the results presented in this thesis. The following paragraphs provide an overview on the code and on some relevant code commands that are recalled throughout the text.

The section ends with a brief overview on the available variance reduction techniques in MCNP. Particular care is given to that which is largely used during the work, to whom a separate section is dedicated.

1.5.1 Basic input file structure

The fundamental input interface to MCNP is a text file, or a set of files read by a main. The content of that file consists in a list of input commands, usually named *cards*. The user can rely on an extensive set of cards for modelling the geometry in a virtual tridimensional space, and for setting up all the relevant parameters for the simulation.

The input file has to follow a rigid structure in which three main blocks have to be identified [11]:

1. cells definition: each geometrical volume has to be defined by mean of intersections and unions of basic surfaces, using boolean algebra methodology [12]. The definition of each cell is completed by specifying a proper material and density. Other auxiliary geometrical parameters can be added if needed;

2. surfaces definition: they are elementary surfaces like planes, spheres, cones, etc;

3. physics and simulation settings: the particle types to transport and simulate, the energy ranges, variance reduction methods, source definition, material specification, detectors and support cards find their place in the third block.

1.5.2 Tallies

The primary way of getting results from a MCNP simulation is to use appropriate cards referred as tallies. Each tally card specifies a particular physical quantity that the user may inquire. Three main types of quantities can be identified: current, flux and energy deposition. Depending on which tally is used, the outcome of such quantities are averaged over a surface or a volume, or can be estimated at a specific point in space. Apart from the latter case, in which the estimation is performed by mean of the semi-deterministic procedure of the next-event estimator [12], tallies estimate the physical quantity by counting the number of histories that are transported through the specific surface or volume.

Tallies need some specific spatial collocation in the simulated geometrical model. That might be a surface for evaluating particle current or flux across it, as well as cells for estimating the particle flux averaged over a volume, and so on.

Tallies can be grouped into two categories according to how they are geometrically defined:

- Geometry-dependent: is the case for those tallies that require to specify on which surfaces or cells, or in which coordinates they are applied,

- Geometry-independent: they require to define a superimposed spherical, cylindrical or rectangular *mesh*.

By default, tallies outcomes are normalized to one source particle. A set of tally multiplier cards allow to change the outcomes by multiplying the results by a constant factor, or by folding the results by a function so to extend the spectrum of basic quantities that MCNP can estimate. The latter method is used in this work to estimate dose rates values by folding the flux with appropriate input conversion functions given later in this chapter, in section 1.6.

1.5.3 Variance reduction cards

MCNP offers a collection of cards for setting up several variance reduction techniques. Part of them are devised so to change the underlying probability density function of the quantity of interest, while other use a semi-deterministic procedure. Depending on the method that they use, four main types of techniques can be made:

- truncation: this type of techniques consists of terminating the histories of those particles whose energy or track time is below a specified cut-off. An example of a somewhat unintended truncation is inherent in the choices taken while modelling the geometry. A detailed model can affect the time length of the simulation [13] since more possible interactions have to be calculated per each history. Excessively large models allow longer particle tracks, even in regions far from that of interest. Removing geometrical regions from the model can be an initial attempt to promote particles in the direction of interest. On the other hand, an over-simplified model can lead to poor and biased estimates.

  These methods are likely to give more precise results but at the expenses of a higher chance to bias the results making them less accurate.

- population control: splitting the particles to increase their number, and killing them when their weight drops lower than a proper threshold or by playing the Russian roulette game [11], are ways of controlling the number of samples that contribute to the tally. Over-splitting particles can reduce the statistical variability of the samples, since the progeny of the same progenitor is generated with identical initial parameters, although their histories will differ. Over-killing reduces the efficiency of the simulation.

- modified sampling: these methods alter the statistical sampling by, for example, shortening (forced collisions [11]) or stretching in a specific direction (exponential transform [11]) the mean free path length between collisions in order to adequately tally particle interactions in small volumes or to increase the transmittance through thick materials.

- semi-deterministic: point detectors are an example of this type of estimators that calculate the contribution that each newly generated particle or any existing particle after an interaction would give to the point of interest, by calculating the chance that they can have to reach that specific point.

The use of any variance reduction technique usually increases the computational time required for the simulation. On the other hand, they can reduce the number of particles giving zero contribution and hence reduce the variance of tally outcomes. In some cases, using variance reduction techniques can be the only available way of getting a non-zero outcome in reasonable times. The shielding studies presented in this thesis is an example of the latter case. The most used variance reduction technique in the present work, the *weight window*[14], is explained thoroughly in the next section.

1.5.3.1 Weight windows

The weight window is a particular technique that controls the particle population by splitting or killing them as they cross cell boundaries or interact. The name recalls the fact that only those particles whose weight is between an appropriate range are neither splitter or killed, so that they can pass through untouched.

There are two types of weight windows, cell-based and mesh-based. They only differ in the way they are applied to the simulation. The cell-based weight window is applied to the geometrical cells defined in the first block of the MCNP input file. The mesh-based instead requires to define a superimposed tridimensional mesh. The latter has a dimmer geometrical dependence, but requires to define an adequately fine mesh whose voxel size is comparable to the average cells size. On the other hand, the cell-based weight window might require a wise partial rearrangement of the geometry.

The focus here is on the mesh-based weight window, which is the one used for the present work. However the following concepts applies for both types, with the only difference that the term *voxels* is to be replaced by *cells* for a cell-based weight window.

At each voxel of the mesh a lower weight bound is assigned. The upper bound is specified by means of the multiplication of the lower bound by a constant user-defined factor. The particle weight is checked at each collision or when crossing the voxel boundary. If it is higher than the upper bound, the particle is splitted as many times as needed so that the progeny has a weight in-between the bounds. If it is lower than the lower bound, the Russian roulette game is played so that the particle is either killed or its weight is increased so to lie in the accepted range. A representative sketch of the weight window technique is shown in figure 1.3.

A weight window can be set so to check particle weight either at voxel boundaries or at collision or at both events. Different weight boundaries

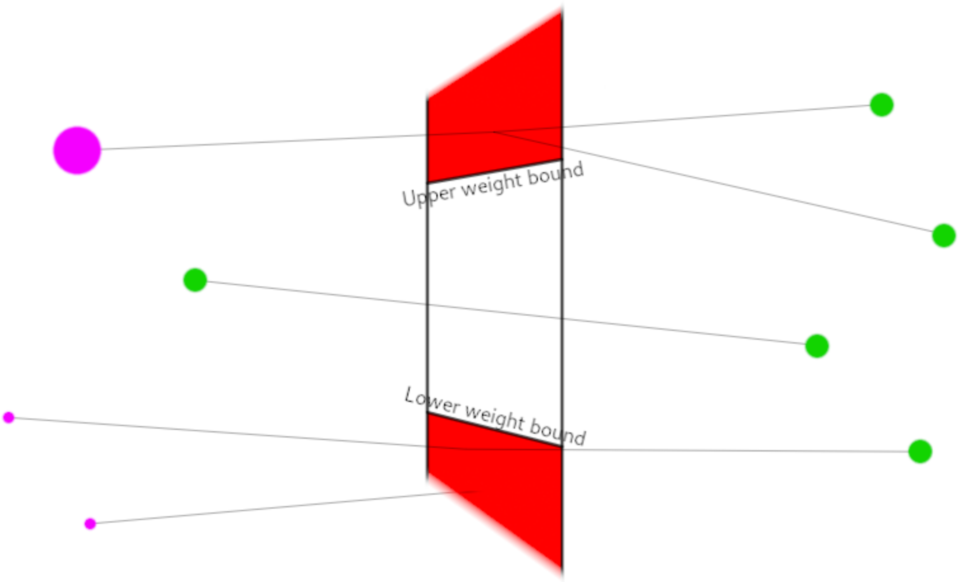

Figure 1.3: Sketch of the weight window technique.

can also be defined so that each of them is applied to particles depending on their energy, time or both.

1.6 Dose

The purpose of the work presented in this thesis is to design the shielding of VESPA, which is one of the instruments that will be built at the European Spallation Source. In particular, the thesis is focused on designing the shielding of the beam-line in the area of the facility which is accessible to users. This task requires to determine the optimal shielding structure that minimizes the radiological dose in some specific area of interest.

In any radioactive environment it is mandatory to evaluate the effects and the potential human hazard due to presence of radiation sources. Several quantities can be defined to describe a radiation field, among those the ones of interest for shielding studies are the radioactive doses and dose rates.

The basic quantity in radiological protection is the *absorbed dose* D, which is defined as the amount of energy imparted dE by the ionizing radiation to a unit mass dm of matter:

$$D = \frac{dE}{dm}, \tag{1.27}$$

where the energy imparted is the amount of net radiant energy R released in the unit of matter by both charged and uncharged particles, including the net energy $\sum Q$ due to the sum of the *Q-values* of all the nuclear reactions that take place:

$$E = (R_{charged} + R_{uncharged})^{IN} - (R_{charged} + R_{uncharged})^{OUT} + \sum Q. \quad (1.28)$$

The absorbed dose is measured in J/kg, which is called *gray* (Gy).

From the definition 1.27 it follows that D is a local quantity, because it is defined point by point, although its value depends on the atoms in the unit of matter dm under consideration. In all practical case, it is possible to define standard procedures for allowing its measurement.

The type of radiation has a sensible effect on the amount of energy imparted in matter, hence on the value of the absorbed dose. However, the biological effects are dependent on the *linear energy transfer* L, which is the spatial rate of energy deposited along the particle track. The dependency of the health effects on the radiation type is taken into account in radiation protection by introducing the *equivalent dose* H. It is defined based on the definition of the absorbed dose as:

$$H = \sum_R w_R D_R, \quad (1.29)$$

where the pedix $_R$ stands for "radiation" and w_R is the weighting factor for the radiation R. The equivalent dose is thus the sum performed over all the types of radiation involved, of the absorbed dose produced by each radiation type, each weighted by an appropriate weight factor. The weighting factors are dimensionless coefficients determined by judgements on radiobiological experiments and regulated by the International Commission on Radiological Protection (ICRP).

An alternative definition for the equivalent dose uses the quality factor Q[1], which is a function of the linear energy transfer:

$$H = QD. \quad (1.30)$$

Since the biological effects caused by radiation show a different grade of severity depending on the type of tissue, the *effective dose* is introduced to quantity such effect. Similarly to equation 1.27, the effective dose is defined as the sum of all the equivalent doses weighted by a dimensionless tissue-dependent factor:

$$E = \sum_T w_T D_T, \quad (1.31)$$

where the subscript $_T$ here stands for *tissue*. The sum is performed over those tissues and organs which are considered to be sensitive to the radiation effects. A different value is thus assigned to the same radiation field

---

[1] Although the same letter Q is used for representing both the Q-value for nuclear reactions and the quality factor in the equivalent dose, the two quantities are unrelated.

depending on the exposed organ, e.g. the effective dose value is higher if the stomach is impacted rather than the liver.

The unit of the equivalent and the effective doses is J/kg that, unlike the absorbed dose, in these cases takes the name of *sievert* (Sv).

Due to the origin of the weighting factors, the equivalent dose and the effective dose are not physical quantities and thus they are not measurable. In practice, it is possible to determine those quantities by applying conversion coefficients on the measured *fluence*.

The fluence Φ of the radiation field is the ratio of the number of particles dN incident on a sphere of cross-sectional area da:

$$\Phi = \frac{\mathrm{d}N}{\mathrm{d}a}. \tag{1.32}$$

It corresponds to the time integral of the flux over the irradiation time.

The conversion coefficients that convert the fluence to dose have to take into account the quality factor Q, the probability of producing secondary ionizing particles, the amount of energy that they deposit in matter as well as the effects on the human body. For the scope, ICRP performs simulations using particle transport codes in which the human body and its internal structure and organs are modelled as a computational phantom. Several geometries are investigated in which the phantom is irradiated from different directions. This because the human model is sufficiently detailed so that it is possible to appreciate differences in the absorbed dose in organs, depending on their position respect to the irradiated surface. The resulting conversion functions thus have a dependency on the reciprocal geometry of the phantom and the radiation field. The graphs in figure 1.4 show such dependency for neutron and gamma fluence to effective dose functions. The red and green lines represent the two extreme radiation conditions, while the blue lines show the particular case of a radiating source moving in a circle and pointing towards a human body placed in the centre.

According to the internal documentation at the European Spallation Source [15], the conversion factors used in this thesis are those that follow the red lines in the pictures, that calculate the maximum values for a given fluence of neutrons and gammas. The tabulated values are reported in appendix A.

Another document [16] classifies the areas in the facility depending on the expected dose to people and defines the maximum allowable dose values for those. According to the internal document [17], the area in which the VESPA instrument will be built is classified as *supervised area.* As a consequence, the dose on the outer surface of the shielding structure of VESPA shall not exceed $3\,\mu$Sv/h. Document [15] also imposes a safety factor for the shielding studies performed using any particle transport code, included MCNP. Such safety factor is equal to 2, so that the outcome of the simulations shall not exceed half of the maximum allowed dose for the area under

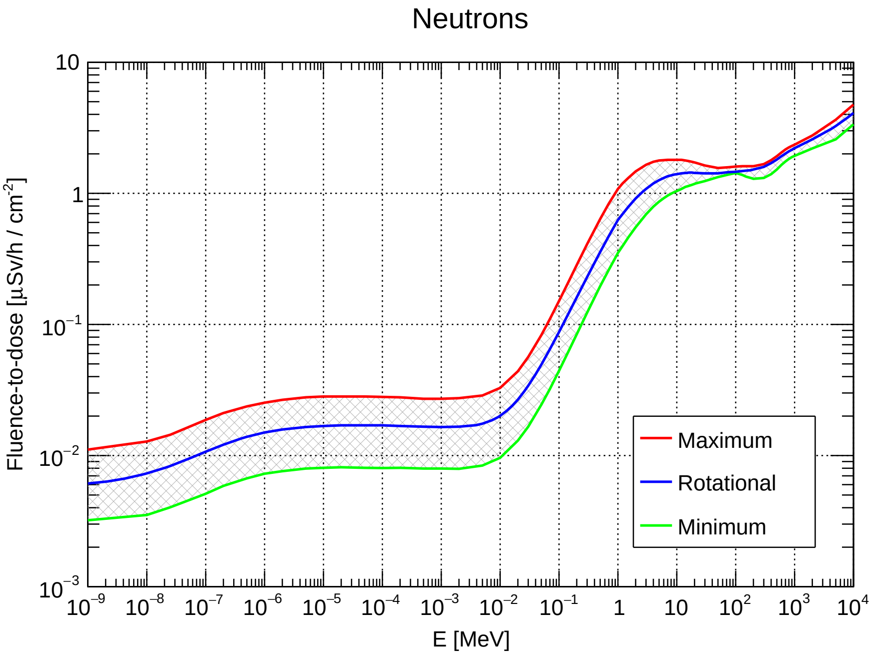

(a)

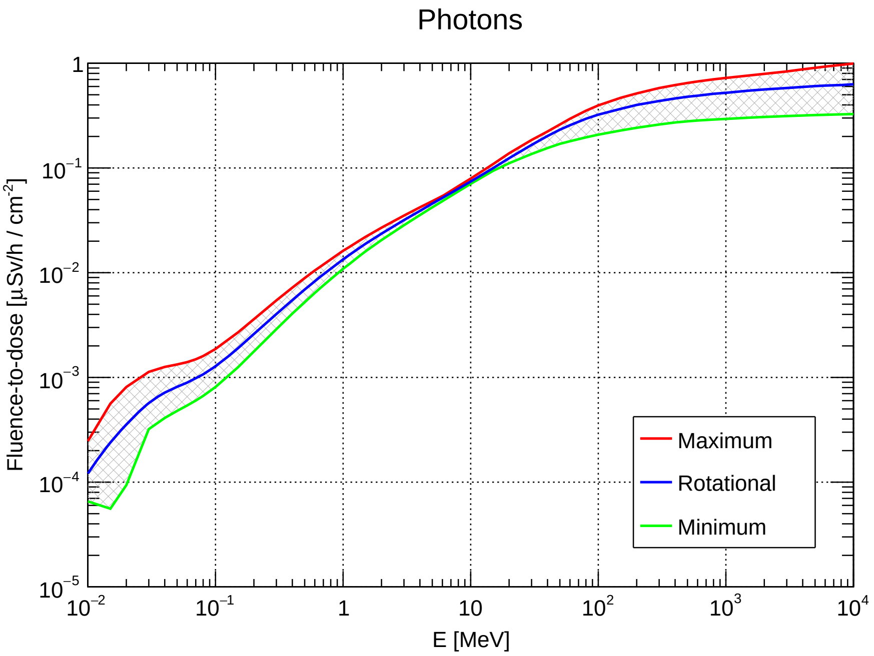

(b)

Figure 1.4: Fluence to effective dose conversion functions for neutrons (a) and gammas (b).

consideration. The purpose of this thesis is therefore to design the shielding for VESPA so that its outer surface do not exceed 1.5 μSv/h.

1.6.1 Transmittance through thick means

The main task in typical shielding simulations is to determine the flux or the radiation dose rate of some radioactive source after crossing a thick shielding material.

Consider the simple case of a narrow and mono-energetic particle beam passing through a homogeneus material ([1]). The reduction of the particle current dI in a short distance $\mathrm{d}x$, along the beam direction, is proportional to the density of target atoms n, to the probability σ of interacting with such material and to the available current I at the considered depth x:

$$\mathrm{d}I = -I(x) n\sigma \, \mathrm{d}x \tag{1.33}$$

The minus sign accounts for the fact that the current I decreases in such mean, and thus dI is negative while $\mathrm{d}x$ is positive. The quantity $n\sigma$ is commonly known as the macroscopic cross section Σ, which essentially represents the effective target area of all atoms in the material.

If we integrate the previous equation, we get:

$$I(x)/I_0 = e^{-\Sigma x} \tag{1.34}$$

which represents the particle transmittance for the specific particle, after crossing a slab of thickness x, due to the type of interactions described by Σ.

If the requirement of a mono-energetic particle beam is loosen, the energy dependence of the cross section $\sigma = \sigma(E)$ has to be taken into account. Equation 1.34 thus can be written as

$$I(E)/I_0 = e^{-\Sigma(E)x} \tag{1.35}$$

which gives the fraction of particles of energy E that do not interact after penetrating a thickness x.

The latter equation doesn't hold if the mean is a inhomogeneous material, for which the cross section $\sigma(E)$ and the atom density n both depend on the position x. Another limitation come from the fact that even a narrow beam show some spread when travelling in any material. A build-up factor should be taken into account so to consider those particles that are elastically scattered inside the material and happen to contribute to the transmitted current. If both sides equation 1.35 are integrated over all energies, even non-elastic scatterings contribute to the revealed transmittance.

In practical cases, in which more materials are usually involved and the radiation source is far from being approximated to a narrow beam, equation 1.35 only gives a reasonable prediction on the transmittance.

Chapter 2

European Spallation Source

The European Spallation Source (ESS) [18] is a neutron source facility which is being built in Lund, Sweden [19]. It will be the world's most powerful pulsed neutron source, capable of providing unprecedented peak brightness, 30 times higher than the world's most powerful reactor-based neutron source [20].

This chapter gives an overview about the facility, with particular care for those areas that are directly involved or addressed in the rest of this thesis. Most of the content of this chapter comes from the Technical Design Report [21] which represents a milestone for ESS. Many steps forward were taken, but it is still a valid comprehensive document for the facility.

2.1 The facility

ESS is one of the largest scientific infrastructure projects under construction nowadays. It is designed to include one of the most powerful linear proton accelerator ever built [18], that will deliver an energetic proton beam on a tungsten target. The interaction leads to spallation reactions that generate neutrons of energies up to that of the proton beam. A complex moderator system slows neutrons down to thermal and sub-thermal energies, and will deliver them to the instruments, which are radially arranged about the target.

A preliminary layout of the ESS facility is shown in figure 2.1, while figure 2.2 shows the main phases of the construction plan.

2.1.1 Source and target

ESS is provided with a liner proton accelerator (LINAC), 600 m long, that accelerates protons up to 2 GeV in energy. The proton beam impinges on a rotating tungsten wheel about 2.6 m in diameter. It is subdivided into 36 sectors, in each of which 190 tungsten bricks are collocated in a staggered

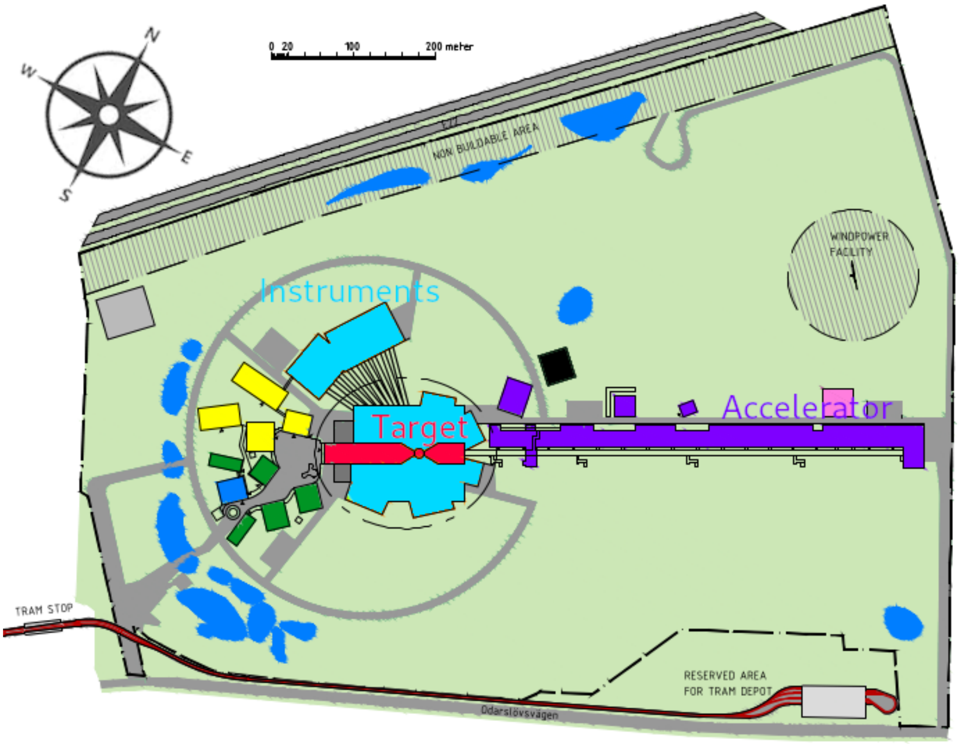

Figure 2.1: Top view of the preliminary layout for the ESS facility.

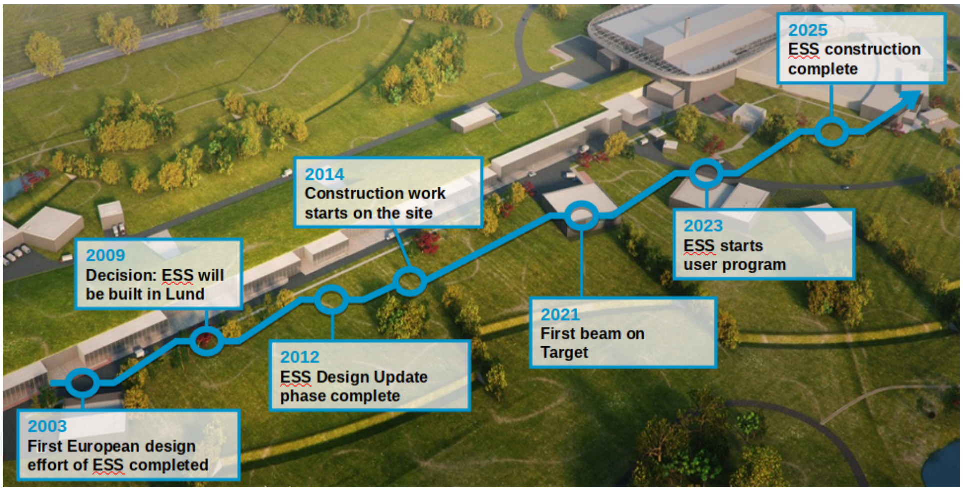

2003
First European design effort of ESS completed

2009
Decision: ESS will be built in Lund

2012
ESS Design Update phase complete

2014
Construction work starts on the site

2021
First beam on Target

2023
ESS starts user program

2025
ESS construction complete

Figure 2.2: Main phases of the construction plan of ESS.

pattern [22], as shown in figure 2.3.

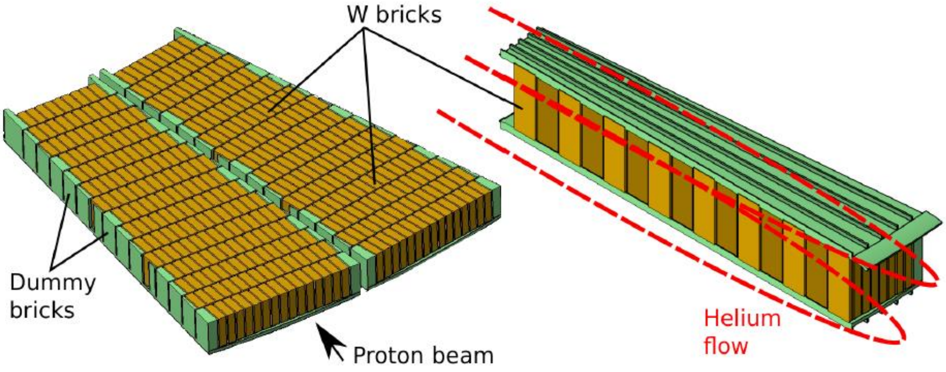

Figure 2.3: Detail of the target wheel showing the disposition of the tungsten bricks [23].

The proton beam is delivered in long pulses having a time-length of 2.86 ms and with a repetition rate of 14 Hz. The frequency of revolution of the target wheel is adjusted so that each single pulse hits a different sector. The proton beam current averaged over a time-length of 1 s is of 2.5 mA, that, given the energy of 2 GeV, results in an average power of 5 MW constantly delivered to the target in the full-power regime. For better reference, such parameters are summarized in table 2.1.

Parameter	Value	Unit
Average beam power	5	MW
Proton kinetic energy	2	GeV
Time-averaged current	2.5	mA
Pulse repetition rate	14	Hz

Table 2.1: Main ESS parameters.

2.1.2 Target-Moderator-Reflector

Neutrons generated from the spallation reaction [24] can have energies up to that of the incoming proton beam. They are slowed down by a complex moderator system which is placed on top of the target wheel. It consists of two main parts, a pre-moderator and thermal and cold moderator. The pre-moderator is a water filled disk 70 cm in diameter and 3.6 cm high. It is placed so that its axis is parallel to the target wheel axis, and its centre is placed right on top of the region in which there is the maximum production of fast neutron in the target.

The cold and thermal moderator system is referred to as *butterfly moderator* because of its shape, shown in figure 2.4. The two *wings* form the thermal moderator, which can be considered as an extension of the pre-moderator, since the moderator material is ambient temperature water. The cross-shaped *body* of the butterfly is the cold moderator, which is filled with liquid para-hydrogen at 20 K.

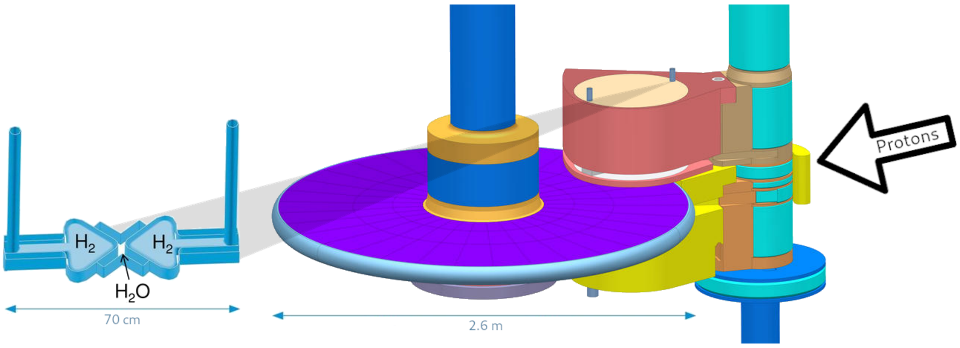

Figure 2.4: The butterfly moderator on the left and its location respect to the target wheel on the right [25].

The centre of the cold moderator is also the thermal and sub-thermal neutron hotspot of energies below 0.6 eV [26]. It is located at a distance of 13.7 cm from the plane of symmetry of the target wheel.

On top of the moderator system a bulk of beryllium is designed for reflecting neutrons back to the moderator, so to reduce the neutron losses.

The moderator and reflector systems constitute a plug, that can be moved sideways for maintenance. They are shown in yellow and light red in figure 2.4. Such plug and the part of the target wheel which is hit by the proton beam constitute the so called Target Moderator Reflector Assembly TMRA.

2.1.3 Monolith

The TMRA is integrated in the centre of a steel structure, named *monolith*. It's a bulky cylinder of cast iron, 11 m in diameter [22], whose main purpose is to adequately shield the surrounding area so to allow personnel access. Apart from the moderator-reflector plug, it contains the entire target wheel, as well as its shaft, the diagnostics and all the electric and coolant supply channels, as shown in figure 2.5 and in figure 2.6.

In addition to providing an adequate shielding, the monolith also has the purpose of delivering neutrons to the beam-lines. The neutron beam extraction system starts with two symmetrical straight tapered openings in the monolith, 120 ° wide in the horizontal direction. These two openings spread till a distance of 2 m from the moderator centre. Neutrons travel till such distance, where they meet 42 rectangular openings in the monolith. Those openings represent the starting point of each instrument at ESS. Hence ESS is designed so to allow up to a total of 42 instruments. Currently, a total of 16 instruments are currently being built. The remaining unused beam-ports and their monolith insert are filled with a steel plug to stop neutrons in the unused beam-ports.

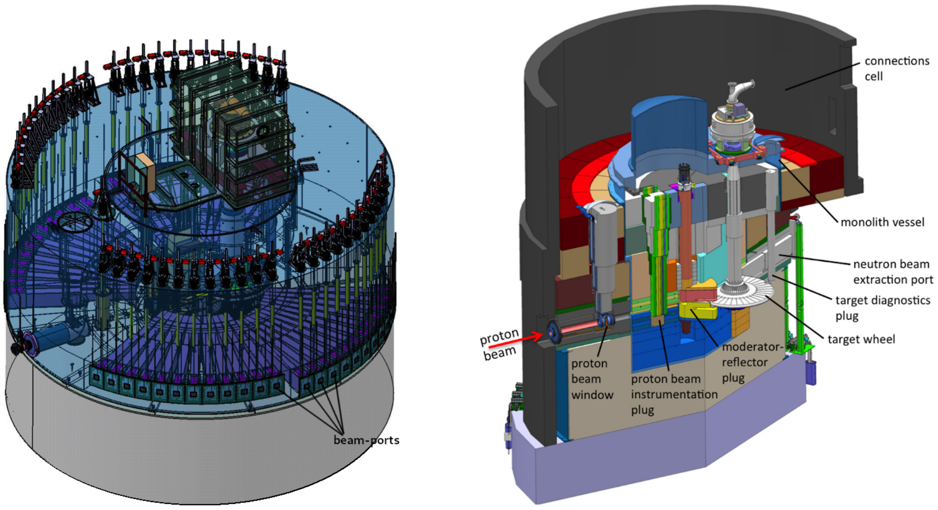

(a) (b)

Figure 2.5: General layout (a) and a cut section (b) of the monolith.

The first element of each instrument is an optically active guide insert that extend from 2 m till the monolith external surface at 5.5 m. Such element is called Neutron Beam Optic Assembly (NBOA), which is part of a the Neutron Beam Extraction (NBEX) element. A representative NBEX is shown in figure 2.8.

Each of the monolith insert ends in an external monolith opening, called beam-port. The 42 beam-ports have a non-uniform average separation angle of $\sim 6\,^{\circ}$, and are arranged so that each of the two symmetrical sides of the monolith have 21 ports. Both sides are further subdivided into a total of 4 sectors, which are addressed depending on their geographical orientation as shown in figure 2.7. West and South sectors are both dedicated to long instruments, that is instruments whose total length can be up to 150 m, while North and East sectors are designed for short instruments of some tens of meters.

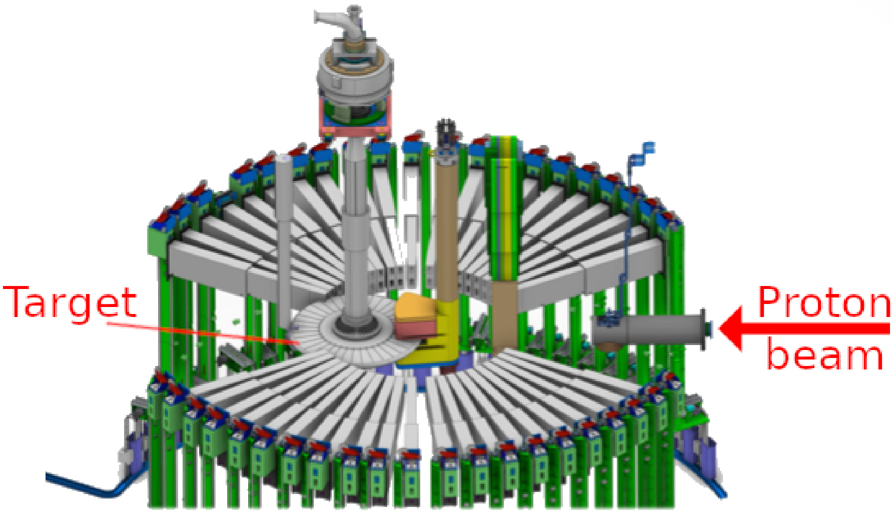

Figure 2.6: View of the TMRA and the beam-ports in the monolith.

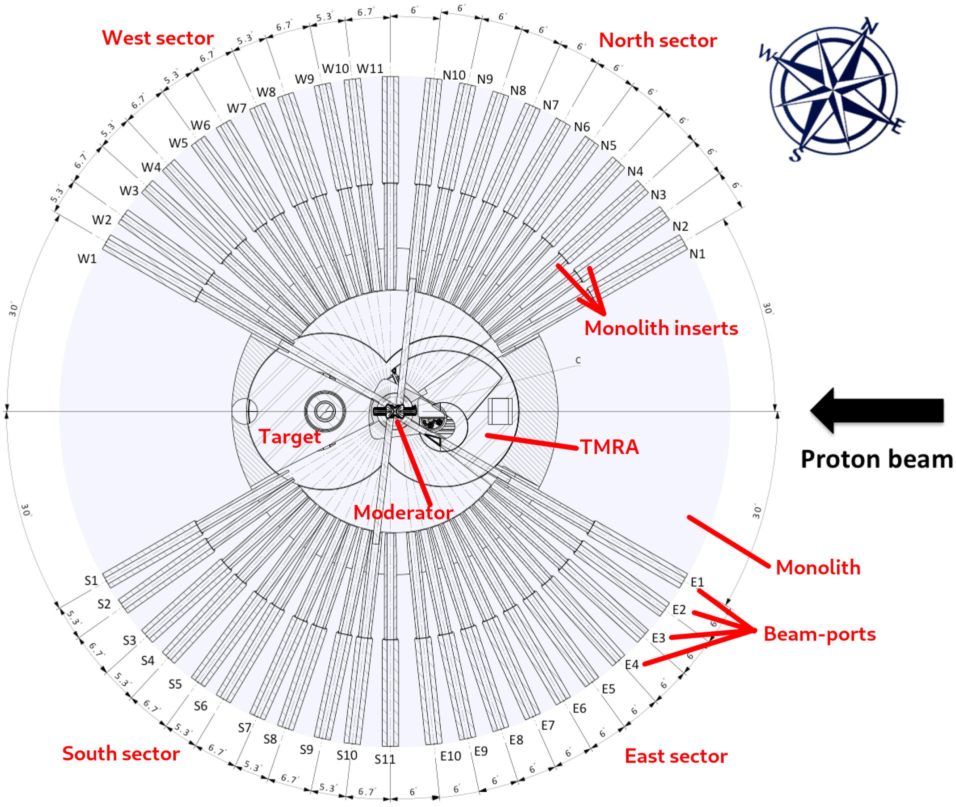

Figure 2.7: Top-view of ESS monolith.

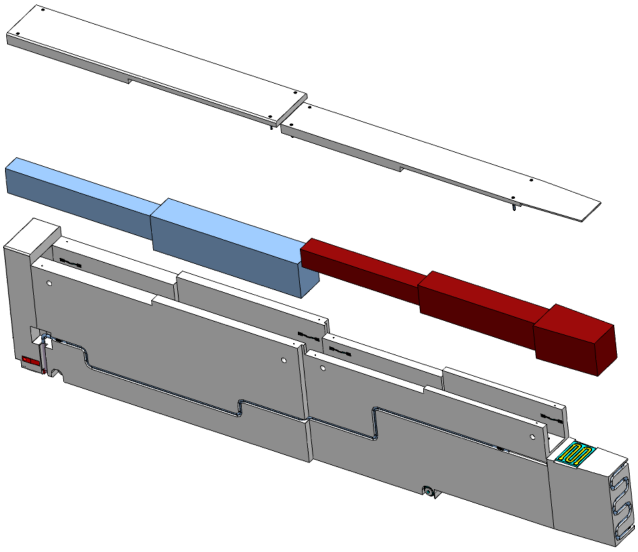

Figure 2.8: Layout of a representative NBEX [27].

2.1.4 Bunker

A wide void area surrounds the monolith in order to further reduce the escaping radiation. Such area, called bunker, is delimited by a heavy concrete wall, 3 m high and 3.5 m thick [28], whose purpose is to shield the external area and to reduce the background on the instruments. It start at 11.5 m from the moderator centre for the short sectors, and at 24.5 m for the long instrument. The final shape somewhat recalls another butterfly, as can be seen in figure 2.9.

The bunker is a non-accessible area of the facility. Therefore, all the operations there must be dealt using remote control, including the handling of the instrument components.

2.1.5 Halls

Outside of the bunker wall, one last covered area surrounds the TMRA. It's called *hall* and, more specifically, *instrument hall*, since it contains part of the instruments, as well as laboratories, offices, and a number of ancillary areas. It is a wide open area that hosts all the short instruments and the long instruments in the South sector. The longest instruments in the West sectors protrude from the main hall that surrounds the bunker, as shown in figure 2.10, while figure 2.11 shows a possible layout for an instrument in the West sector. Their guide sections of the instruments in the West sector are contained in a *neutron guide hall* that ends in a secondary arched instrument hall.

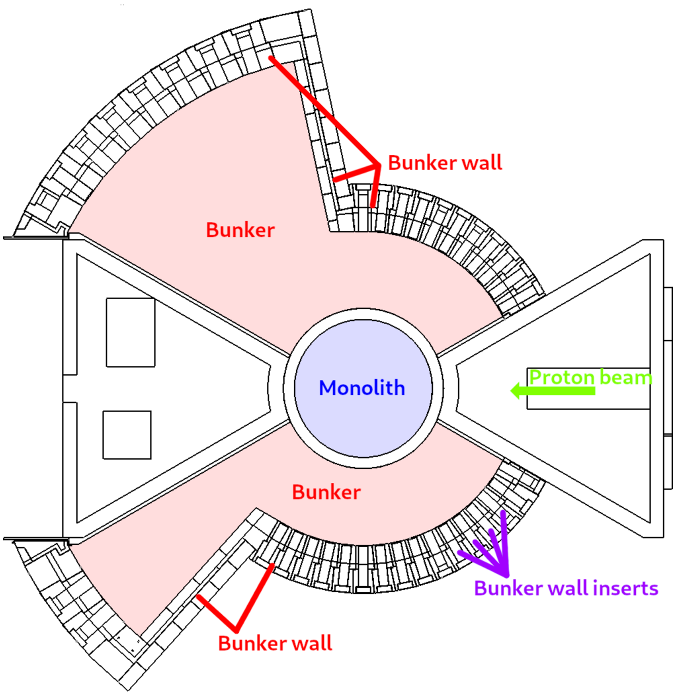

Figure 2.9: Top-view of ESS bunker.

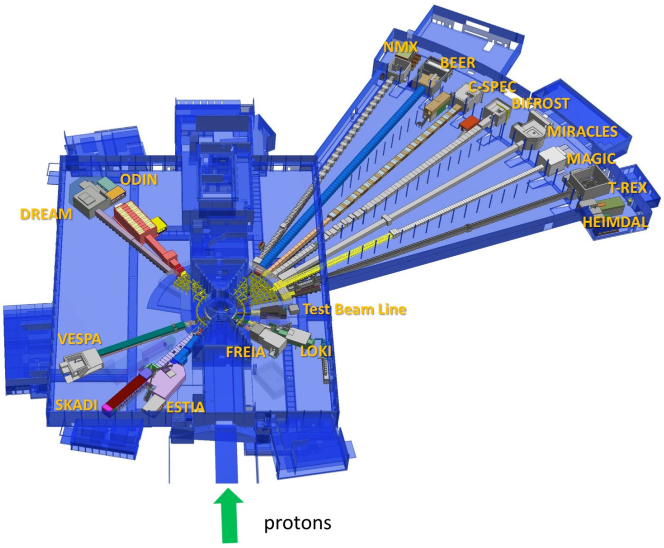

Figure 2.10: Top-view of ESS, showing the bunker, the instrument halls, the 16 instruments under construction and their relative disposition respect to the proton beam.

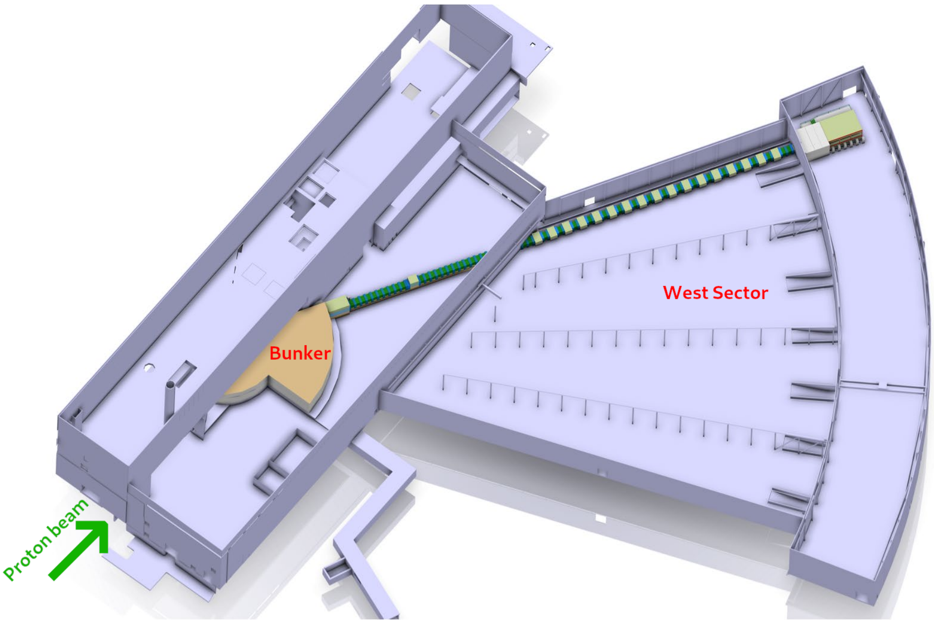

Figure 2.11: Possible layout of an instrument in the West sector

The present work is focused on VESPA instrument, which will be built in the East sector, at beam-port E7. It is one of the instruments which are being built in the East sector. Despite being in a short sector, the distance of the sample from the moderator in VESPA is about 60 m long, making it at the edge of a medium instrument.

Chapter 3

VESPA

The present work aims to design the biological shielding for VESPA instrument, which is one of the 16 instruments currently under construction at ESS [29].

This chapter provides an introduction to VESPA instrument and a detailed description of its components. Much care is given especially to the geometry and the material composition, since they are of main interest for setting up the neutronic calculations.

3.1 Scientific case

VESPA project is a partnership of CNR (Consiglio Nazionale delle Ricerche, IT) and STFC (Science and Technology Facilities Council, UK) [29, 30]. The name gives a hint on which type of instrument VESPA is, in fact it stands for Vibrational Excitations Spectroscopy with Pyrolytic-graphite Analysers. VESPA will be the only inverse geometry neutron spectrometer at ESS fully dedicated to Neutron Vibrational Spectroscopy for chemical and material science applications [31].

The instrument is designed so exploit the long pulse produced by ESS and to optimize high flux and high intensity in the so-called fingerprint region $60 \div 220\,\mathrm{meV}$, which is of interest for identifying functional chemical groups [32]. It will offer an almost constant high relative energy resolution in a broad energy transfer range $0 \div 500\,\mathrm{meV}$.

The instrument can be divided into a Primary Spectrometer, whose purpose is to shape and form the beam and to deliver it to the sample, and a Secondary Spectrometer, which processes and delivers the scattered beam to the detector system [30]. The Primary Spectrometer consists of a 51 m long neutron guide having an elliptical profile, and a beam shaping system composed by 5 choppers [33]. VESPA makes use of the so-called Wavelength Frame Multiplication (WFM) technique in order to achieve the main scientific requirement of an energy relative resolution better than 1 % in the broad energy range $0 - 500\,\text{meV}$ [34]. The technique consists in using three Pulse Shaping Choppers (PSCs), closely placed at about 6.5 m to 7.36 m from ESS moderator, that split the source pulse in three sub-frames. In addition to that, a Frame Overlap Chopper (FOC) at 10 m and a sub-Frame Overlap Chopper (sFOC) at 20 m from the moderator centre are needed to prevent the contamination of the sample and to keep them sub-frames well separated in time up to the sample position.

VESPA will be capable of trading flux for resolution depending on the pair of PSCs used. When coupled with the high neutron flux of ESS, such feature will allow to perform in-situ experiments even on bulky samples with a reduced sample area. The high flux can also allow to collect time-dependent data of chemical processes in minutes, and hence to investigate processes evolving in time, like the hydrogen release from materials of interest for hydrogen storage. The high resolution will allow to investigate, and potentially resolve, vibrational modes never resolved before in the very crowded spectral range of the fingerprint region. It will also allow to study the spectra characteristics as a function of the system thermodynamics, and to perform measurements at pressures (several GPa) which are not currently achievable in neutron vibrational spectroscopy [35].

The Secondary Spectrometer consists of a set of Highly Oriented Pyrolytic Graphite (HOPG) crystals that select the neutron energy through Bragg scattering. The high-order harmonics are removed by mean of a beryllium filter, before they reach an array of ^{3}He detector tubes. Diffraction detectors are also included in the Secondary Spectrometer so to enhance the performance of the instrument by providing the unique capability to obtain simultaneous dynamic and structural data [30], and hence to track structural changes in time-evolving systems [35].

VESPA will be capable of producing world-leading science in the field of Neutron Vibrational Spectroscopy, thanks to its high flux, intensity and resolution. Several scientific areas will benefit from its performances, ranging from renewable energy materials, to macromolecular science and cultural heritage [31].

3.2 Instrument

VESPA will be built in the East sector of ESS, at beam-port E7. It is a medium instrument whose sample position is at 59 m from the moderator centre, in direct line of sight with it. A sketch is shown in figure 3.1.

The direction of the E7 beam-port axis forms an angle of 66 ° respect to the proton beam axis. In order to collect a higher flux in the region of interest for VESPA, the instrument is tilted by 0.9 ° so that its axis forms an angle of 65.1 ° respect to the proton beam axis. The tilting allows to collect more neutrons from the very central part of the moderator, so to promote a higher flux in the fingerprint region. These details are illustrated in figure 3.2.

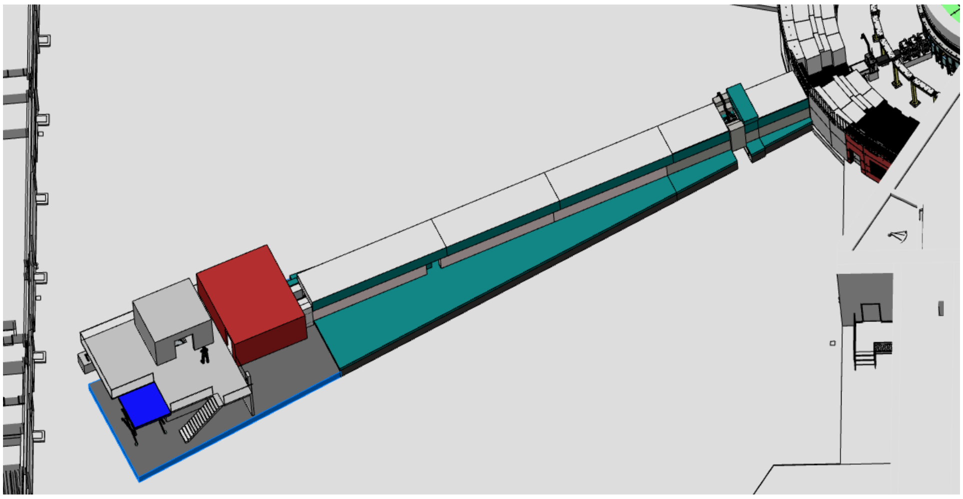

Figure 3.1: VESPA layout [31].

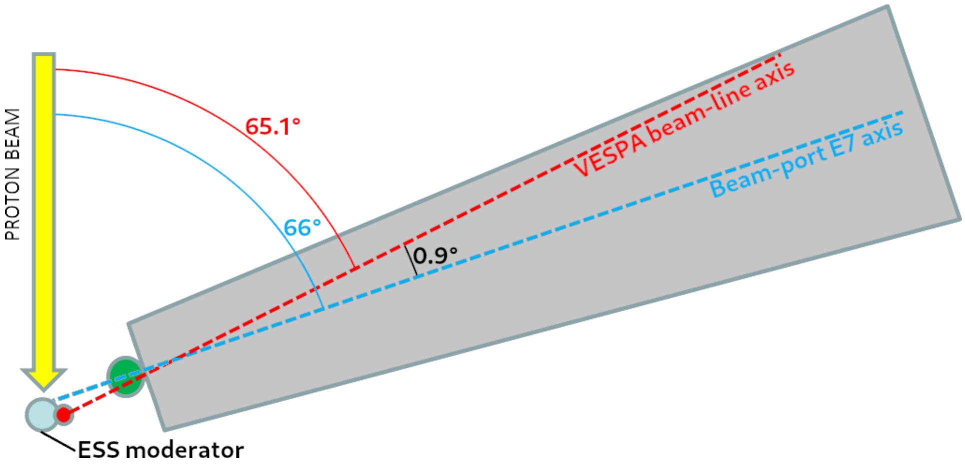

Figure 3.2: Schematic drawing of VESPA beam-line axis that shows its direction respect to the proton beam axis and the E7 beam-port axis. The tilt of 0.9 ° is about the green dot, which is at about ~ 1 m from the moderator centre. Hence, the two angles of 66 ° and 65.1 ° do not share the same vertex [36].

Several guide elements make up the path for the neutron beam from the moderator to the sample. The section of the guide has a rectangular shape of non-costant dimension that gradually changes following an elliptical profile.

Two ellipses shapes the guide, one on the horizontal plane for the profile of the vertical guide internal edges, the other for the horizontal edges in the vertical plane. In particular, the guide has an elliptical profile for the first ∼ 4 m of the beam-line, followed by a constant rectangular section of ∼ 1.5 m, and then another elliptical profile till the sample position [34, 37]. A schematic representation of the guide profile on the horizontal plane is shown in figure 3.3.

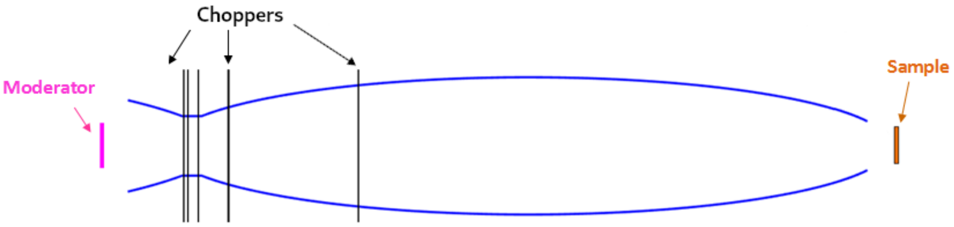

Figure 3.3: Schematic representation of the elliptical profile of the guide on the horizontal plane.

The Primary Spectrometer is completed by other components like the aforementioned choppers, the heavy-shutter and two sets of jaws to shape the neutron beam right before the sample position. A schematic representation of the instrument, showing the position of such components is given in figure 3.4, where the distances are taken respect to the moderator centre.

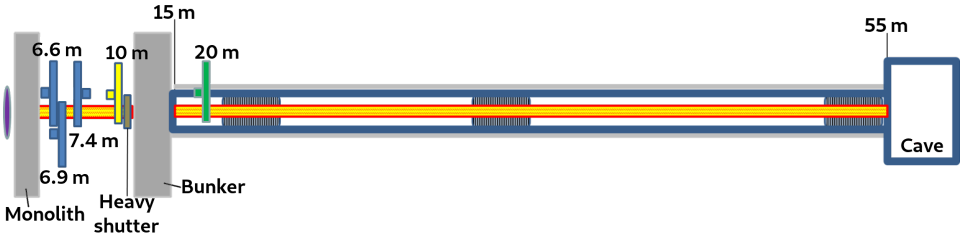

Figure 3.4: Layout of VESPA instrument showing the positions of its main components [33].

The instrument can be divided into two sections respect to the bunker. One being inside the bunker, the other outside, in the experimental hall of the East sector. A description of the instrument in these two sections is given in the following.

3.2.1 Inside the bunker

The section inside the bunker is shown in figure 3.5, which is taken from the engineering design of VESPA.

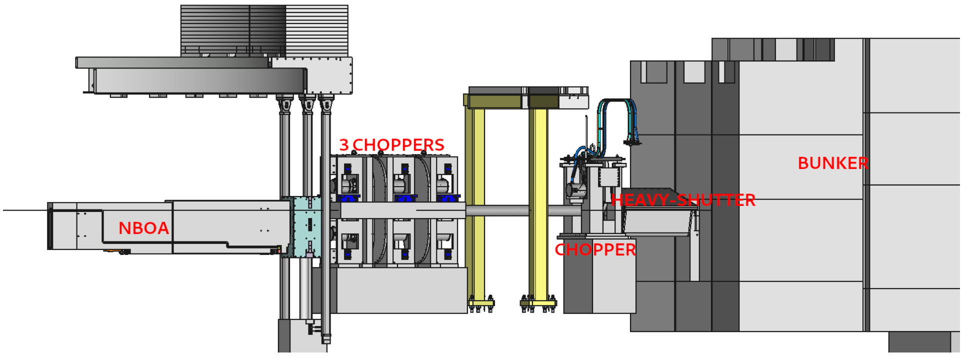

Figure 3.5: Engineering design of VESPA inside the bunker [38].

This section starts in the monolith, with the first component being the NBOA, described in section 2.1.3. It is the first guide section, whose rectangular opening at 2 m from the moderator centre has the following dimensions:

$$4.58 \times 3.51\,\mathrm{cm}^2. \tag{3.1}$$

Those are not preserved along the entire length of 3.5 m of the monolith insert, as can be seen in figure 3.6 that shows the dimensions of both NBOA openings at the monolith entrance and exit.

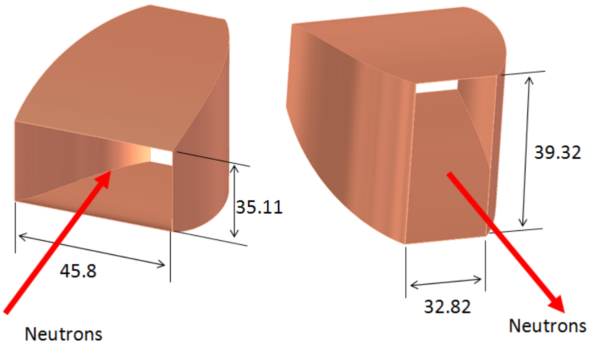

Figure 3.6: Size of the NBOA entrance and exit in the monolith [39].

After the monolith, the instrument extends inside the bunker, where 5 sections of the guide system are installed, including the sections passing through 4 choppers and the heavy-shutter. Each of the first 3 PSCs consists of a pair of counter-rotating discs, sharing the same vacuum box. They are designed to work in couple, two at a time. This will enable a peculiar feature of the instrument, allowing the user to choose between high or low resolution mode, with an increased flux in the low resolution mode.

The 3 PSCs are packed together in a compact block, due to the short distances between them. In fact, they are placed at 6.5 m, 6.8 m and 7.4 m from the moderator centre. The design of such block is shown in figure 3.7.

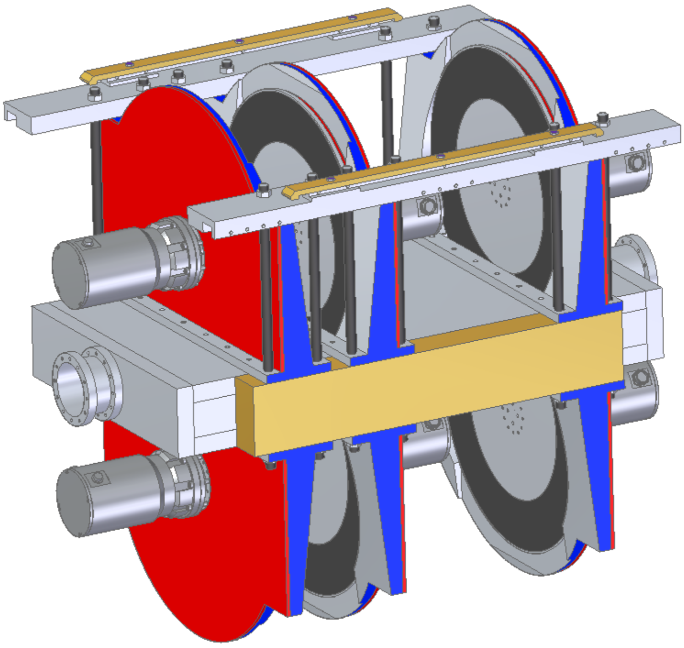

Figure 3.7: Design of the triple of double-disc PSCs inside the bunker.

A fourth chopper, that is a FOC that has only one disc, is placed at about 10 m from the moderator centre and at 1.5 m from the bunker wall. Between that chopper and the bunker wall, the heavy-shutter will be placed. Due to geometrical constraints, the maximum length for such component is about 1.2 m [40].

The heavy-shutter is an attenuator block that consists of materials having high neutron cross sections for absorption and inelastic scattering. In fact, this component is conceived to stop the neutron beam coming from the moderator [41], so to allow a safe access into the experimental cave during operations.

The heavy-shutter is integrated with a guide section of the same length and it is provided with movable parts so to allow remote handling. In fact, this component can be placed into two possible configurations: open or closed. When it is in the open configuration, the guide section is placed in line with the instrument guide, so to allow and improve the neutron transport to the sample. In the closed configuration, the attenuator is in place so to stop the neutron beam.

The last part of the section is constituted by the insert in the bunker wall. Similarly to the monolith feed-through, the bunker wall insert is a component that allows neutrons to go through the wall and exit the bunker. It is integrated with a specific plug to prevent neutron streaming out of the optics.

The opening entrance of this insert has an area of

$$4.50 \times 4.92\,\mathrm{cm}^2, \tag{3.2}$$

while the area of the bunker wall exit is of

$$5.35 \times 5.51\,\mathrm{cm}^2. \tag{3.3}$$

3.2.2 Outside the bunker

Outside the bunker there is the instrument hall. It is a supervised area [17] in which the beam-lines of the instruments and their experimental stations are placed.

In the instrument hall, VESPA will have a $\sim 47\,\mathrm{m}$ long guide section, with an elliptical profile, interspersed with two choppers. It will be provided with sufficient shielding to meet ESS requirements on radiological protection [16].

The first chopper outside the bunker will be Prompt Pulse Suppression Chopper (T0 Chopper) placed as close as possible to the external surface of the bunker wall at 15 m from the moderator centre, while the other, the sFOC, is double-disc chopper placed at $\sim 20\,\mathrm{m}$ from the moderator centre. The former is an additional sixth chopper, whose current design is still not available [33], that will not be part of the instrument at day one. VESPA will be built with a total of 5 choppers, but the additional chopper next to the bunker will be added later, as part of the first upgrade stage [31].

At the end of the $\sim 45\,\mathrm{m}$ long section, the instrument has the experimental cave, the sample preparation area and the hutch [42], which are not in the scope of this thesis.

- Experimental cave: it allows to access to the spectrometer and a number of utilities. It consists of two rooms that are placed one above the other. The one at the bottom contains the spectrometer, while the other allows to put the sample in position.

- Sample preparation area: it contains the equipment and utilities for preparing the samples and for temporarily storing those which are irradiated.

- Hutch: users and instrument personnel are expected to spend most of their time in this area. Here they can remotely monitor the instrument, control technical components and analyse the data.

The design of these areas is in progress by the time of writing of the present work. Their current draft design is shown in figure 3.8, where a detail is given on the lower cave and the Secondary Spectrometer. Also the design of the latter has still to be finalized, however a few pictures of the current state of work is given in figure 3.9.

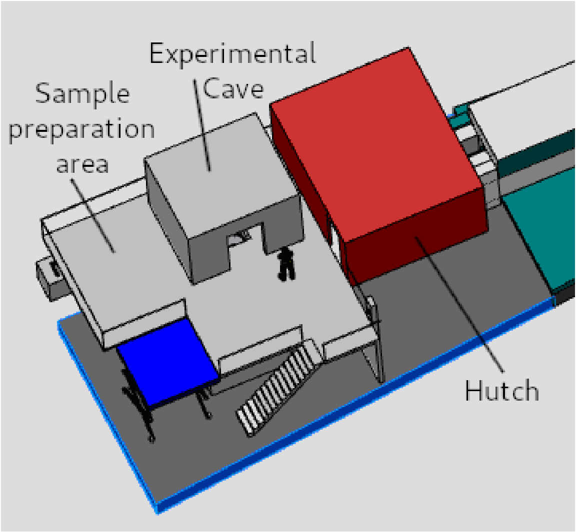

(a)

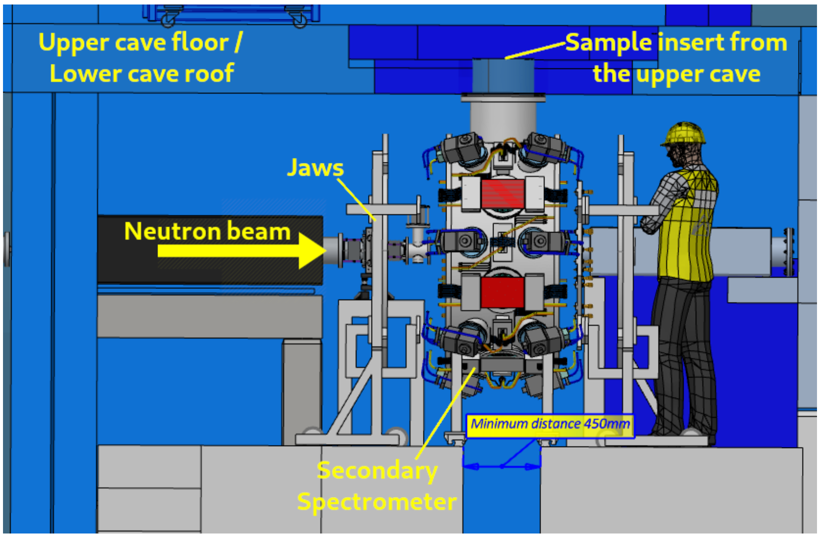

(b)

Figure 3.8: (a) Current design for the hutch, cave and sample preparation area of VESPA [31]. (b) Concept design VESPA lower experimental cave, showing the Secondary Spectrometer and the sample insert from the upper cave [43].

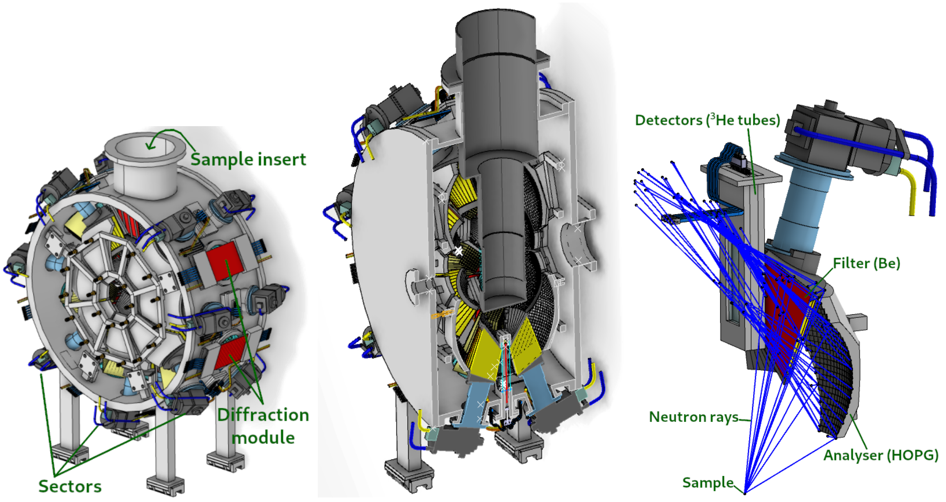

(a) (b) (c)

Figure 3.9: Overview (a) and a vertical section (b) of the Secondary Spectrometer. It is constituted of two symmetrical halves, each consisting of 6 diffraction modules and 7 vibrational spectrometer modules, one of which is shown in (c) [43].

The instrument hall outside the bunker is designed as a supervised area, so to allow a more frequent access than the area inside the bunker [17]. Because of that, different radiological dose requirements apply for the two areas [16]. In order to meet such requirements in the halls, the instruments have to be provided with an appropriate shielding. Hence, the entire section of VESPA in the hall has to be designed with an adequate shielding. In particular the present work presents the proposed design for the shielding of the section between the bunker wall and the sample position in the cave.

3.3 MCNP model

The engineering model of the instrument is not in the correct format for performing simulation using MCNP. Since it is meant for manufacturing purposes, it is over-detailed and thus it's not suitable for performing Monte Carlo simulations [44].

The need for a model which is expressly conceived for MCNP was initially met by CombLayer, which is a geometry builder and a variance reduction system for MCNP and other Monte Carlo codes [45, 46]. An early version of VESPA model is available in its repository. Such model was edited by using the details from the engineering model [38] and several internal documents for VESPA [36, 33]. The work resulted in a model shown in figure 3.10, that was updated in a dedicated branch of CombLayer [47].

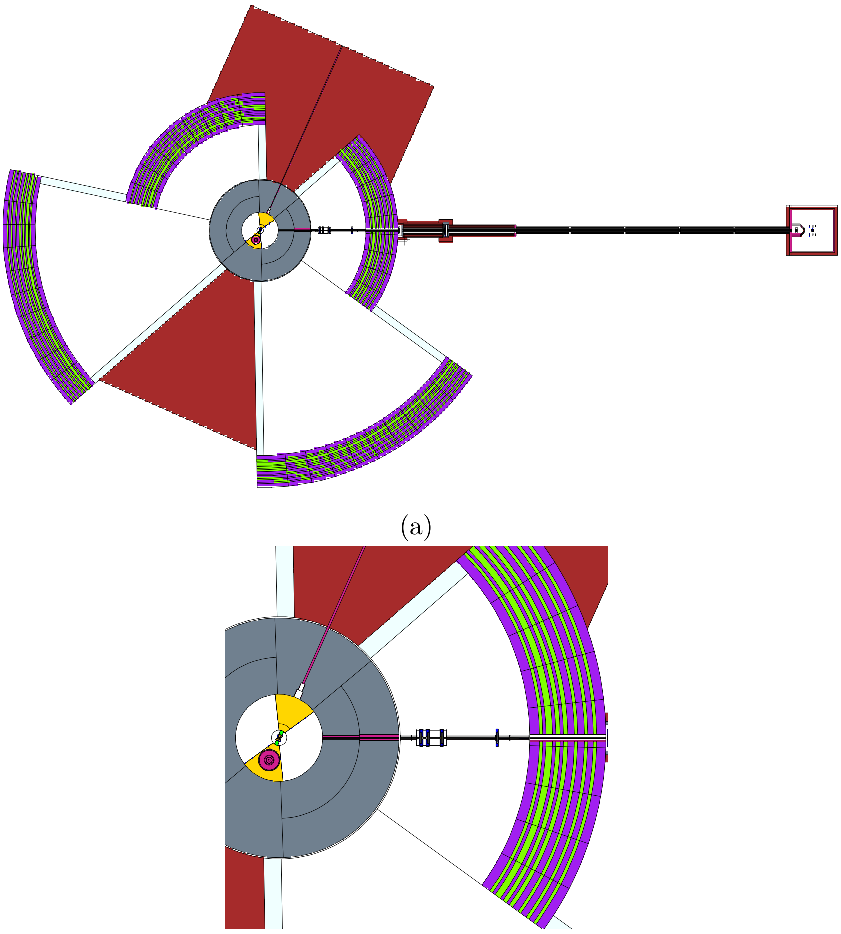
(a)

(b)

Figure 3.10: Top-views of VESPA MCNP model (a) and a detail of the area inside the bunker (b), from the dedicated branch of CombLayer [47].

The revised model [47] was used as a starting point for setting up a completely new model from scratches, without using CombLayer. This was a decision taken for having a complete knowledge of the model, and also to further simplify the model, e.g. by removing most of the bunker and of the TMRA. The resulting model, shown in figure 3.11, was built using the materials defined in CombLayer, that can be found in appendix B.

The discs of the choppers that will be built for VESPA are provided with a set of slits in specific angular positions. The purpose of the choppers is to shape and to remove the undesired energetic component of the neutron beam before it reaches the sample. For that, the chopper blades, which are the annulus sectors between the slits, will be made of appropriate materials. However, the blades were not reproduced in the MCNP model because the worst case scenario considered is the one in which all choppers are in a fully open configuration. It is also a common scenario for all the instruments involved in the project. Hence, all the neutronic calculations presented in this work were performed with all the choppers in a fully open configuration. The only exception is for the blades of the sFOC, which were considered in the model for one calculation in a fully closed configuration with a thermal neutron beam. The case in which the full beam from the moderator hits the sFOC in a closed configuration is beyond the scope of the Common Shielding project, since it's part of the studies on the risk assessment which are on their initial phases at the time of reviewing this thesis (May 2020) [48].

Figure 3.12 shows both the MCNP model and the engineering model of the first triplet of choppers, which are here considered as representative. The picture that shows the MCNP model was taken using the MCNP geometry viewer, which only draws the cells and surfaces that intersect the portrayed section. The viewer for the engineering model, instead, also shows other objects like the chopper engines and guide that appear to be missing in figure 3.12(d).

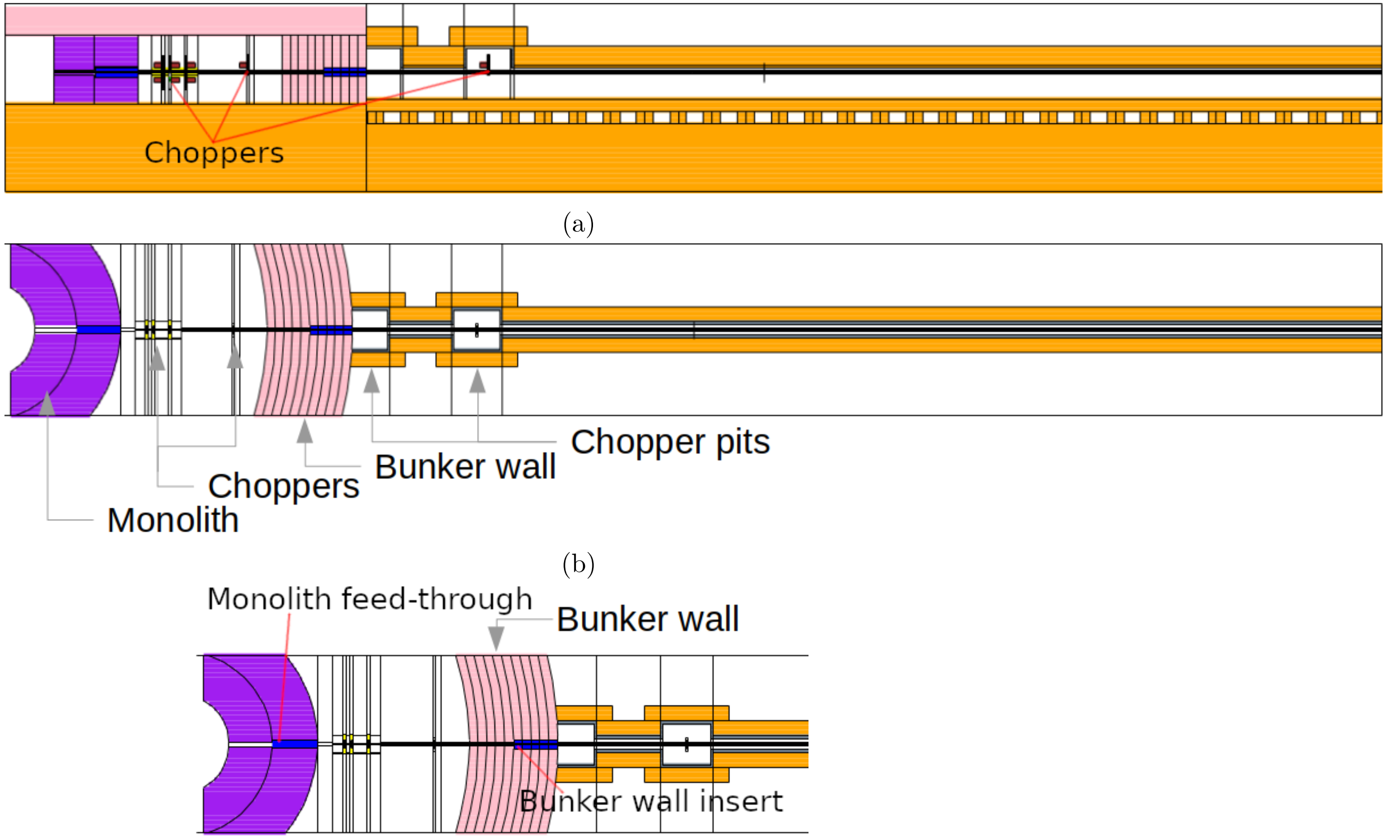

(a)

(b)

(c)

Figure 3.11: Side-view (a), Top-view (b) and a detail (c) of the first section of the MCNP model of VESPA, used for performing the calculations presented in this thesis.

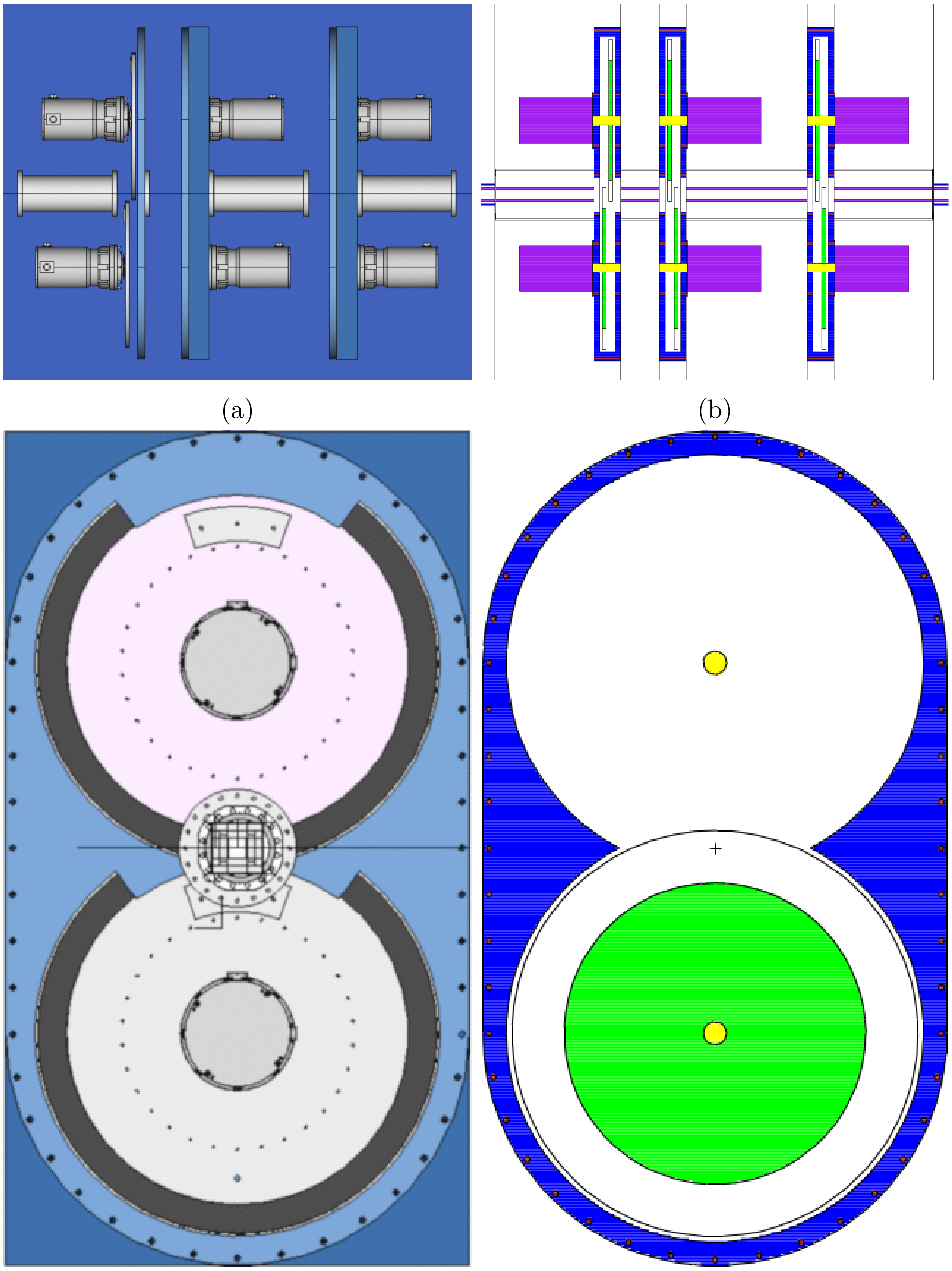

(a) (b)

(c) (d)

Figure 3.12: Comparison between the engineering model (a, c) and the MCNP model (b, d) of the first triplet of choppers of VESPA inside the bunker.

Chapter 4

Fictive neutron sources

Stochastic simulations that use models of the target monolith and of the proton source can be very inefficient for designing any beam-line shielding [49]. The need to reproduce the entire spallation process and to transport neutrons at long distances puts a burden which is hard to overcome, even using advanced variance reduction techniques [49]. A possible alternative used in similar works [50] is to calculate a source term, that is a fictive neutron source placed in a convenient position.

Two source terms are presented in this chapter, the first being produced by V. Santoro et al. [51]. The second source was produced at the bunker wall entrance, at 15 m from the moderator centre. It was generated using the first one as source so to relieve the needs for variance reduction techniques for designing the beam-line shielding of VESPA.

In order to distinguish the source term produced by ESS from the second one that was calculated for studying VESPA beam-line shielding, the first is addressed in this text as primary source term, the latter as secondary source term.

The two source terms find different applications in the fields investigated in the present work. One was used to determine the design of the heavy-shutter, while the latter was used for designing the beam-line shielding.

4.1 ESS source terms

A source term is a fictive source that generates neutrons using appropriate probability density functions. Such functions are determined by benchmarks with the results of other simulations that make use of another reference source. The purpose is to design the source term so that it reproduces the same spectrum and the particle flux of the reference source. The calculation and hence the use of the source term allows to bypass the use of that original source. Hence, the need to use of variance reduction techniques can be relaxed or avoided by using a source term.

At ESS the most natural choice for studying some neutronic quantity is to design a proton source that reproduces the proton beam a few centimetres before it hits the target. Such source is defined as a flat rectangular surface of appropriate size that emits protons according to the physical parameters given in table 2.1.

In order to have estimations of some neutronic quantity using the proton source, the simulation has to reproduce at least part of the TMRA. Depending on the case-study under examination, further elements have to be added in the model. If the purpose is similar to studying a particular beam-line as the case presented in the present work, additional elements like the monolith, the bunker and part or the entire instrument have to be modelled.

Once the geometrical model is ready and the proton source is set, the simulation has to simulate the entire spallation reaction in order to obtain some neutronic estimation. Generating neutrons by reproducing all the processes involved in the reaction is a time consuming task. Furthermore, the resulting neutron angular distribution is another disadvantage when the purpose is to study one of the beam-lines. In fact, although spallation neutrons of energies higher than 20 MeV have a strong angular dependence, neutrons of lower energies show almost an isotropic angular distribution [24]. The isotropy is further favoured by the multi-scattering interactions that take place in the moderator system, and that contribute to slow down neutrons of energies higher than 20 MeV. On the other hand, each of the beam-lines extends in a particular radial direction from the TMRA. Thus the natural geometry of the case-study is adverse to the simulations, since only few of all the generated neutrons happen to find their way toward the beam-line under examination.

The high complexity of the MCNP model, the almost isotropic neutron distribution and the additional burden on the required computational time due to the spallation reaction are a drawback in using the proton source for studying the beam-lines. The investigation of ESS on this issue resulted in six sets of source terms, each set for a different beam-line. The beam-lines were chosen so to cover a broad range of possible angular positions around the TMRA [51], as can be seen in figure 4.1. The monolith feed-through of VESPA is added to the picture as a reference, since it didn't benefited from that work.

The source terms provided by ESS were calculated following one of the methodologies investigated by F. Gallmeier et al. in [52]. Each of them consists of a rectangular surface, perpendicular to the beam-line axis. The surface is placed at the NBOA opening in the monolith, at 2 m from the moderator centre. A representative beam-line is shown in figure 4.2 in which the position of the source term is highlighted.

Each of the source terms calculated by ESS generates neutrons in the direction of the beam-line axis. The initial emission angle for each neutron

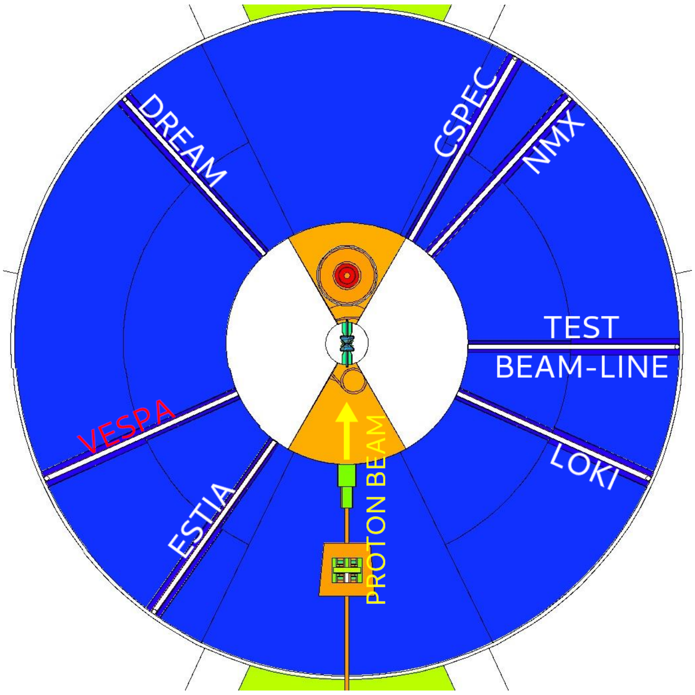

Figure 4.1: The full suite of beam-lines for which ESS calculated the source terms. VESPA is not in that list, but it is added for reference.

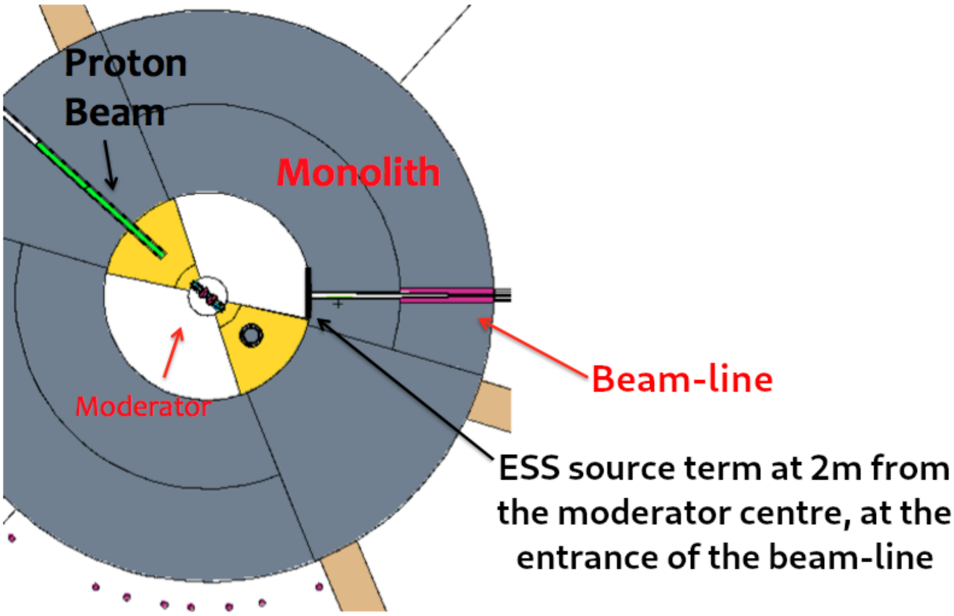

Figure 4.2: MCNP model of the TMRA showing the position of ESS source term for a representative beam-line [51].

is sampled from a proper angular distribution. The characterization of such distribution is a very sensitive part in defining the source terms. It has to be chosen so to be sufficiently fine to reproduce the angular distribution of neutrons generated by the original proton source in the surface area of the source term. On the other hand, it can't be excessively refined in order to allow to adequately sample the angle and energy distributions.

For each point on the source surface, the angle of emission is taken respect to a line parallel to the beam-line axis. The solid angle is therefore subdivided into concentric cones as sketched in figure 4.3, each having an appropriate probability of being sampled.

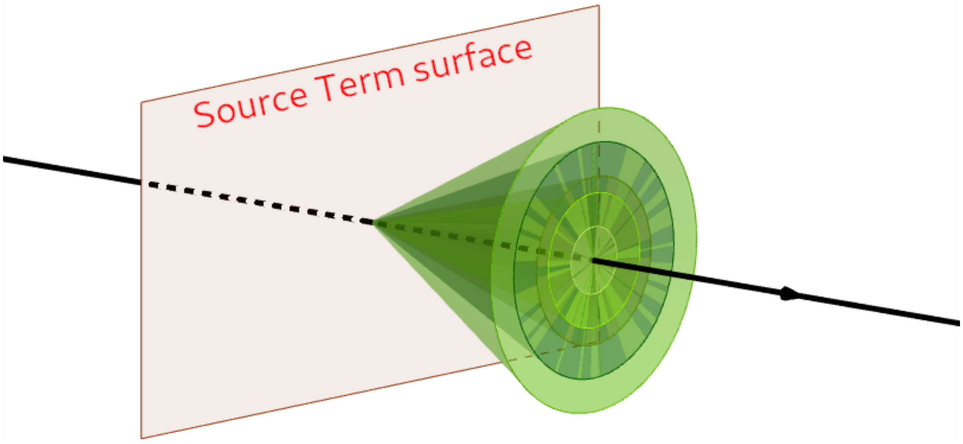

Figure 4.3: The solid angle about a line parallel to the beam-line axis is subdivided into concentric cones.

All the source terms provided by ESS use an angular distribution consisting of eleven not equally spaced angular bins. Each of these probability density functions is unique for the considered source term, even if they are part of the same set of sources for a specific beam-line. Choosing a specific source hence uniquely determines the angular distribution.

VESPA is not in the list of those beam-lines that benefited from ESS source terms. However, due to geometrical reasons it is still possible to exploit one of the available source terms. The TMRA is almost symmetric respect to the proton beam axis. In fact, the vertical plane that crosses the proton beam axis virtually splits the TMRA and the bunker into two parts, each of which having a short sector and a long sector. It is reasonable to expect that beam-ports at symmetrical positions respect to that plane show comparable neutron fluxes and spectra [53]. The only major difference between the two halves is in the TMRA, due to the shape of the moderator and reflector plug, as can be seen in figure 4.1 and in figure 2.4.

VESPA will be built in the EAST short sector, at E7 beam-port.

The symmetrical beam-port respect to the proton beam direction is the N7 beam-port, which is used by LOKI instrument. LOKI is one of the instruments that benefited of ESS source terms. Thanks to the symmetry of the two beam-ports, it is possible to exploit the calculated LOKI source terms for performing studies on VESPA instrument.

4.2 Primary source term

ESS calculated five different source terms for LOKI, each with a different size for the rectangular surface area. The complete list of those sizes is shown in table 4.1.

	Width × Height (cm^2)				
LOKI	8×3	8×5	8×8	8×10	8×12

Table 4.1: LOKI source terms calculated by ESS.

The selection for the best source to be used for VESPA was based on the size of surface area of the available sources for LOKI. It allows to introduce the smallest possible discrepancy between the estimations from the original source and those from the source term.

The best source term for VESPA is that whose surface size is the closest as possible to that of its NBOA opening. Such opening in the monolith has a size given in equation 3.1. Among the source terms calculated for LOKI, the one with a surface area of $8 \times 5\,\mathrm{cm}^2$ was chosen for being used for VESPA studies.

The source chosen for VESPA, which is addressed as primary source term in the rest of the text, is characterized by the angular distribution shows in figure 4.4. The non-zero height of the bin at $90 - 180\,^\circ$ shows that the primary source emits neutrons also in a backward direction, toward the monolith. However it has to be noted that such bin covers half of the spherical solid angle. If the sum of the other bins is considered, the fraction of neutrons going backward is negligible. A similar argument can be given for the bin in the range $5 - 10\,^\circ$, which should be more properly compared to the sum of the first bins from $0\,^\circ$ to $5\,^\circ$.

Apart from the emission angle, each neutron is generated with a proper initial energy. It is sampled from a given energy spectrum, which is uniquely determined once the emission angle is selected. At each bin of the angular distribution corresponds a unique specific neutron spectrum. The complete set of neutron spectra is shown in figure 4.5, where their ordinates are reported as calculated by ESS in the document [51]. MCNP doesn't use such absolute values but normalizes them, so that each spectrum is used as probability density function for sampling the initial energy.

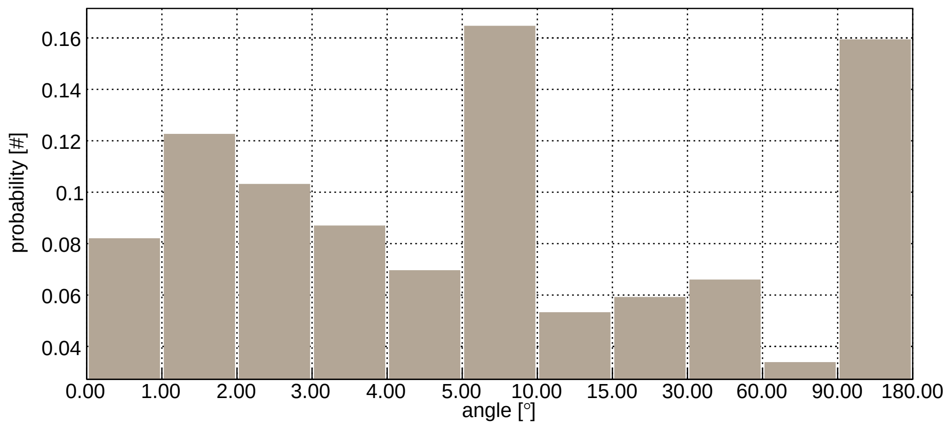

Figure 4.4: Probability density function used for sampling the emission angle from the primary source term.

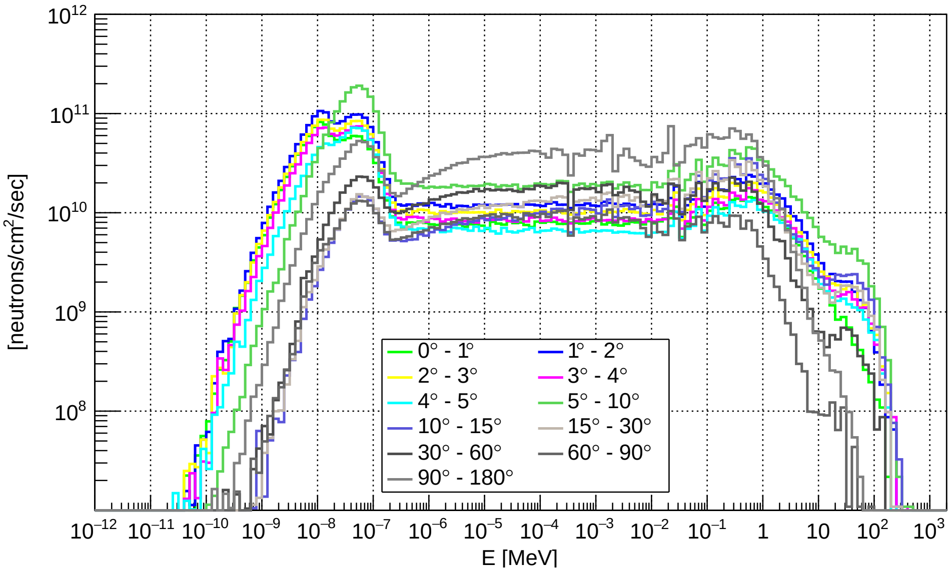

Figure 4.5: The neutron spectra used for sampling the initial energy of neutrons generated by the primary neutron source term.

The simulations that use a source term can run much faster, up to $\sim 10^{3-4}$ times faster when using the primary source term [53], and can avoid or at least reduce the need for variance reduction techniques. The results have to be normalized so that they match those produced using the reference proton source. The benchmark consists in comparing the neutron spectra that the two sources produce at specific locations at the exit of the NBOA, at 5.5 m from the monolith centre. All the source terms calculated by ESS are thus provided with appropriate normalization factors. The one given for the the source term chosen as for the primary source for VESPA is:

$$\sim 2.012 \cdot 10^{13}\,\mathrm{sp/sec.} \tag{4.1}$$

4.2.1 Setting up the primary source term

The normalization factor of equation 4.1 is valid for the original surface area of $8 \times 5\,\mathrm{cm}^2$ of the chosen source term. That size is bigger than the NBOA opening of VESPA. If it is not resized to fit it, a fraction of neutrons would be generated in the cast iron of the monolith, and thus they would have a small chance to contribute to the estimations requested on the simulation. In order to avoid that, the size of the surface was changed so to fit that of VESPA NBOA opening.

The resizing of the primary source term leads to the need to change the original normalization factor of equation 4.1. That coefficient represents the number of neutrons that crosses the source term surface per second, that is the particle current across that surface. Such current depends on the size of the surface, so that if it is smaller, the current is expected to be logically lower. Because of that, the normalization factor was scaled down by the ratio of VESPA NBOA opening size to the original size

$$2.012 \cdot 10^{13}\,\mathrm{sp/sec} \cdot \frac{4.58 \times 3.511}{8 \times 5} \simeq 8.088 \cdot 10^{12}\,\mathrm{sp/sec.} \tag{4.2}$$

The assumption that led to rescale the normalization factor as shown in equation 4.2 is that the particle current can be considered almost linear with the area of the surface. Such assumption was tested and the result was improved by performing a similar benchmark as that performed by ESS, between the results produced by the source terms and the original proton source.

Since the output of MCNP simulations are normalized to one source particle *sp*, those simulations that use a model of the target and the proton source need an appropriate normalization factor. It can be calculated by recalling that

$$1\,\mathrm{mA} = 6.24 \times 10^{15} e/s, \tag{4.3}$$

where e is the absolute value of the electric charge of the electron, which coincides with that of a proton, $e = sp$. Hence the normalization factor which has to be used for getting results normalized to one second is

$$6.24 \times 10^{15}\,\frac{e}{\mathrm{s}\cdot\mathrm{mA}} \cdot 2.5\,\mathrm{mA} = 1.56\,\frac{sp}{\mathrm{s}}, \tag{4.4}$$

which represents the average amount of protons that are conveyed to the target at each second.

The neutron spectra produced from two different simulations, performed on two different machines, at 5.5 m from the monolith centre, were compared. The geometry of the simulation in which the primary source was set, is presented in paragraph 3.3 and shown in figure 3.11. The other simulation that was set up with the proton source makes use of the MCNP model shown in figure 3.10 and available from [47]. That model is older than that used by ESS for calculating the source terms.

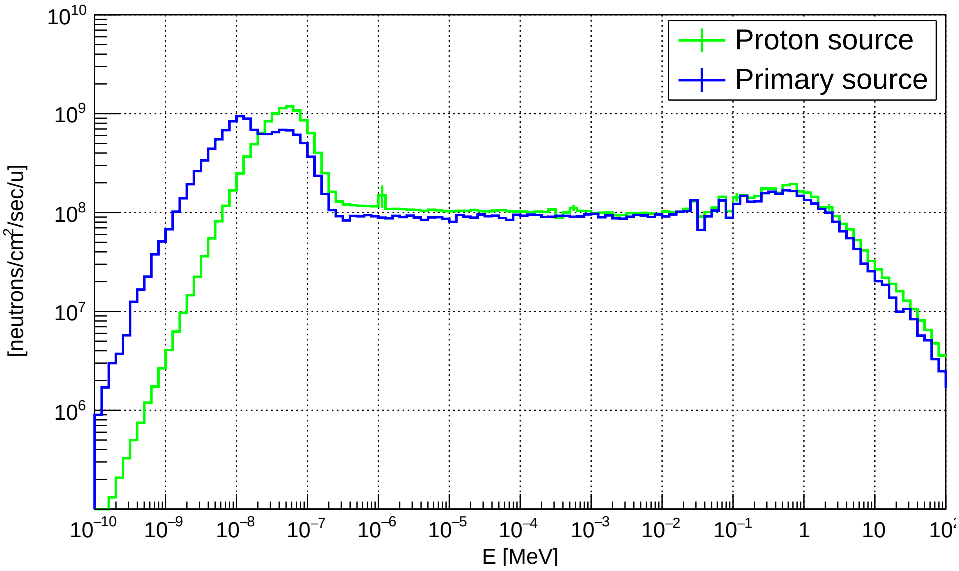

Figure 4.6: Neutron spectra in lethargy units produced by the primary source and the proton source, at 5.5 m from the monolith centre.

The spectra in figure 4.6 show a discrepancy in the thermal and sub-thermal region, below $\sim 1 \cdot 10^{-7}$ MeV. It is to be attributed to a cross-section library for para-hydrogen that wasn't available on the machine in which the spectrum from the proton source (green line in figure 4.6) was simulated. In fact, the spectrum of the primary source shows an additional peak at cold energies, below $2.5 \cdot 10^{-8}$ MeV, that can be produced only by the para-hydrogen in the cold moderator.

If the direct contribution of neutrons to the dose is considered, slow neutrons have a negligible impact on that, as shown by the flux to dose conversion function for neutrons in figure 1.4(a). On the other hand, due to their high chance to be captured, they can contribute to the total dose through the emission of gammas in neutron capture reactions. However it is expected that the dose rates of a straight beam-line in line of sight with the moderator are dominated by fast neutrons, as observed for similar beam-lines [54].

Although the spectrum from the primary source is lower than that of the proton source especially in a fraction of the energy range $10^{-8} - 10^{-7}$ MeV, it has a larger integral area for energies below $\sim 1 \cdot 10^{-8}$ MeV. Thus, it can produce slightly overestimated and hence conservative results, which do not constitute an issue for shielding calculations. Apart from the sub-thermal region, the benchmark already shows a good match between the primary source and the proton source. However the rescaled value given in equation 4.2 can be further improved by considering an additional multiplicative factor.

Assume to label the content of each bin of the spectrum produced by the primary source as s_i, and the analogous bin for the proton source as p_i. The following quantity ξ can be considered

$$\xi = \sum_i (x \cdot s_i - p_i)^2. \tag{4.5}$$

It is the sum of the euclidean distances between the ordinates of the two spectra. The quantity x is a dimensionless multiplicative constant that can be varied so to find the minimum of ξ. That value of x that minimizes ξ is the additional multiplicative factor that has to be applied to the normalization factor 4.2 so to achieve the best match between the two spectra in figure 4.6.

Two different cases were considered, one in which the sum 4.5 is performed over all energies, while in the other the sum is performed only for energies above 1 eV. For the former case, the value of x that minimizes ξ is about 0.9, in the latter it is 1.13. Such values correspond to the minima of the parabola shown in figure 4.7. The parabolic shape is due to the form of the equation 4.5, where it is clear that ξ is a second order polynomial in x.

The effect of the additional multiplicative factor x on the spectra at the monolith feed-through exit is shown in figure 4.8, where the red curves represent the spectrum from the primary source term after being rescaled by $x = 1.13$ in one case, and by $x = 0.9$ on the other.

The additional factor x is close to unity in both cases, when calculated over all energies and for energies above 1 eV. In the former case the minimum of the parabola is at $x = 0.9$, lower than unity. That is due to the higher thermal region in the spectrum produced by the primary source term. Although such value of x would optimize the match between the primary source spectrum and the proton source spectrum, it scales down the total neutron flux. The case where $x = 1.13$ scales up the flux instead, due to the fact that the spectrum is multiplied by such factor x greater than 1. Such

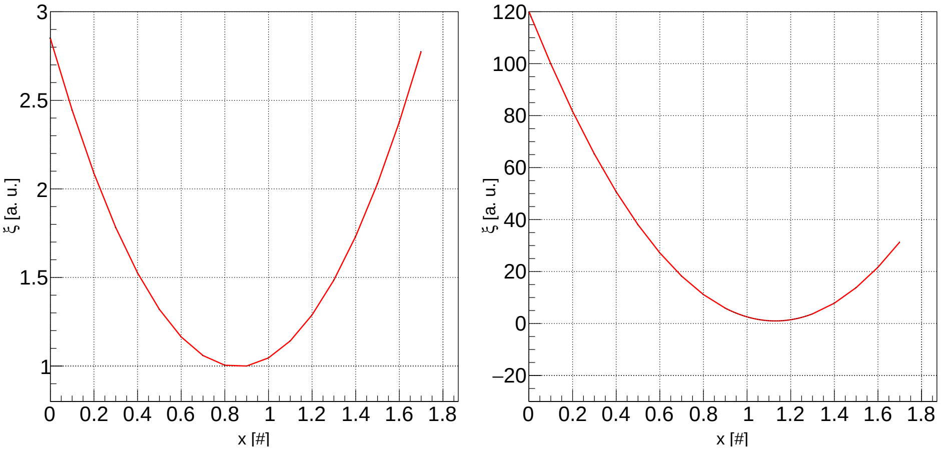

(a) (b)

Figure 4.7: Graphs of the quantity ξ as a function of x when the sum of equation 4.5 is performed over all energies (a) and for energies above 1 eV (b).

latter case was chosen as the additional factor $x = 1.13$ for the equation 4.2. The choice is not only because fast neutrons are of more concern for straight beam-lines, as for the case of VESPA, than the gamma contribution due to slow neutron capture, but also because the thermal region in the spectrum from the proton source is not reliable due to the missing para-hydrogen library.

The resulting normalization factor for VESPA primary source is the following:

$$8.087781493 \cdot 10^{12}\,\text{sp/sec} \times 1.13 = 9.139193087 \cdot 10^{12}\,\text{sp/sec}. \tag{4.6}$$

Apart from the simulations needed for tweaking the normalization factor, all the calculations presented in this thesis were performed using the primary source term.

4.3 Secondary fictive neutron source

The primary source term allows to relax the need for variance reduction techniques, but it is still not sufficient for completely avoiding them if the purpose is to study the beam-line shielding in the hall. In fact, the source is placed at 2 m from the moderator centre, at the entrance of the 3.5 m NBOA in a thick bulk of cast iron, that is the monolith. Then neutrons have to travel for 8 m inside the bunker before they go through the 3.5 m thick bunker wall of heavy concrete.

Both the bunker wall and the monolith are designed with the purpose of attenuating the neutron dose rates to appropriate levels. They are two

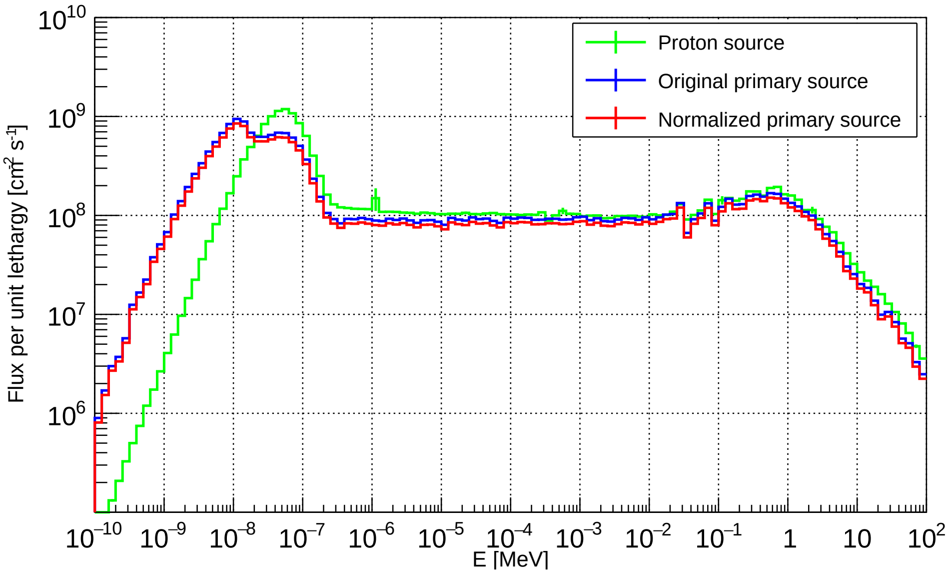

(a)

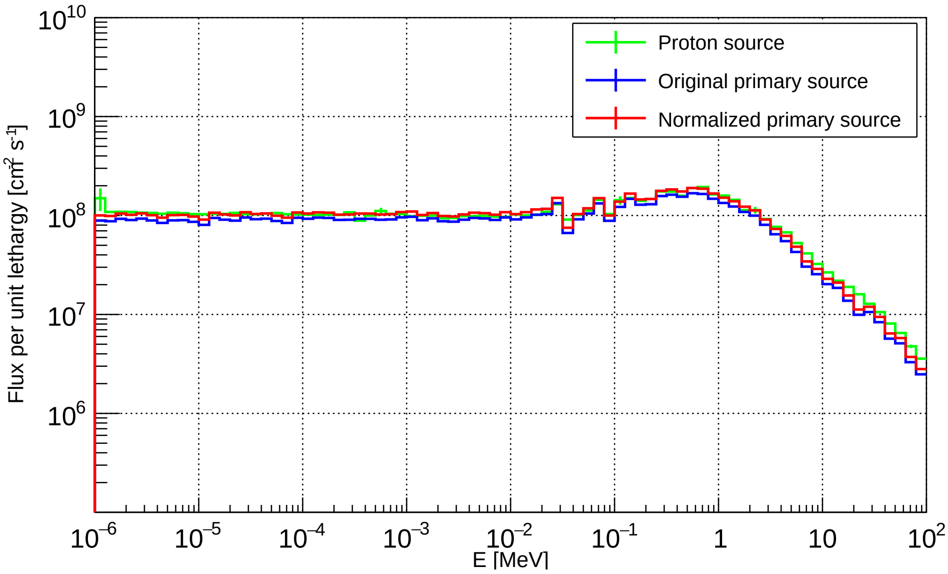

(b)

Figure 4.8: Benchmark spectra of figure 4.6 on which a third curve in red is superimposed, which represent the spectrum calculated by the primary source term after being rescaled by $x = 0.9$ (a) and by $x = 1.13$ (b).

shielding blocks that put a burden for performing pure analog Monte Carlo calculations, even if they are provided with feed-throughs along their thickness. In fact, those inserts have roughly a cross section area of about $4 \times 4\,\mathrm{cm}^2$, which is not sufficiently wide to let all the neutrons, generated within the first angular bin of figure 4.4, to travel in a straight line across both the bunker wall and the monolith.

As sketched in figure 4.9, those neutrons generated with an emission angle $\alpha = 1°$, have to travel for about

$$\frac{2\,\mathrm{cm}}{\tan(1°)} \simeq 1.15\,\mathrm{m} \tag{4.7}$$

so to reach a distance of 2 cm from the beam-line axis. That means that neutrons generated with an emission angle $\geq 1°$ interact with the monolith, and thus they can be absorbed or scattered in a unfavourable direction. Only those neutrons emitted with an angle lower than

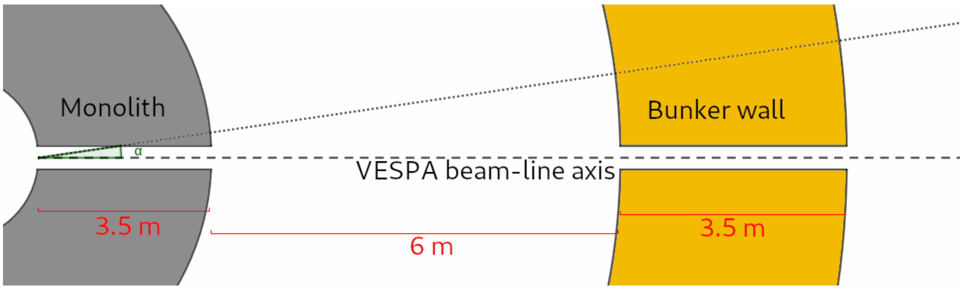

Figure 4.9: Sketch of the first section of VESPA beam-line showing the angular opening of the primary source term.

$$\arctan\left(\frac{2\,\mathrm{cm}}{9.5\,\mathrm{m}}\right) \simeq 0.12° \tag{4.8}$$

can reach the bunker wall entrance at 9.5 m from the source. That means that only one tenth of the neutrons emitted in the first angular bin of the primary source can have a chance to travel unscattered till that entrance. In other terms, the monolith acts as collimator for the neutron beam.

The geometry of the first section of the beam-line requires to use variance reduction techniques in order to transport neutrons out of the bunker. Once there, they have to be transported through an additional shielding structure around the beam-line for other $\sim 55\,\mathrm{m}$. Instead of refining an efficient variance reduction technique, it was chosen to try to determine a secondary source term, following the same procedure by F. Gallmeier [52], that was used to calculated the primary source.

Gallmeier suggests an alternative approach that consists of subdividing the source surface into a matrix of smaller surfaces. Gallmeier in [52] is a higher freedom due to the higher number of parameters.

4.3.1 Suitable positions

The secondary source term has to be defined in a position which is suitable for designing the beam-line shielding of VESPA. The source also has to increase the chances for the neutrons to survive both the monolith and the bunker wall, so to contribute to the desired estimations in the hall. These two requirements lead to investigate two possible positions in the bunker wall:

- bunker wall entrance, at 11.5 m from the moderator centre,
- bunker wall exit, at 15 m from the moderator centre.

The position at the exit of the bunker wall might look like the best choice for promoting the transport of neutrons for beam-line shielding studies. However it must be noted that such choice would underestimate or result in bad estimations of the shielding structure next to the bunker wall. Hence such section of the shielding should be investigate using the primary source term.

On the other hand, the position at the bunker wall entrance would prevent such issue but might not completely avoid the use of variance reduction techniques. In fact, it would not avoid the the need to transport neutrons through the bunker wall.

4.3.2 Angular binning

The geometrical arguments discussed in paragraph 4.3 give clues about the expected angular distribution for a secondary source term at the bunker wall. Only a small fraction of neutrons, generated with small emission angles, can have the chance to travel in a straight line till the bunker wall feed-through. This suggests that the neutron beam in the bunker wall insert is expected to have a small divergence and, thus, the investigations should focus mainly on the first couple of degrees about the beam-line axis.

Two angular binning were investigated in great detail for calculating the secondary source term. Their bin boundaries in degrees are reported in table 4.2. The angular binning characterized with wider bins is addressed in the rest of the text as *coarse binning*, in contrast with the other which is called *fine binning*.

Coarse	0 - 0.1 - 0.2 - 0.3 - 0.4 - 0.5 - 0.7 - 0.9 - 1.1 - 180
Fine	0 - 0.05 - 0.1 - 0.15 - 0.2 - 0.25 - 0.3 - 0.35 - 0.4 - 0.45 - 0.5 - 180

Table 4.2: The two angular binning investigated for calculating the secondary source term.

4.3.3 Secondary source term candidates

A set of three candidate secondary source terms were calculated in the two positions discussed in paragraph 4.3.1. The following list shows the position in which they were calculated and which angular binning they use:

1. bunker wall exit, coarse binning,
2. bunker wall exit, fine binning,
3. bunker wall entrance, fine binning.

They are listed in the chronological order in which they were investigated.

A secondary source at the bunker wall exit is expected to inadequately estimate the doses for the shielding structure next to the bunker. However, it could minimize the use of any variance reduction technique. For this reason, the position at the bunker wall exit was investigated first.

The additional choice to use the coarse binning was taken for the smaller number of spectra required to define the source respect to those required by the fine binning. The coarse binning would in fact require less source particles for a sufficient sampling of the source spectra and the emission angles. A fine binning is expected to generate more spectra for the sources, and hence to better describe the neutron angular distribution about the beam-line axis due to the more refined binning.

Three candidate source terms were produced. The simulations performed to define them were set so to use the primary source term. The purpose of the calculations was to estimate the neutron current that crosses the opening surface areas at the entrance and at the exit of the bunker wall insert. In particular, they estimate the energy and angular dependencies of that neutron current.

The resulting angular distributions from the simulations are shown in figure 4.10, while the spectra associated to each angular bin are given in figure 4.11.

The heights of the angular distributions in figure 4.10 represent the integral areas of the spectra shown in figure 4.11. Since those angular distributions are used as probability density functions in MCNP, they are normalized to unity.

All the three angular distributions in figure 4.10 show that the neutron beam at either the bunker wall entrance and exit has a small divergence about the beam-line axis. In fact, in all the three graphs the ranges in angles which are coloured in grey correspond to bins whose associated probability is $\sim 5 - 6$ orders of magnitude lower than those at smaller angles. That means that the contribution coming from those bins in the grey area, which starts at 0.3° in figure 4.10(a) and figure 4.10(b) and at 0.3° in figure 4.10(c), is negligible respect to those at smaller angles. The same doesn't hold for the last angular bins: that from 1.1° to 180° for the coarse binning, and the

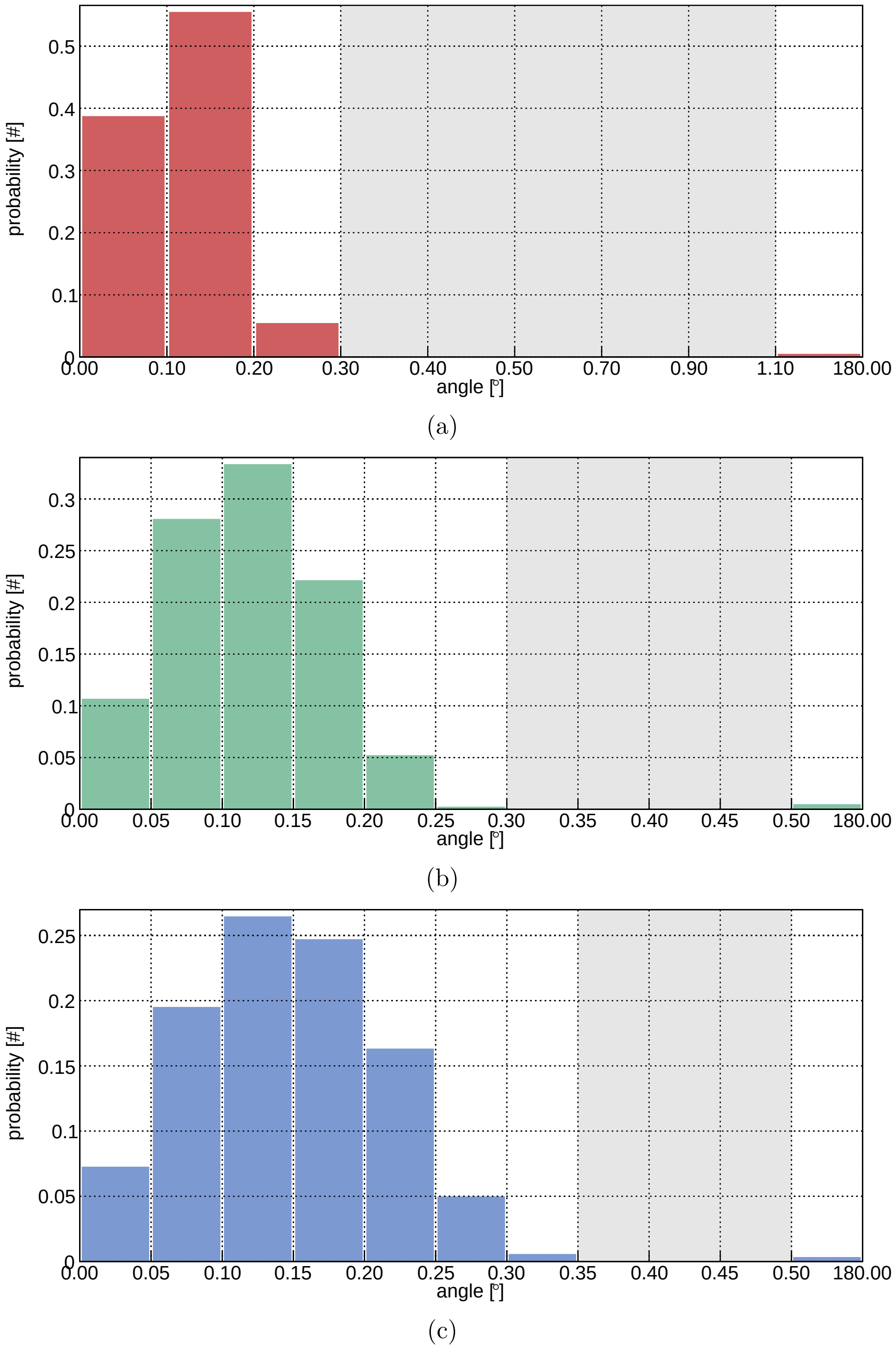

(a)

(b)

(c)

Figure 4.10: The angular distributions for the candidates source terms at the bunker wall exit (15 m) with a coarse binning (a), at the bunker wall exit (15 m) with a fine binning (b) and at the bunker wall entrance (11.5 m) with a fine binning (c).

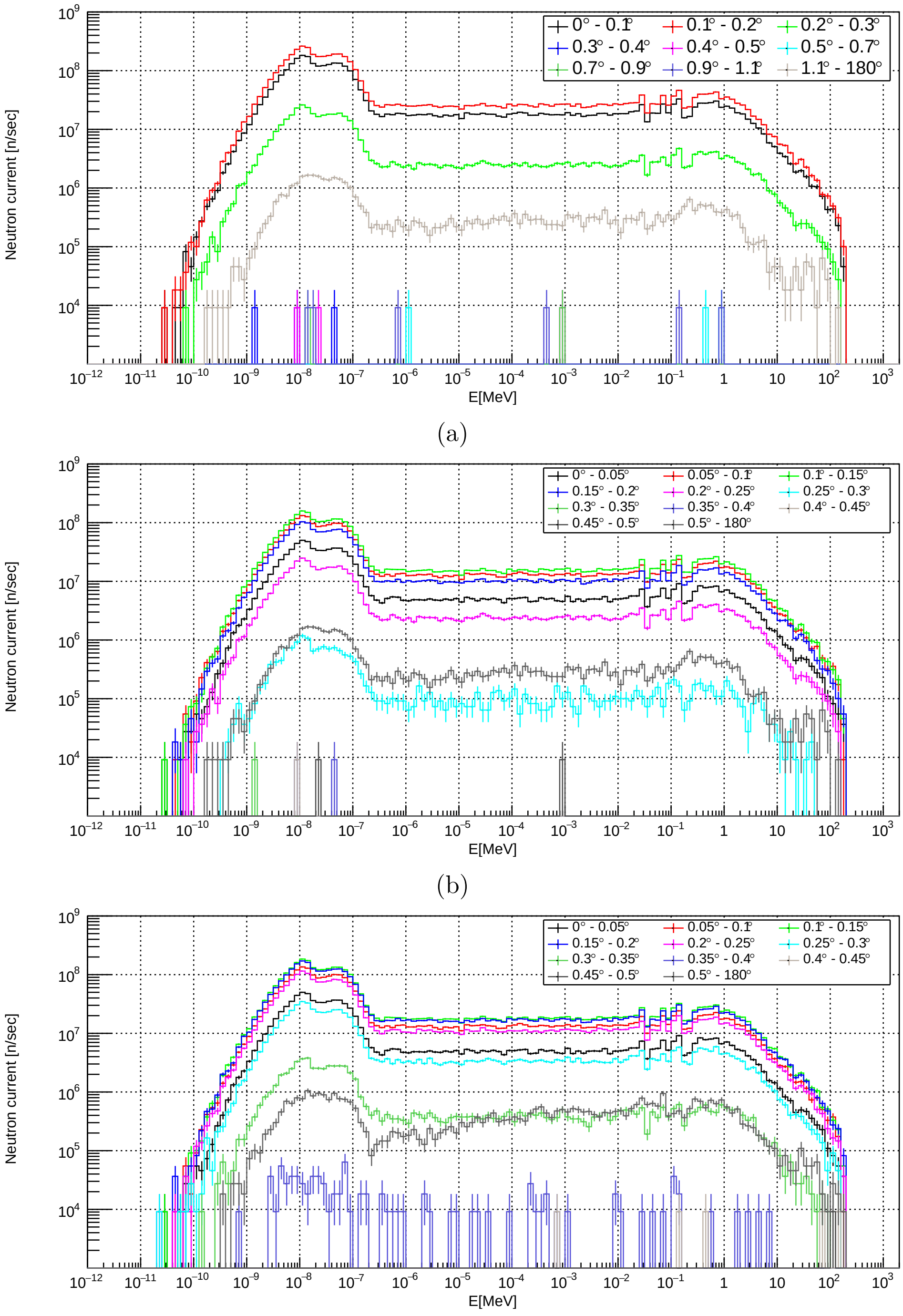

(a)

(b)

(c)

Figure 4.11: Neutron spectra for the candidates sources at the bunker wall exit with a coarse binning (a), at the bunker wall exit with a fine binning (b) and at the bunker wall entrance with a fine binning (c).

other two from 0.5° to 180° for the fine binning. These last bins cover a very broad region of space, hence they can collect a larger amounts of neutrons, and yet their heights is relatively small compared to the bins about the beam-line axis. Hence, it is clear that the neutron beam that finds its way in the bunker wall insert is highly collimated.

A slightly broader divergence is shown at the bunker wall entrance, in the last graph in figure 4.10(c), respect to that at the bunker wall exit in figure 4.10(b), where the same fine binning is used. This is a proof that also the bunker wall insert, similarly to the monolith feed-through, acts as a collimator for the neutron beam, although neutrons at the bunker wall entrance already have a very small divergence about the beam-line axis. In fact, the gain is just a factor of 0.1°, from 0.35° of figure 4.10(c) to 0.25° of figure 4.10(b).

Although the amounts of neutrons detected in the last bins of both the coarse and fine binnings are not negligible, they have to be compared with the height of the other few bins that cover the very first angles, before the grey area. It is indeed clear from that comparison that the last bins are relatively much less relevant, especially if the analogous comparison is made for the last bin of the primary source term respect to all the other bins in the same angular distribution (shown in figure 4.4). This proofs that the monolith feed-through acts as an effective collimator since the angular distribution of the primary source at 2 m from the moderator centre, has a much broader divergence than the observed at the bunker wall entrance. This collimation effect was also checked with a simulation in which all the angular bins of the primary source, except the first about the beam-line axis, were suppressed. The flux inside the bunker area resulted to be comparable to that produced when neutrons are emitted in all the angles of the primary source angular distribution.

Because of the observed small divergence of the beam and the very low contribution from the bins in the grey areas in the three graphs of figure 4.10, it was chosen to neglect them by setting to zero the probability to generate neutrons having those emission angles. In fact, the heights of those bins in the grey areas are such that about only a few neutrons out of one million would be generated with an emission angle in those angular ranges. The energy of those few neutrons should also be sampled according to the spectrum associated to the sampled angular bin. This results in the requirement of an higher number of primary particles to generate in a MCNP simulation in order to sufficiently sample the very small contributions of such small angular ranges in the grey areas. They should also survive the scattering against the bunker material inside its feed-through, which is inevitable at those angles due to the geometrical dimensions of the feed-though.

The resulting angular distributions that were used to set up three candidate sources are shown in figure 4.10, where all the other bins outside the grey areas were kept, included the last bins with a broad angular range.

Hence, figure 4.10 and figure 4.12 show the same graphs, with the difference being in the substitution of the bins in the grey areas in the latter with a single bin having a null probability to be sampled.

4.3.4 Benchmarks for selecting the secondary source term

The three candidate secondary sources were tested so to select the one that was used for studying the beam-line shielding. The benchmark is similar to that used in paragraph 4.2.1 for setting up the primary source term. It consists of comparing pairs of spectra calculated at specific positions. Such positions were selected along the beam-line axis, at different distances from the moderator centre: 25 m, 30 m, 35 m and 40 m. Two additional positions were considered inside the second chopper pit, at 20.7 m along the the beam-line axis, and at ±70 cm in the perpendicular direction on the horizontal plane. Such positions are shown in figure 4.13.

The resulting spectra from the benchmarks are shown in figure 4.14, where they are compared with the spectra produced by the primary source term (dashed lines) in the same positions.

Qualitatively, all the three candidates show a good agreement. Some procedure is needed in order to quantify and hence select the best source. For such purpose, an analogous quantity to that given in equation 4.5 was used. In that case the purpose was to tweak the normalization factor for the primary source term, by using the proton source as a reference. Now the primary source term is used as a reference for testing the secondary source candidates.

Consider to label the content of the each bin of the spectra from the primary source as s_i. The analogous bin for each of the secondary source candidates is labelled as c_i. Since 3 candidate sources were investigated, the latter label has to be replaced with c_i^{src}, where the index $src = \{1, 2, 3\}$ takes into account which candidate source is in examination. In contrast to what was done in paragraph 4.2.1 for the primary source, the benchmarks for the secondary sources were performed by comparing several spectra in different positions. Hence, a third index *pos* has to be considered so to address the positions in figure 4.13. The quantity ξ should thus be written as

$$\xi^{src,pos} = \sum_i (x^{src,pos} \cdot c_i^{src,pos} - s_i^{pos})^2. \tag{4.9}$$

where $x^{src,pos}$ is the analogous multiplicative factor for the secondary source candidates.

The quantities $\xi^{src,pos}$ were investigated for the three sources, in each of the six pairs of spectra in figure 4.14. They are shown in figure 4.15 as functions of the quantities $x^{src,pos}$. Also in this case, due to the form of equation 4.9, each of the curves $\xi^{src,pos}(x^{src,pos})$ is a parabola.

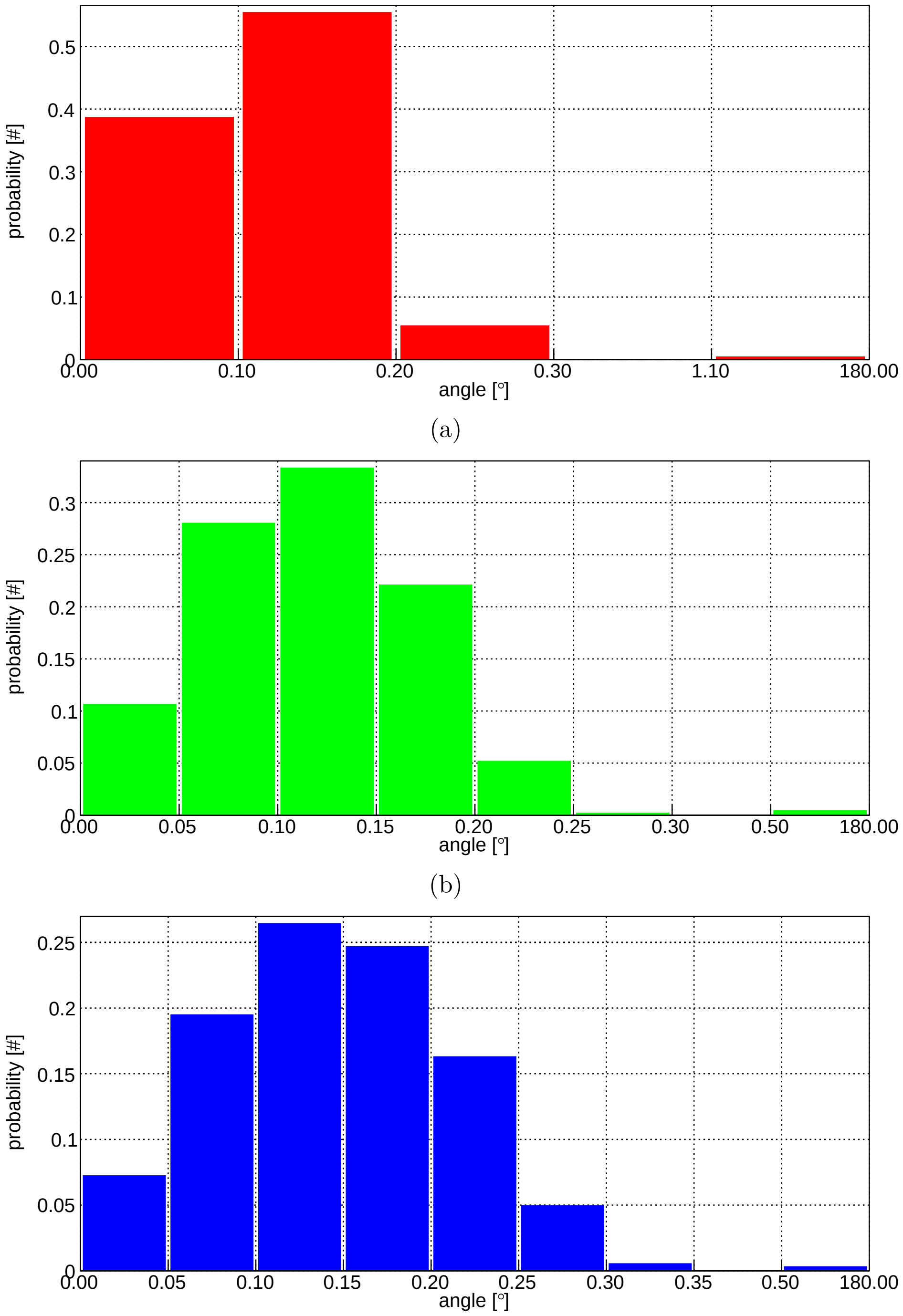

(a)

(b)

(c)

Figure 4.12: The refined angular distributions for the candidates source terms at the bunker wall exit (15 m) with a coarse binning (a), at the bunker wall exit (15 m) with a fine binning (b) and at the bunker wall entrance (11.5 m) with a fine binning (c).

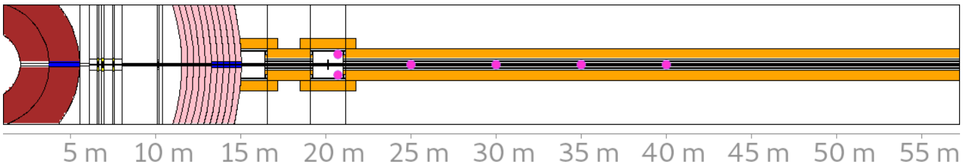

Figure 4.13: The six positions used for benchmarking the candidate secondary source terms with the primary source term.

4.3.5 Selection of the secondary source term

The values of $x^{src,pos}$ that minimize the $\xi^{src,pos}$ have now a different role respect to what was done in paragraph 4.2.1. In fact, in that case x was investigated as the multiplicative factor that has to be used in order to obtain the best match between the primary source term and the proton source. Now, the $x^{src,pos}$ are used to choose the best secondary source among the three candidates. If all the three sources were perfectly determined, with the best angular distributions, each $x^{src,pos}$ should be independent on the position *pos* at which the spectra were calculated. Furthermore, $x^{src,pos} \simeq 1$ for all the sources *src*.

The graphs in figure 4.16 shows the minima $x^{src,pos}$ as a function of the positions in which the spectra of figure 4.11 were calculated. It is clear from them that the best secondary source is the one at the bunker wall entrance. In fact, the multiplicative factors $x^{src,pos}$ in the blue lines are the closest ones to the unity. Furthermore, the source at the bunker wall entrance is the one for which all those factors are lower than 1. This means that the neutron current produced by that source overestimates that of the primary source in all the considered positions. Because of that, it was chosen as the secondary source term for calculating the shielding studies for VESPA.

The values of the minima $x^{src,pos}$ are different in the positions along the beam-line respect to those in the second chopper pit. However, the normalization factor was not rescaled in order to account for that. Its value, which was used for the studies presented in this thesis, is

$$\sim 9.462 \cdot 10^9 \,\text{sp/sec}. \tag{4.10}$$

By using such value, the neutron current is overestimated. Hence all the results produced by the secondary source term are overestimated, till a maximum factor of ~ 2 in the proximity of the bunker wall exit. Small overestimations do not represent an issue for shielding studies, since they can lead to build structures that ensure even lower dose rates than the calculated.

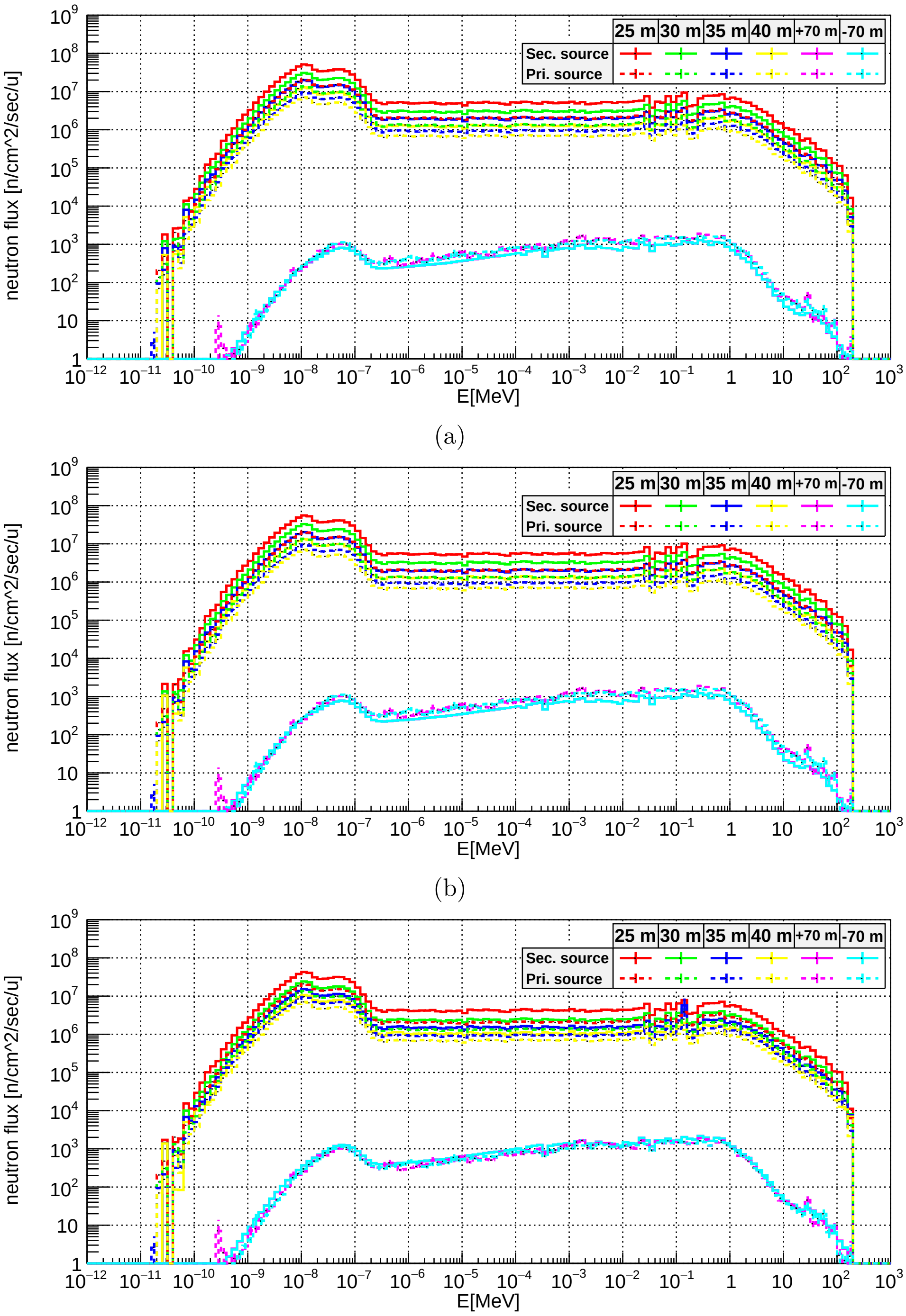

(a)

(b)

(c)

Figure 4.14: Benchmark spectra for the candidate secondary sources at the bunker wall exit with a coarse binning (a), at the bunker wall exit with a fine binning (b) and at the bunker wall entrance with a fine binning (c).

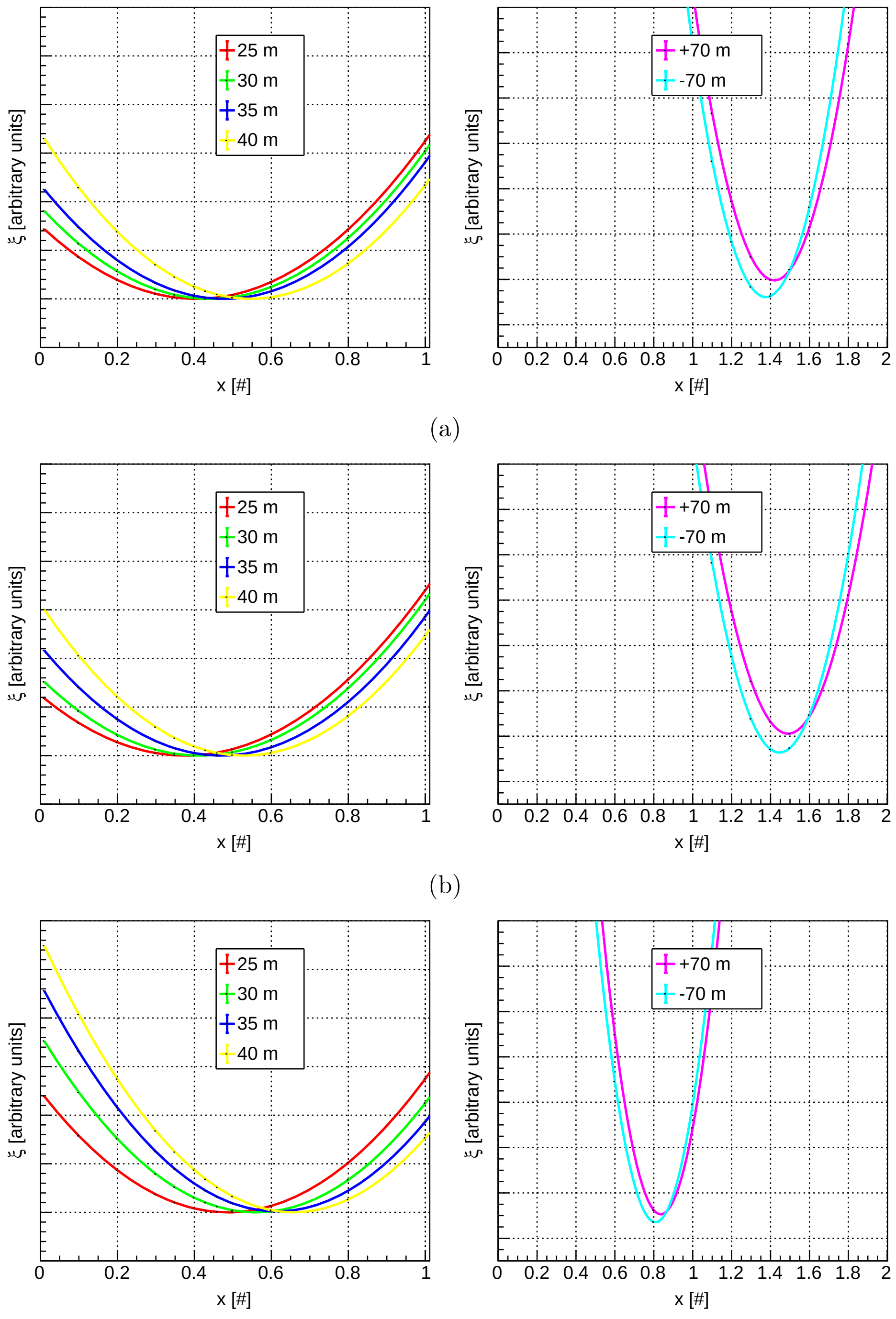

(a)

(b)

(c)

Figure 4.15: Graphs of the quantities $\xi^{src,pos}$ as a function of $x^{src,pos}$ for the source at the bunker wall exit with a coarse binning (a), at the bunker wall exit with a fine binning (b) and at the bunker wall entrance with a fine binning (c).

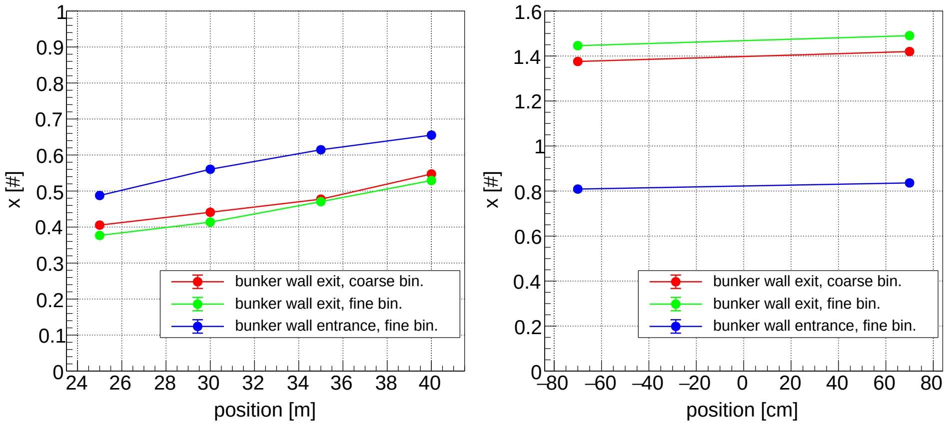

(a) (b)

Figure 4.16: Graphs of the minima $x^{src,pos}$ as functions of the positions along the beamline (a) and in the second chopper pit (b).

4.3.6 Effects of a gamma source term

The choice to consider only neutrons as particle source for the studies presented in this thesis, as well as for similar studies within the Common Shielding project, comes from the studies about the primary source term [51] and those on the design of the bunker wall [28]. The latter, in particular, shows that neutrons are responsible for the largest part of the radiation doses outside the bunker, whereas gammas contribute only for about 3 % [28]. These results give clear hints in deciding whether to consider also gamma in the source definition for the studies in this thesis, however it must be note that they were produced with the purpose to design the bunker wall, hence no beam-ports are considered in the model. In order to determine if a gamma source needed, along with the neutron source, for the shielding design of VESPA, a set of simulations was performed. The CombLayer model of ESS [45] was used to calculate the gamma spectrum at the beam-port entrance of VESPA instrument at 2 m from the moderator centre. It is shown in fig 4.17.

A further simulation was performed with the purpose to calculate the integral gamma current at the bunker wall entrance, at 11.5 m from the moderator centre. Such quantity was calculated using a point-detector tally at that position, since other tallies require elaborated variance reduction techniques in order to produce meaningful results. The outcome is

$$4.077 \cdot 10^7 \text{ gamma/sec.} \tag{4.11}$$

This result was used as the normalizing factor for setting up a simple gamma source at the bunker wall entrance. Such source was set so to emit only monochromatic gammas of 10 MeV, the maximum energy of gammas

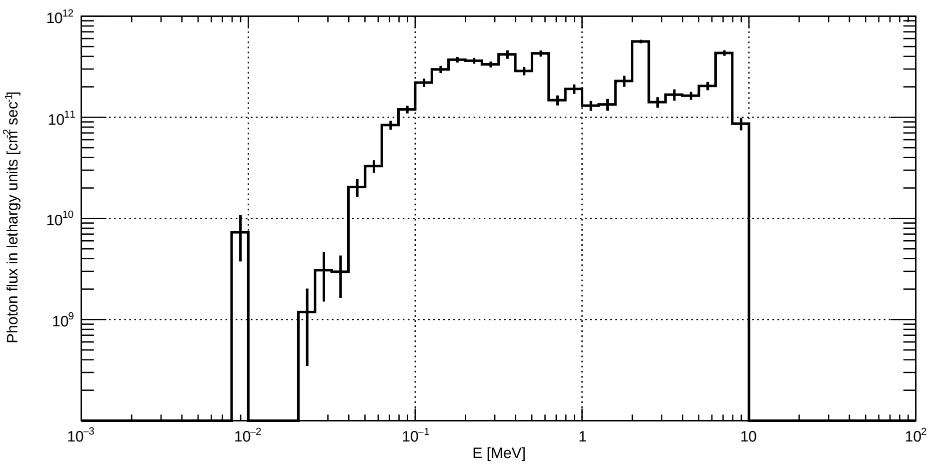

Figure 4.17: Gamma flux spectrum taken at 2 m from the moderator centre, on the surface area of VESPA primary source.

produced in the target, as shown from the spectrum in figure 4.17. The source surface is a rectangle whose dimensions are the same of the feedthrough of the bunker wall entrance. It emits gammas within an angle of about 0.3 °. Such value is the maximum geometrical divergence that a gamma particle at 2 m from the moderator centre can have so to travel in a straight direction, without interacting with material, from that position to the bunker wall entrance at 11.5 m.

The gamma source was used in a MCNP model of VESPA having a shielding design that will be introduced later in this thesis, in chapter 5. The purpose was to produce the gamma dose rate map in figure 4.18, that shows the negligible impact on the dose rates of a source that reproduces the gamma emission from the target.

This gamma source largely overestimates the results, due to the thoughtful choice to design it so that it emits only gammas of 10 MeV in energy, with the same current of equation 4.11 calculated at 11.5 m from the moderator centre.

A gamma source was neglected when performing the studies provided in this thesis, due to their negligible impact on the dose rate, as shown from the map in figure 4.18. However, the gamma prompt radiation induced by neutron reactions was not neglected, and relevant gamma dose rate maps are provided later in this thesis.

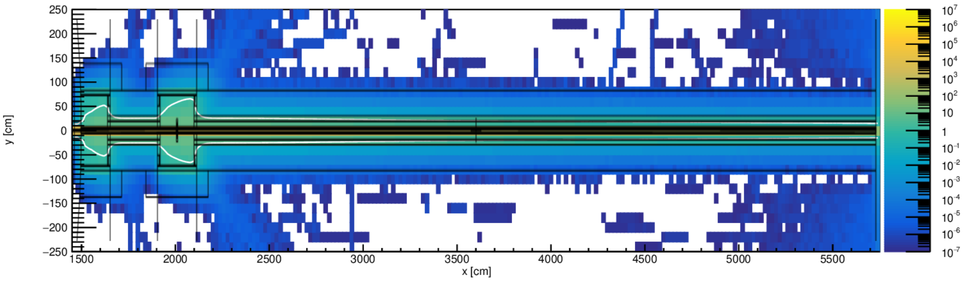

Figure 4.18: Top-view of the gamma dose rate map due to monochromatic gamma source of 10 MeV at the entrance of the bunker wall. The image shows one of the shielding geometry used in the Common Shielding project, later introduced in this thesis.

Chapter 5

Beam-line Shielding

This chapter is dedicated to provide the results of the simulations performed for designing the shielding of VESPA beam-line. The calculations aimed to design the shielding in compliance with the requirement of not exceeding $1.5\,\mu$Sv/h [16, 17] for both neutron and photon dose rates.

5.1 Common Shielding Project

VESPA is one of the 13 instruments that joined the Common Shielding Project at ESS [55]. The project aims to centralize the efforts of the instrument teams in performing the scientific investigations for designing the beam-line shielding. It provides a common work-team constituted by representatives of the instrument teams in charge of performing neutronic calculations, engineers and ESS scientists and coordinators.

The scope of the Common Shielding Project is to standardize the beam-line shielding structures based on the neutronic input from the work-team. The outcome is a common design that is suitable for the instruments involved in the project. It consists of modular blocks of different sizes, made of layers of different material and thickness.

The simulations within the Common Shielding Project, including those presented in this thesis, started by considering the effect of fast neutrons, which are of particular concern for shielding purposes. The effects of slow neutrons were investigated in a more accurate way as a next step. Slow neutrons do not drive the shielding requirements due to their smaller penetration length in matter. However, they have a higher cross section for radiative capture, that can produce high energetic gammas. The dose due to gamma particles was calculated using the standard MCNP code to give a preliminary estimation of their dose rate maps. More accurate calculations are given for the gamma dose rate map, after the design of the shielding has been defined to meet the dose level requirements for fast neutrons.

5.2 Geometry

The Common Shielding Project proposes two main geometries for the beam-line shielding, one for the instruments in the short sector, the other for the long sector. The one suitable for VESPA, which is under construction in the East short sector, is shown in figure 5.1. It consists of two main types of blocks. The basal blocks are 1 m tall and made of ordinary concrete. Their shape resembles a reverse U letter in order to reduce the weight and to leave space for cables.

The shielding blocks above the basal blocks are made of three consecutive layers of different material attached together. Their thickness and material are given in the following list, starting from the innermost layer.

1. borated concrete, 2 cm,
2. steel, 10 cm,
3. concrete, variable thickness.

Concrete, steel and borated compounds are common shielding materials for spallation facilities [56, 57, 58] and for ESS in particular [59].

Details on the size of the blocks for the guide shielding are given in figure 5.2. It shows the current design in which a layer of steel is added at the bottom of the guide.

5.2.1 Preliminary model

The first set of simulations aimed to determine the shielding design for VESPA using the preliminary concept in figure 5.1. Calculations were performed using an increasing thickness for the concrete layer, by steps of 10 cm, starting from 60 cm. The dose rate maps due to photons and neutrons are given in figure 5.3 to figure 5.10, were the white lines are isodose line at $1.5\,\mu$Sv/h. The purpose is to determine the adequate shielding for the concrete layer, so that the dose rate on their external surface is lower than ESS limit set at $1.5\,\mu$Sv/h

The results show that the isodose lines for the gamma dose rates are of less concern respect to the neutron dose rates. In fact, photon isodose lines are closer to the beam-line axis in each dose map. This is already quite noticeable by comparing figure 5.3 and figure 5.4. They show that the 60 cm thick concrete layer provides enough neutron shielding only from 40 m − 45 m to the instrument cave. On the other hand, that concrete thickness is sufficient for shielding the gamma radiation already from ~ 35 m. A slightly thicker concrete layer is already sufficient to shield the gammas for the entire length of the instrument in the hall. It can be seen in figure 5.6, where only in the first section with the chopper pits the gamma isodose lines escape from the shielding boundaries.

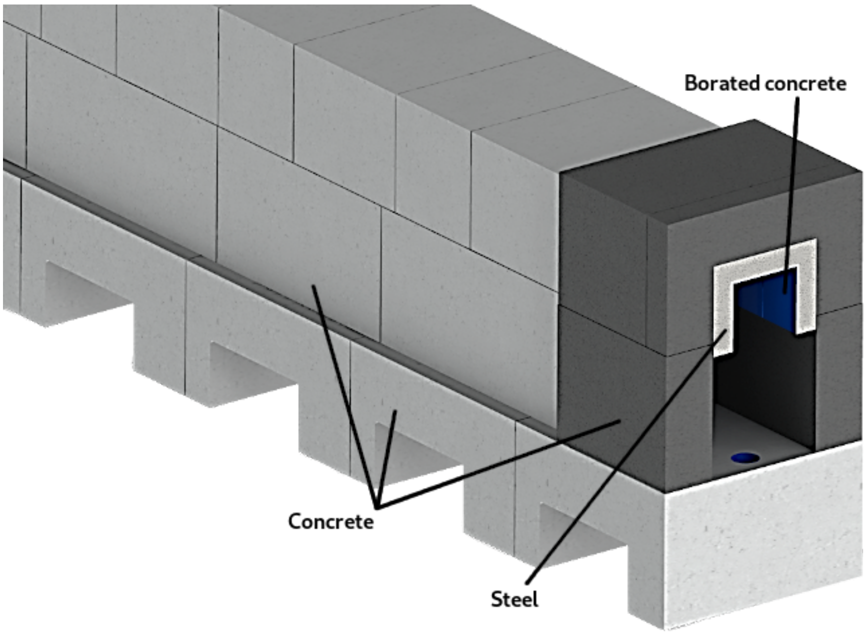

(a)

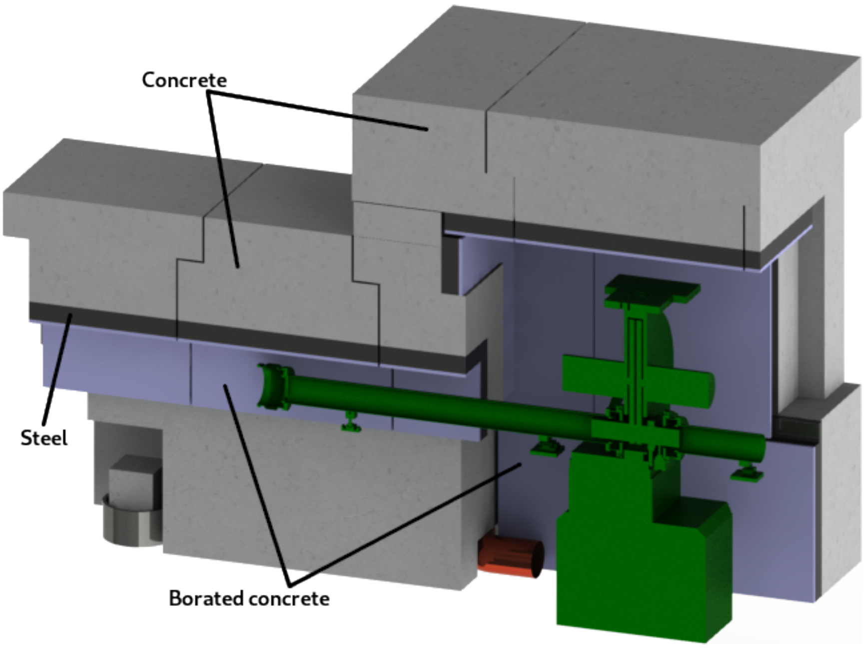

(b)

Figure 5.1: Engineering drawings of the preliminary shielding design of the guide section (a) and the chopper pit (b) in the short sector halls [60, 61].

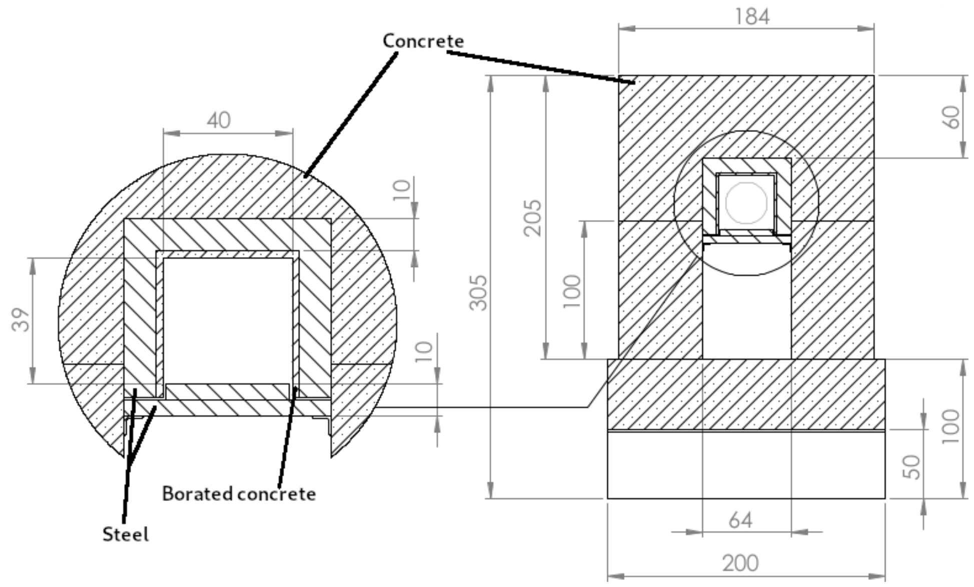

Figure 5.2: Engineering drawing of the guide shielding [62] showing the relevant geometrical parameters, with a detailed view of the region around the guide on the left. This picture is a vertical section of what is shown in figure 5.1(a).

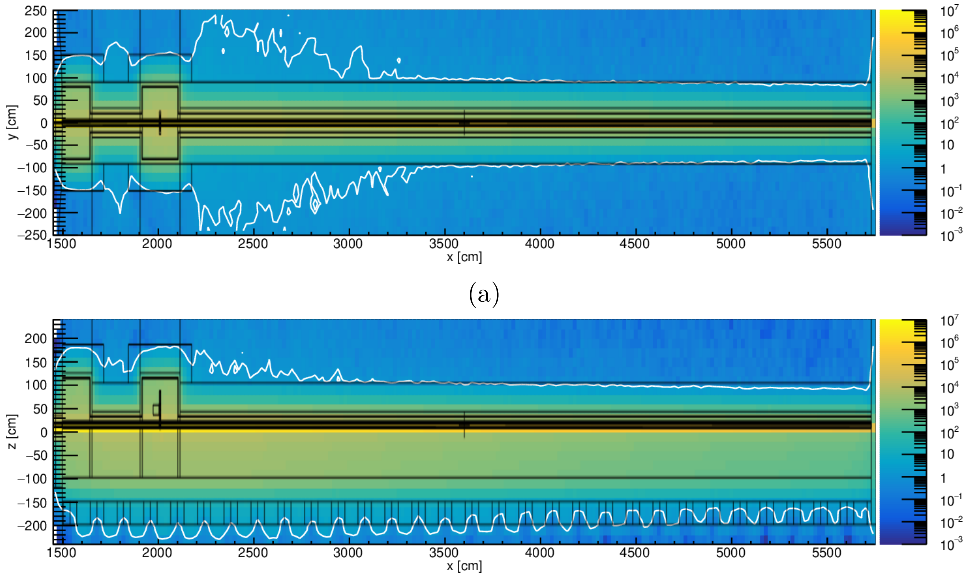

(a)

(b)

Figure 5.3: Preliminary model top-view (a) and side-view (b) of the neutron dose rate map with a 60 cm thick concrete layer.

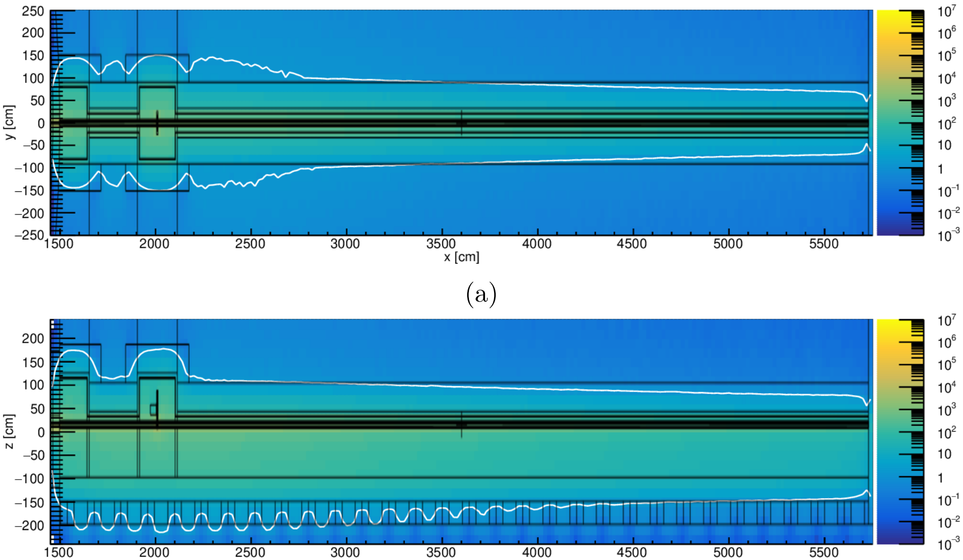

(a)

(b)

Figure 5.4: Preliminary model top-view (a) and side-view (b) of the photon dose rate map with a 60 cm thick concrete layer.

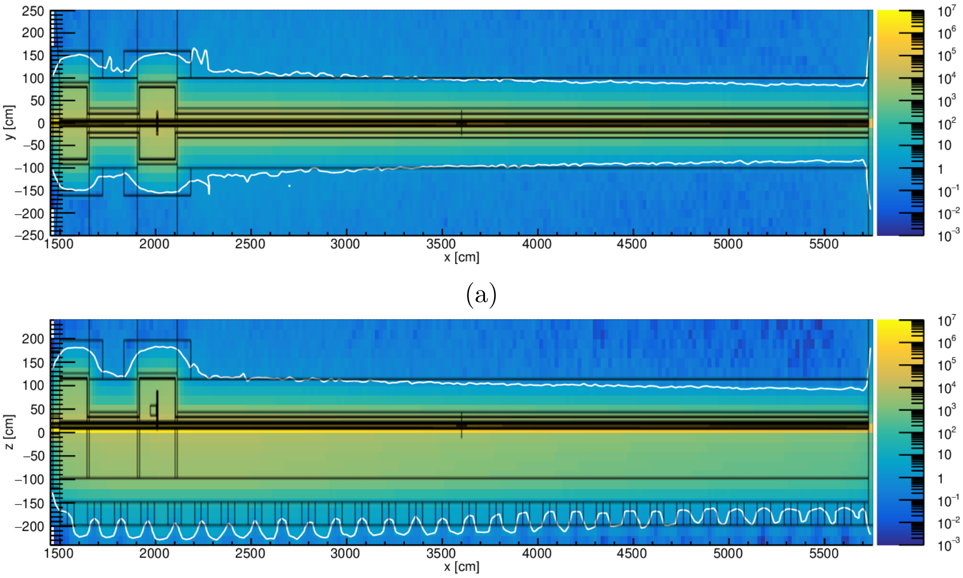

(a)

(b)

Figure 5.5: Preliminary model top-view (a) and side-view (b) of the neutron dose rate map with a 70 cm thick concrete layer.

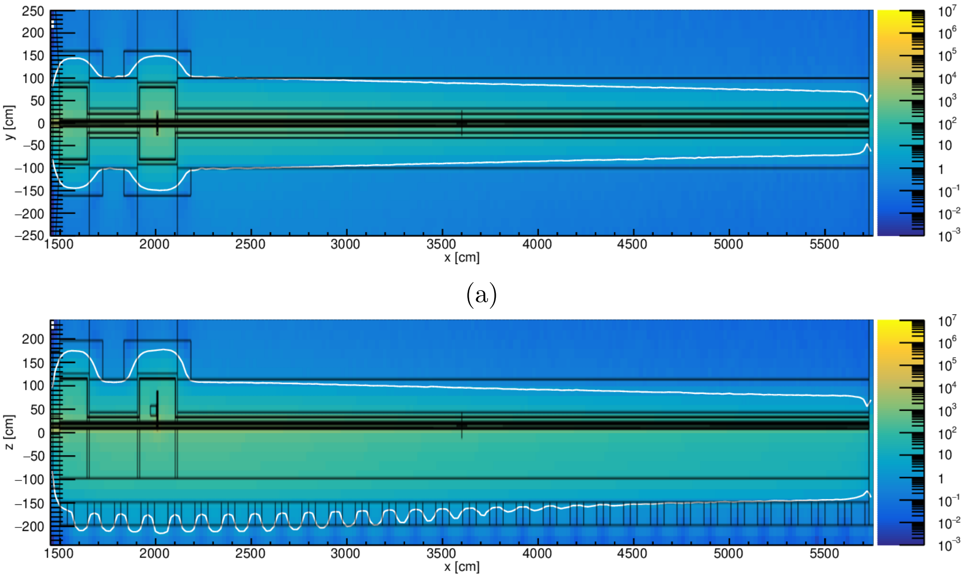

(a)

(b)

Figure 5.6: Preliminary model top-view (a) and side-view (b) of the photon dose rate map with a 70 cm thick concrete layer.

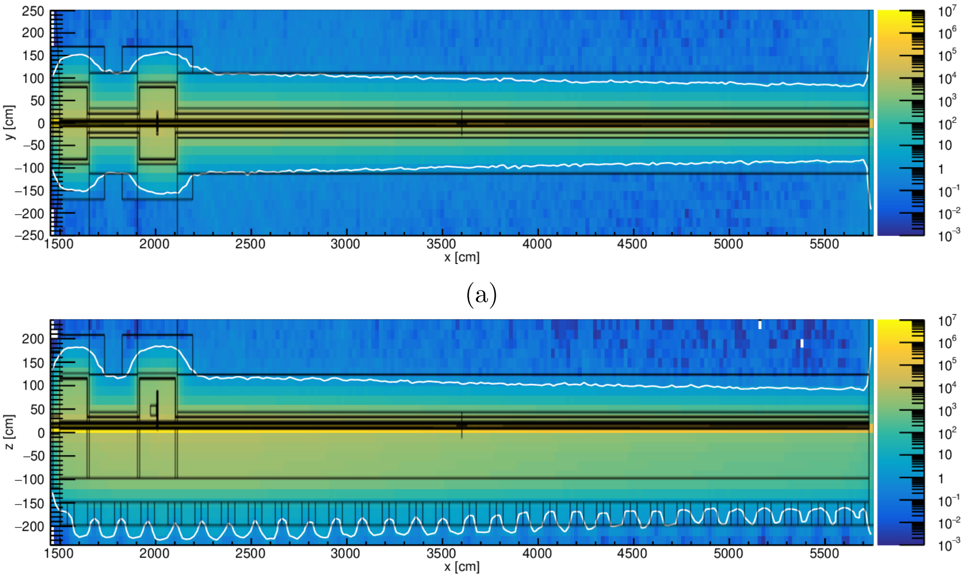

(a)

(b)

Figure 5.7: Preliminary model top-view (a) and side-view (b) of the neutron dose rate map with a 80 cm thick concrete layer.

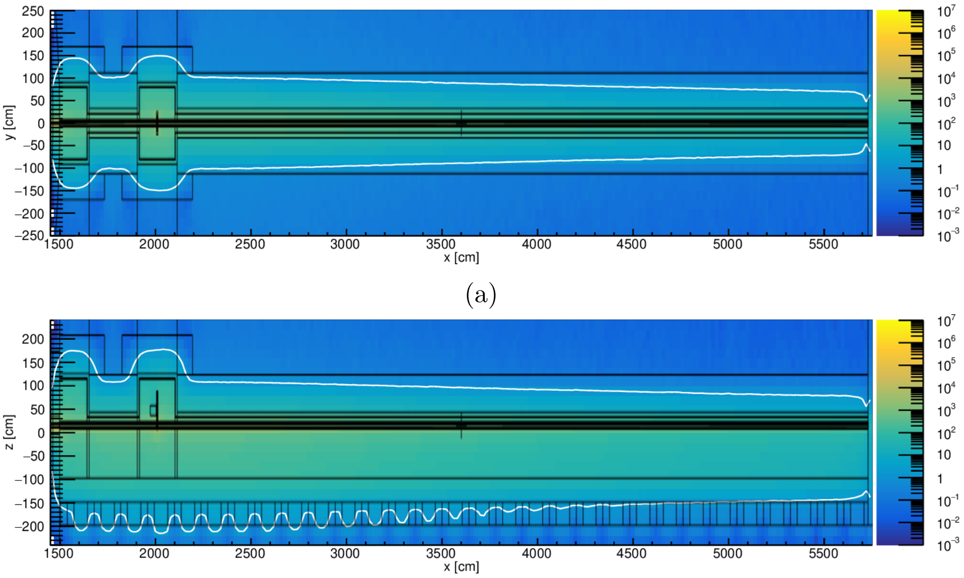

(a)

(b)

Figure 5.8: Preliminary model top-view (a) and side-view (b) of the photon dose rate map with a 80 cm thick concrete layer.

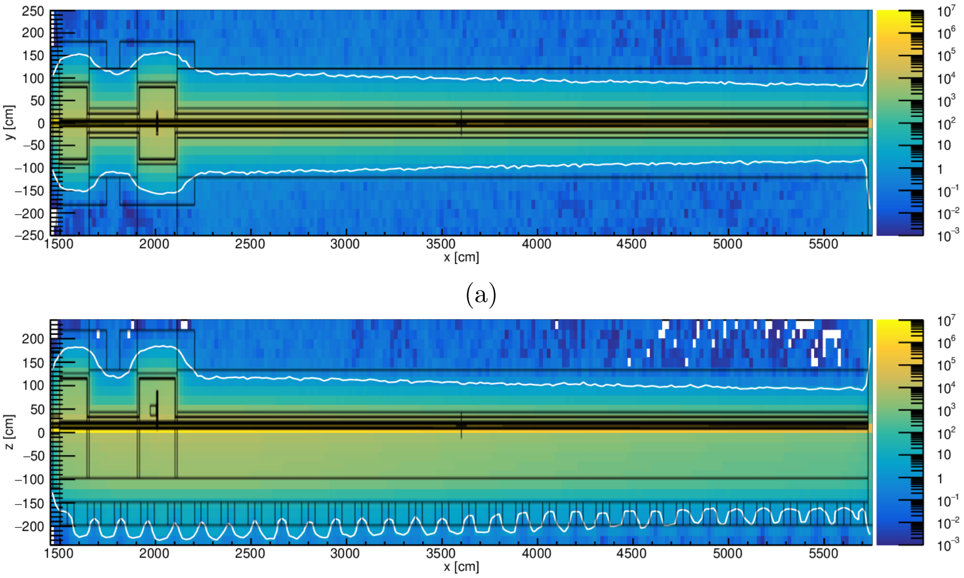

(a)

(b)

Figure 5.9: Preliminary model top-view (a) and side-view (b) of the neutron dose rate map with a 90 cm thick concrete layer.

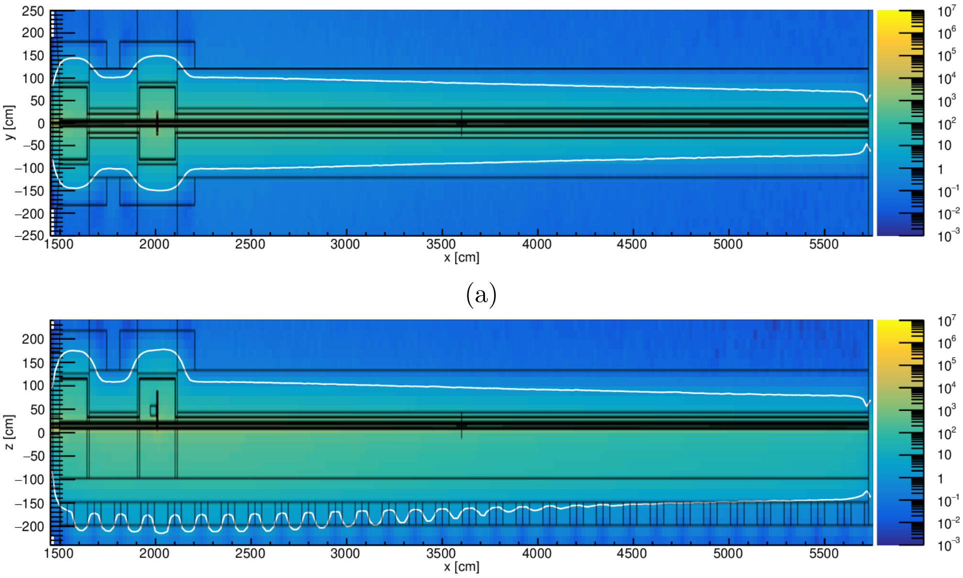

(a)

(b)

Figure 5.10: Preliminary model top-view (a) and side-view (b) of the photon dose rate map with a 90 cm thick concrete layer.

The isodose lines in all the pictures open up at the very end of each graph. This is due to the fact that the geometrical model ends in a void cell. In fact, the instrument cave is not modelled in the geometry.

5.2.2 Common shielding model

All the results for the preliminary model show a substantial leakage toward the floor. In order to reduce such effect, a layer of steel was added below the guide, as shown in figure 5.2. Additional changes consist in the vertical distance between the guide and the upper half of the shielding block, that was smaller by 3 cm in the previous model. Such difference should not be of any concern, yet the calculations were performed again using the correct model.

Results of the simulations are shown from figure 5.12a to figure 5.19a.

The dose rate maps are comparable with those of the preliminary design, as expected. In fact, the differences between the two model were not sufficient to significantly alter the results.

The major difference is in the dose rates below the guide. By comparing the neutron dose rate in figure 5.3b(b) with that in figure 5.12b(b), it is clear that the latter show a much smaller leakage toward the floor. In particular, such difference is significant at high distances from the bunker wall, like at about $\sim 40\,\mathrm{m}$. The same is not true for the neutron dose rate next to the bunker wall. This is due to the fact that the additional layer of steel below

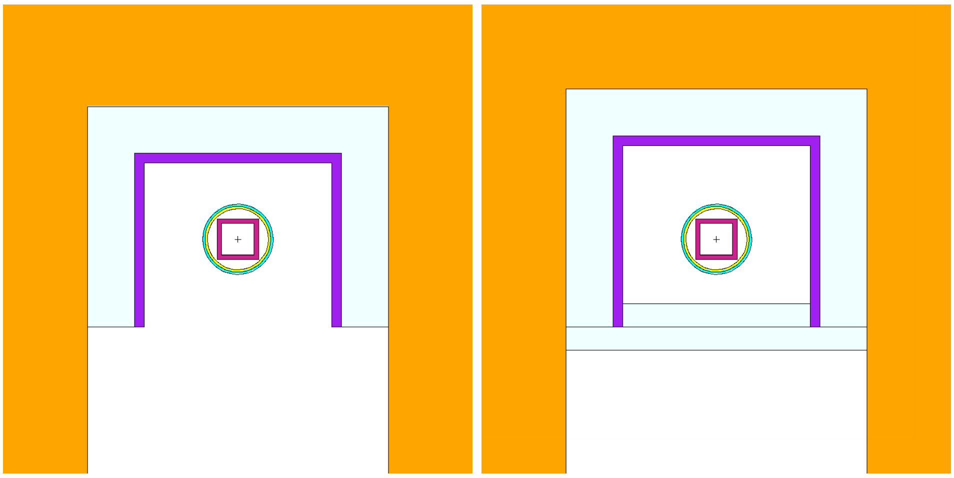

(a) (b)

Figure 5.11: Front-view of the preliminary Common Shielding model (a) and the definitive Common Shielding model (b) in MCNP, at 35 m from the bunker wall.

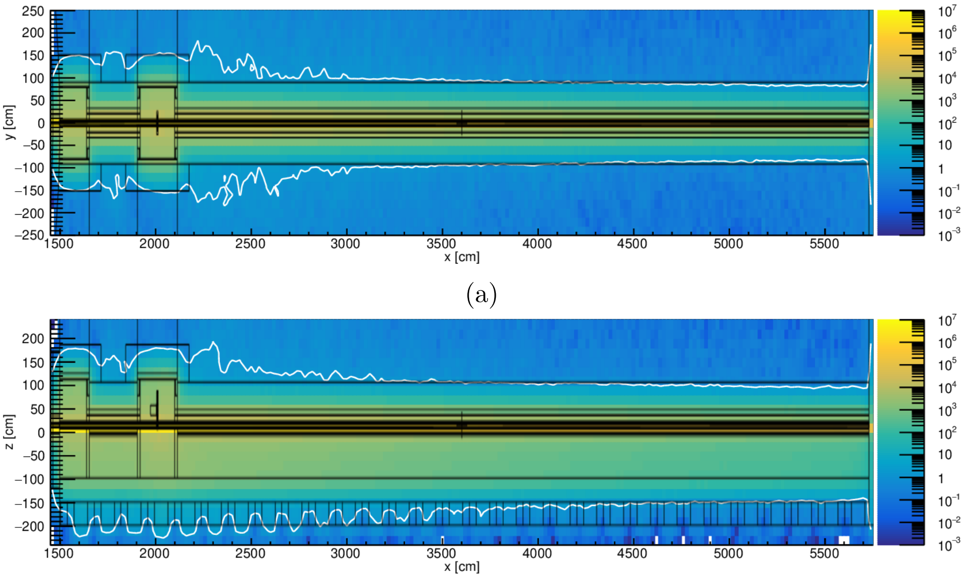

(a)

(b)

Figure 5.12: Common Shielding model top-view (a) and side-view (b) of the neutron dose rate map with a 60 cm thick concrete layer.

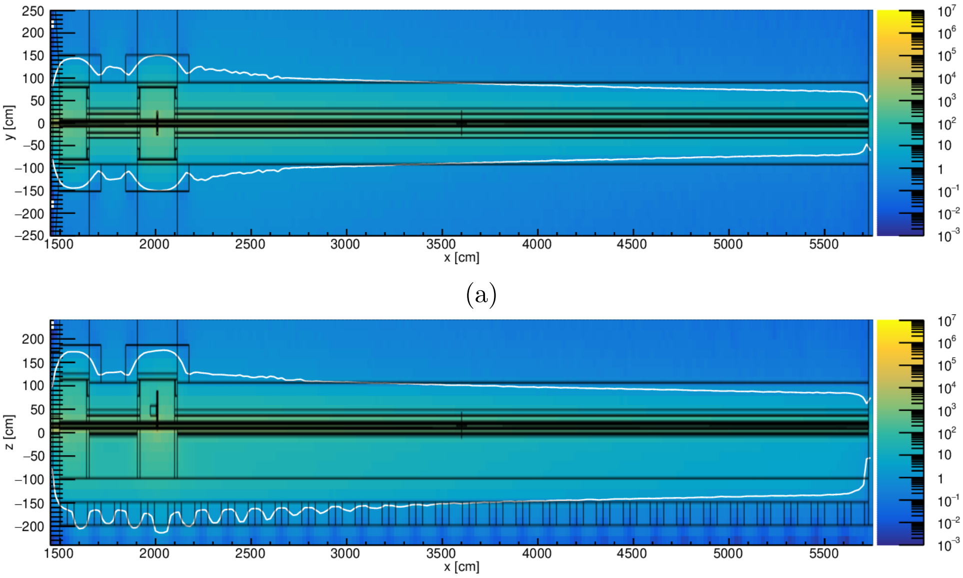

(a)

(b)

Figure 5.13: Common Shielding model top-view (a) and side-view (b) of the photon dose rate map with a 60 cm thick concrete layer.

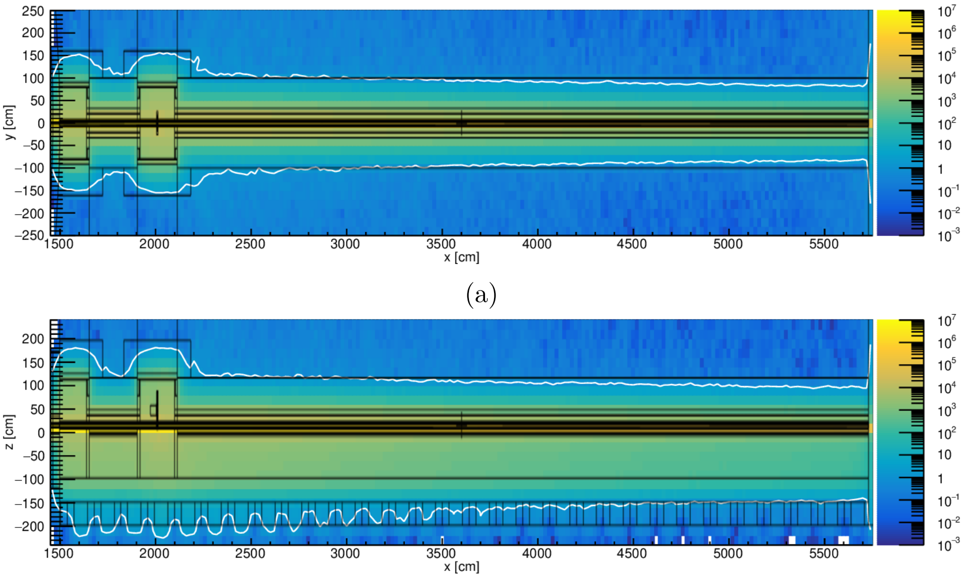

(a)

(b)

Figure 5.14: Common Shielding model top-view (a) and side-view (b) of the neutron dose rate map with a 70 cm thick concrete layer.

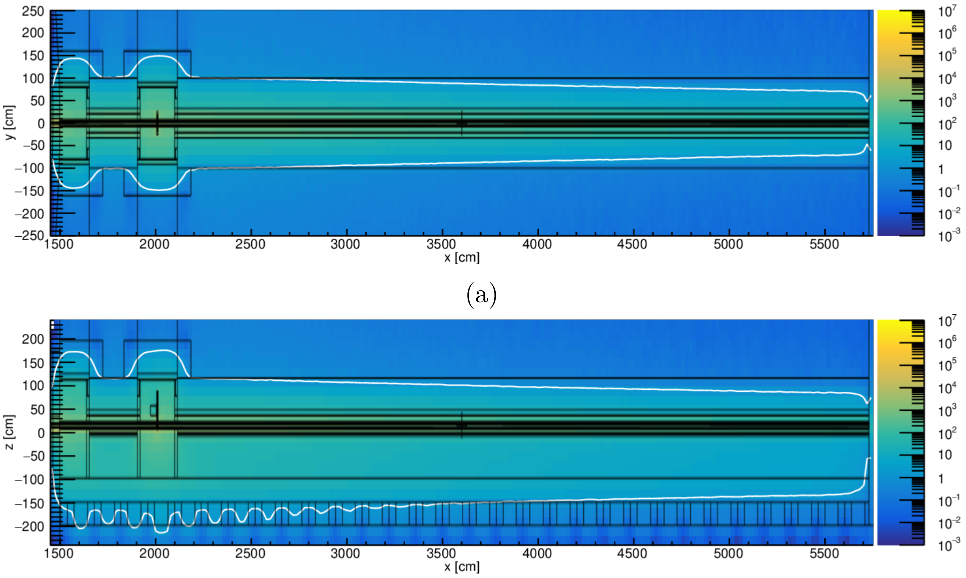

(a)

(b)

Figure 5.15: Common Shielding model top-view (a) and side-view (b) of the photon dose rate map with a 70 cm thick concrete layer.

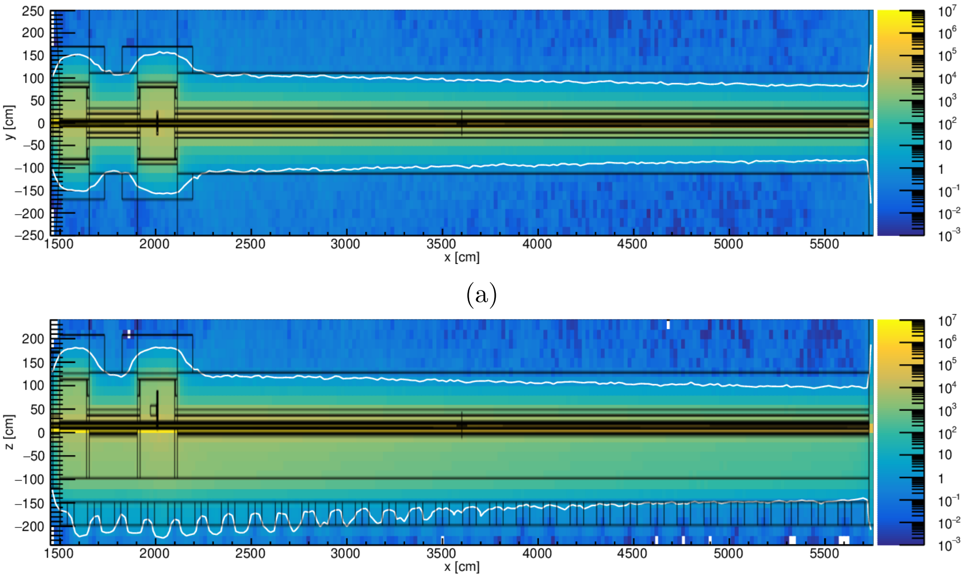

(a)

(b)

Figure 5.16: Common Shielding model top-view (a) and side-view (b) of the neutron dose rate map with a 80 cm thick concrete layer.

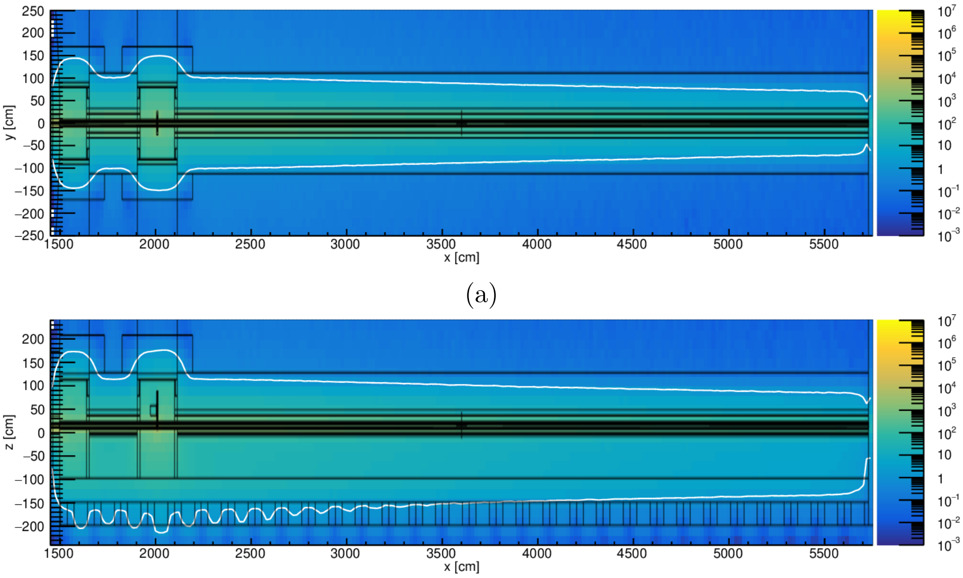

(a)

(b)

Figure 5.17: Common Shielding model top-view (a) and side-view (b) of the photon dose rate map with a 80 cm thick concrete layer.

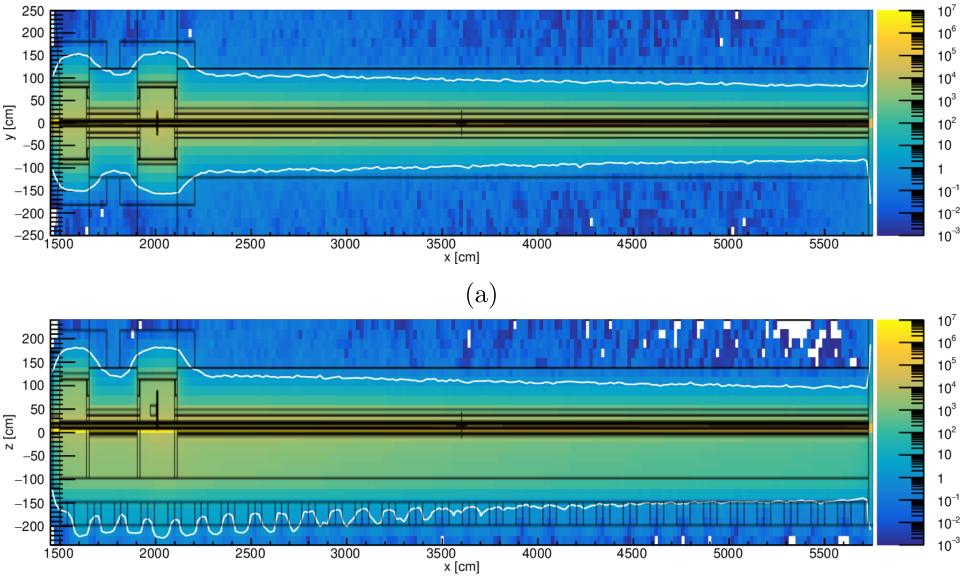

(a)

(b)

Figure 5.18: Common Shielding model top-view (a) and side-view (b) of the neutron dose rate map with a 90 cm thick concrete layer.

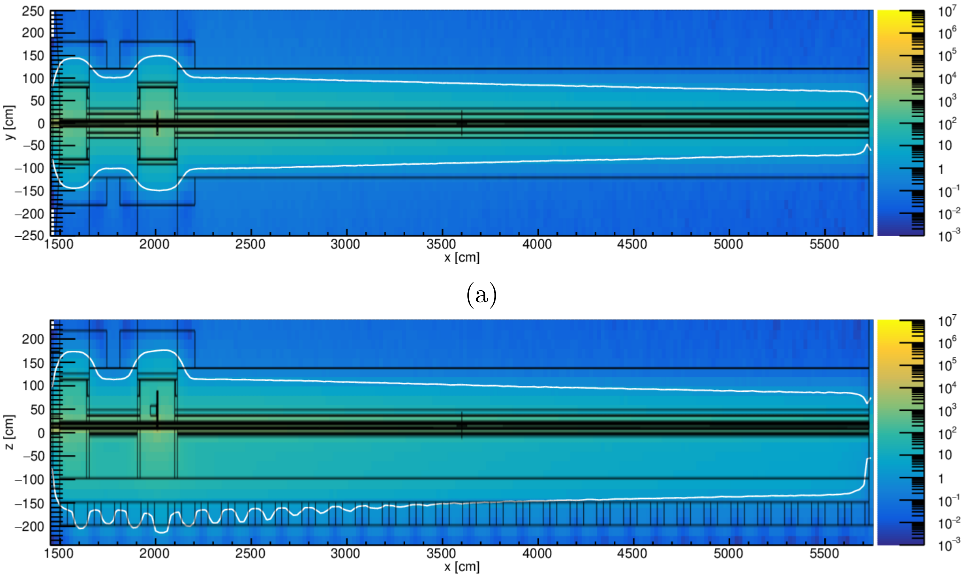

(a)

(b)

Figure 5.19: Common Shielding model top-view (a) and side-view (b) of the photon dose rate map with a 90 cm thick concrete layer.

the guide is not added in the chopper pits blocks. However, this is not a concern, because the void in the basal blocks are meant to host cables. Also, the isodose lines at 1.5 μSv/h in figure 5.20 show that the missing steel layer in the chopper pits do not constitute an issue for the shielding, because they do not reach the external boundary of the shielding structure.

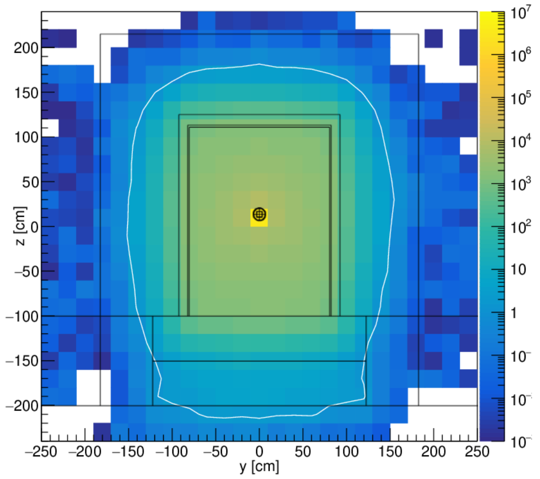

Figure 5.20: Common Shielding model front-view of the neutron dose rate taken at 1580 cm.

5.2.3 Common shielding model without borated concrete

The purpose of the borated concrete layer is to reduce the activation and the neutron absorption in the steel layer. Boron is characterized by a high cross section for neutron absorption. In particular, the cross section for the reaction $^{10}B(n, \alpha)^{7}Li$ is of $\sim 4000\,\mathrm{b}$ [1, 63], which makes it an effective neutron absorber for slow neutrons. In fact, it also finds application in nuclear reactor plants [64].

Slow neutrons are not of a concern respect to fast neutrons of energy $\gtrsim 1\,\mathrm{MeV}$. On the other hand, they have a much higher chance to induce nuclear reactions due to the general inverse proportionality $1/v$ of the neutron cross sections. When irradiated by slow neutrons, some metal-based alloys can emit high penetrating gammas of energy $\gtrsim 7\,\mathrm{MeV}$ [65]. This can be a concern for shielding. Thus, the need for the borated concrete layer was investigated.

A set of simulations was performed in order to determine if such layer is mandatory for the shielding design of VESPA. Results are shown from figure 5.21a to figure 5.28b.

Both the neutron and photon dose rate maps are similar to those calculated in the previous paragraph for the Common Shielding model. This can be due to the fact that the guide substrate is a 1 cm thick layer of borofloat. The percentage of boron in such material could be sufficient to capture slow neutrons. The amount of slow neutrons that reach the steel layer could thus be already minimal, even without the additional borated concrete layer in the shielding structure.

5.2.4 sFOC in closed configuration

The purpose of the Common Shielding project and, hence of this thesis, is to determine the design of the shielding of the instruments outside the bunker so that it is capable of containing the hazardous radiation in the worst case scenario. In order to match this with the need for an advantageous comparison of the studies from all the instruments that joined the project, the considered scenario is the one in which all the instrument choppers are in a full-open configuration. The scenario in which one particular chopper is stuck in a closed or half-closed configuration is considered an accident scenario and, as that, is to be studied as part of the risk assessment of the particular instrument [48]. Such studies are beyond the scope of this thesis, since they are not part of the Common Shielding project. They are at their initial stages at the time of reviewing this thesis (June 2020).

In VESPA instrument there is only one chopper outside the bunker, in the area of interest for the Common Shielding project. The scenario in which that chopper, the sFOC chopper at $\sim 20\,\mathrm{m}$ from the moderator centre, gets the full beam coming from the moderator is not part of the ordinary operation of the instrument [36]. In fact, during normal operations, the high

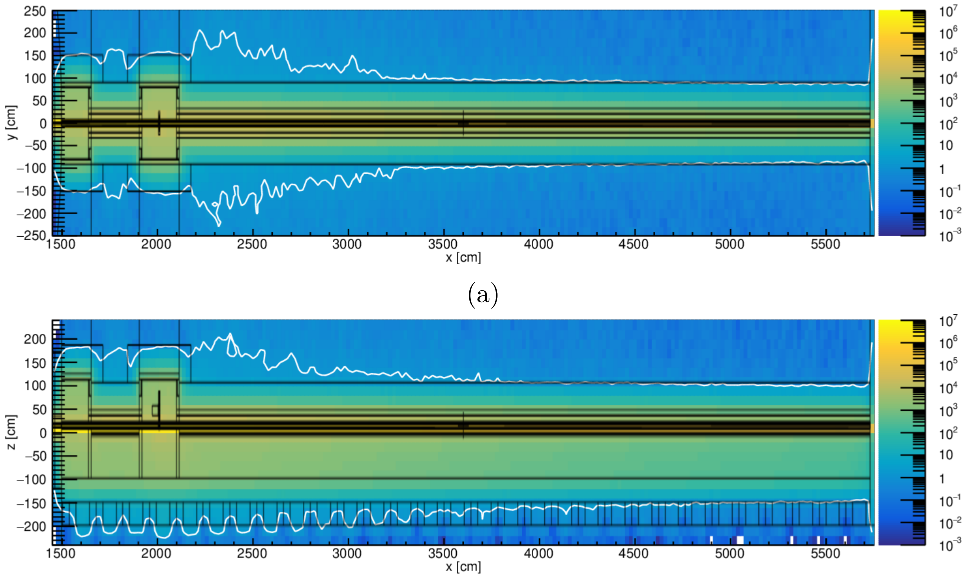

(a)

(b)

Figure 5.21: Common Shielding model (without the borated layer) top-view (a) and side-view (b) of the neutron dose rate map with a 60 cm thick concrete layer.

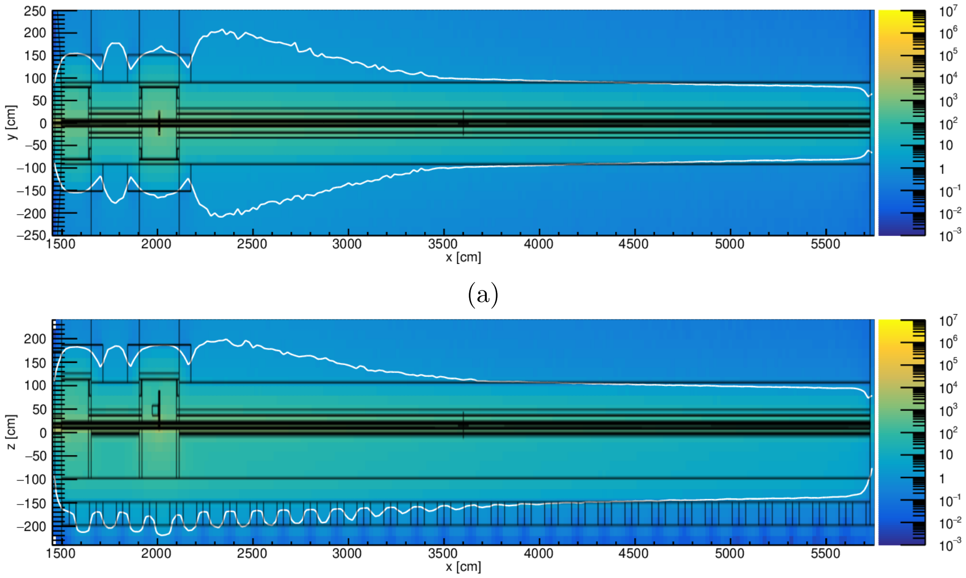

(a)

(b)

Figure 5.22: Common Shielding model (without the borated layer) top-view (a) and side-view (b) of the photon dose rate map with a 60 cm thick concrete layer.

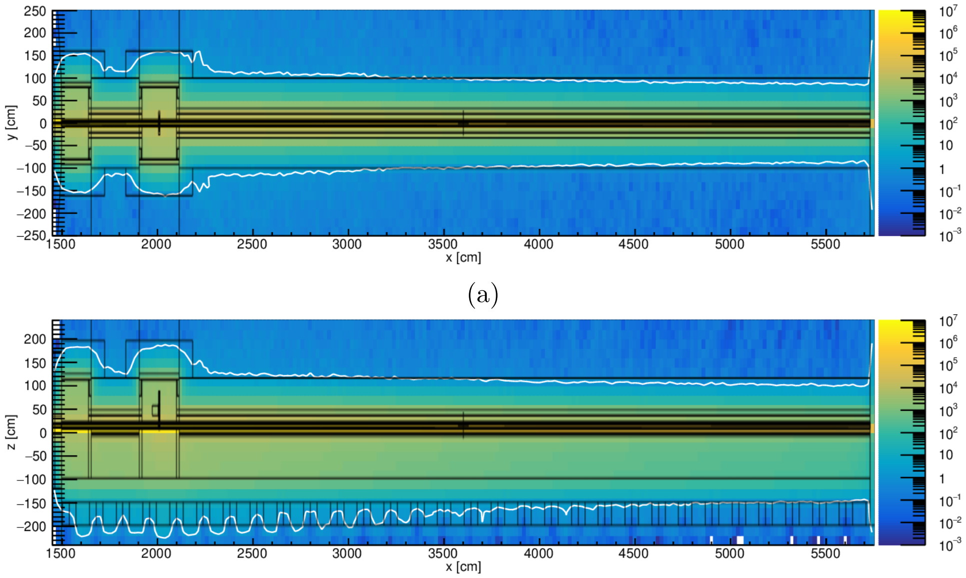

(a)

(b)

Figure 5.23: Common Shielding model (without the borated layer) top-view (a) and side-view (b) of the neutron dose rate map with a 70 cm thick concrete layer.

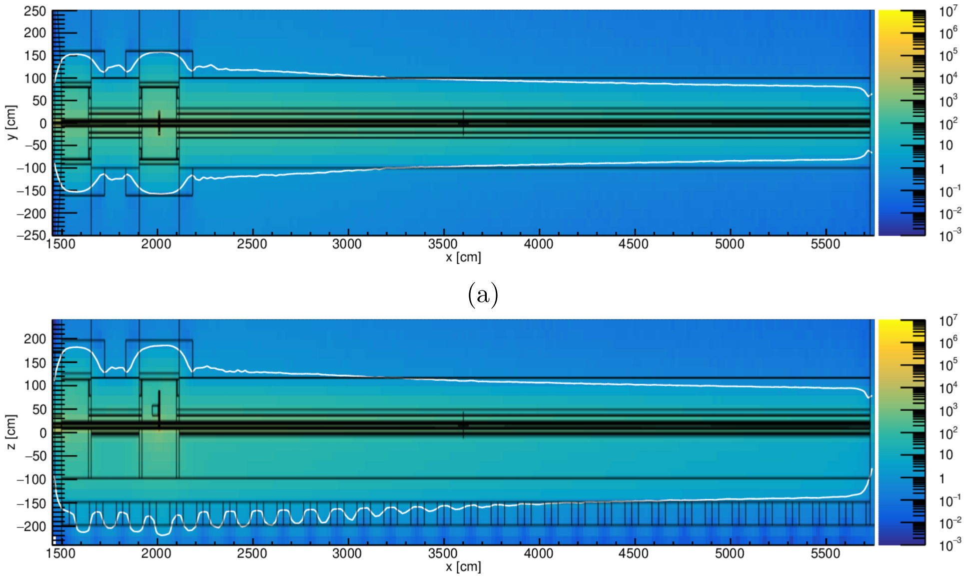

(a)

(b)

Figure 5.24: Common Shielding model (without the borated layer) top-view (a) and side-view (b) of the photon dose rate map with a 70 cm thick concrete layer.

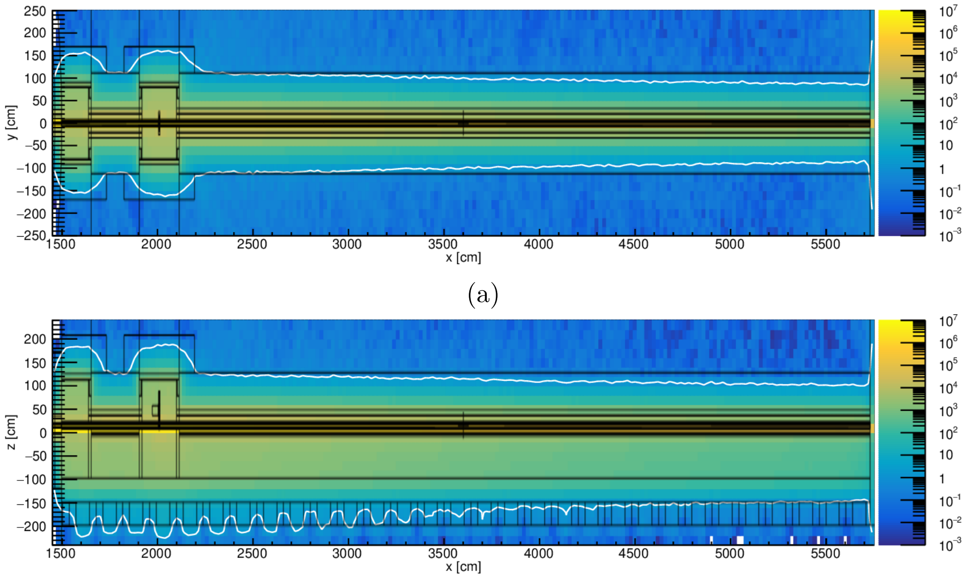

(a)

(b)

Figure 5.25: Common Shielding model (without the borated layer) top-view (a) and side-view (b) of the neutron dose rate map with a 80 cm thick concrete layer.

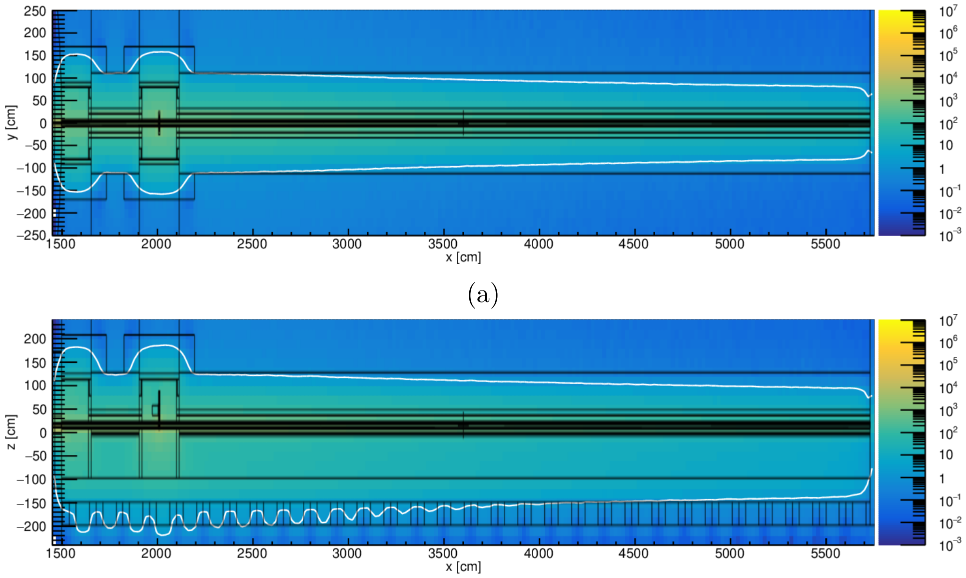

(a)

(b)

Figure 5.26: Common Shielding model (without the borated layer) top-view (a) and side-view (b) of the photon dose rate map with a 80 cm thick concrete layer.

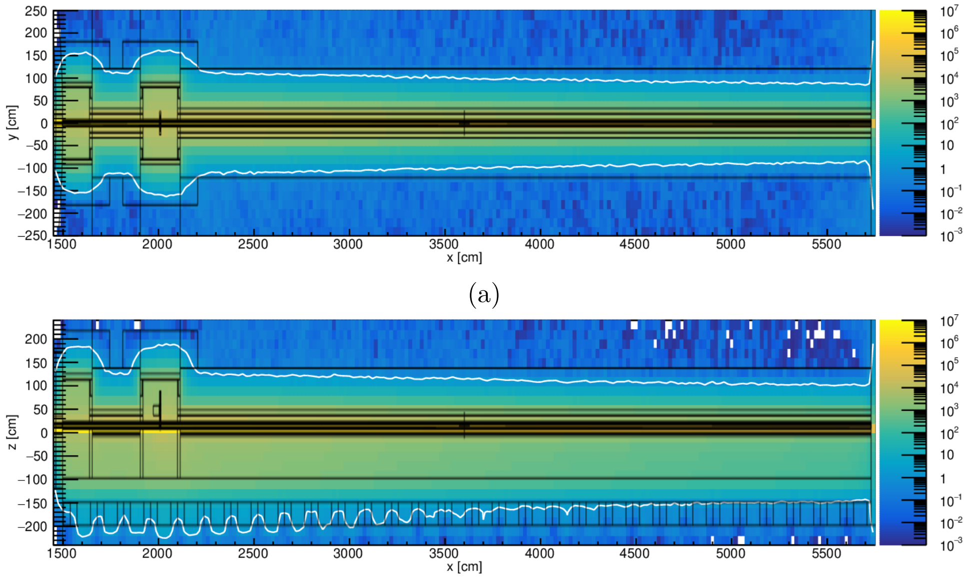

(a)

(b)

Figure 5.27: Common Shielding model (without the borated layer) top-view (a) and side-view (b) of the neutron dose rate map with a 90 cm thick concrete layer.

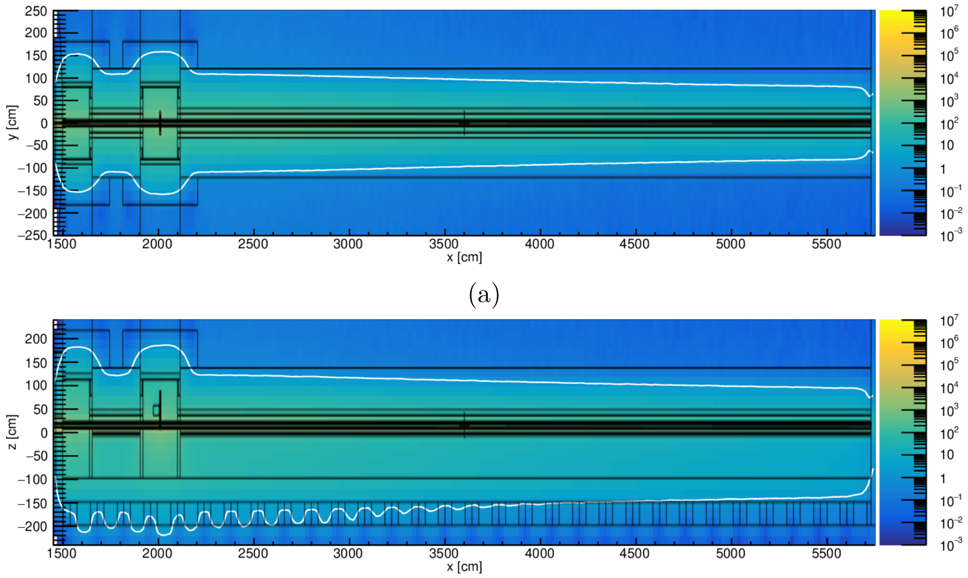

(a)

(b)

Figure 5.28: Common Shielding model (without the borated layer) top-view (a) and side-view (b) of the photon dose rate map with a 90 cm thick concrete layer.

energy part of the beam from the moderator is cut off by the triplet of PSC choppers inside the bunker, so that only neutrons up to 500 meV can find their way to the sample. Thus, the scenario in which the full beam reaches the chopper stuck in a closed configuration is an accident scenario that is being considered as part of the risk assessment for VESPA.

The purpose of the sFOC chopper is to clean the tails of the neutron beam shaped by the choppers inside the bunker. It is not meant to chop off some specific energy ranges from the neutron beam, as opposed to what the PSC choppers do. However the effects of the thermal beam fully impinging on its blades was considered.

A planar fictive neutron source was considered at the entrance of the chopper, that emits neutrons towards the chopper, perpendicularly to its surface. It was set up with the thermal neutron flux (below 1 eV) shown in figure 5.29. The latter is the flux crossing the same chopper entrance, which was calculated with the help of a subsidiary simulation set to use the secondary source.

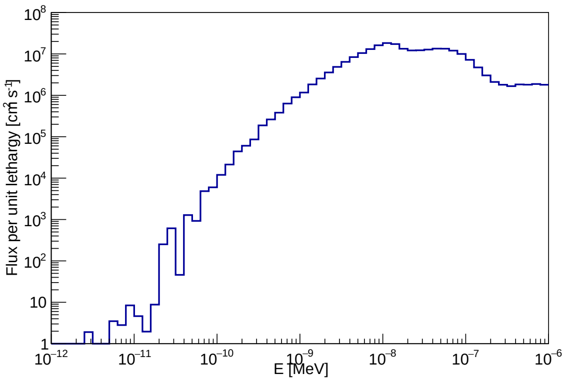

Figure 5.29: The thermal neutron flux, below 1 eV, crossing the entrance of the sFOC. This spectrum was used to set up a fictive thermal source at the same position.

For this calculation, the The design of the choppers for VESPA was not yet completed at the time of writing this thesis. Although the official specifications of the chopper were not available, it is expected that the disks will be made of aluminium, 1 cm thick, and the blades will have an extra coating of B_4C, 2.5 mm thick [40]. This values were added in the MCNP model of the sFOC chopper, shown in figure 5.30 along with the position of the fictive thermal source.

The resulting neutron and gamma dose maps are shown in figure 5.31, where the white lines are set at 1.5 μSv/h and have a relative error below 10%.

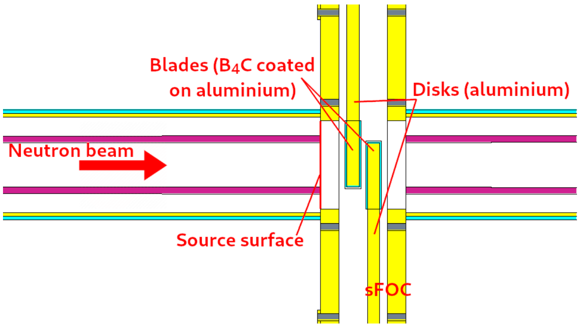

Figure 5.30: Side-view of the sFOC chopper in a fully closed configuration in the MCNP model, also showing the position of the fictive thermal neutron source at its entrance.

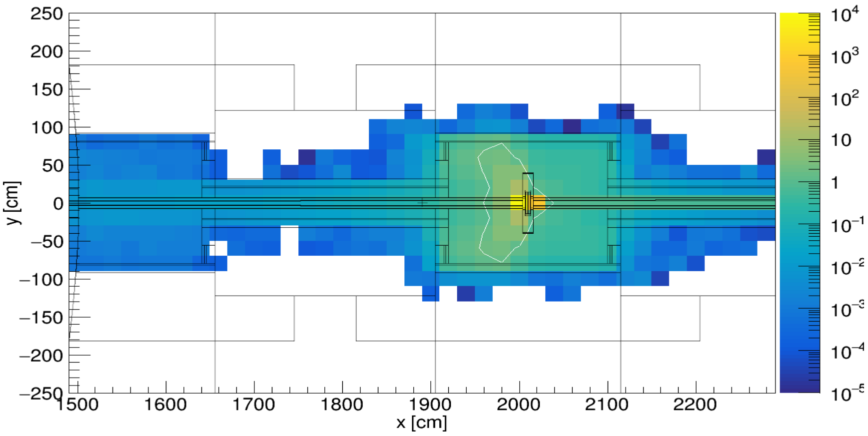

(a)

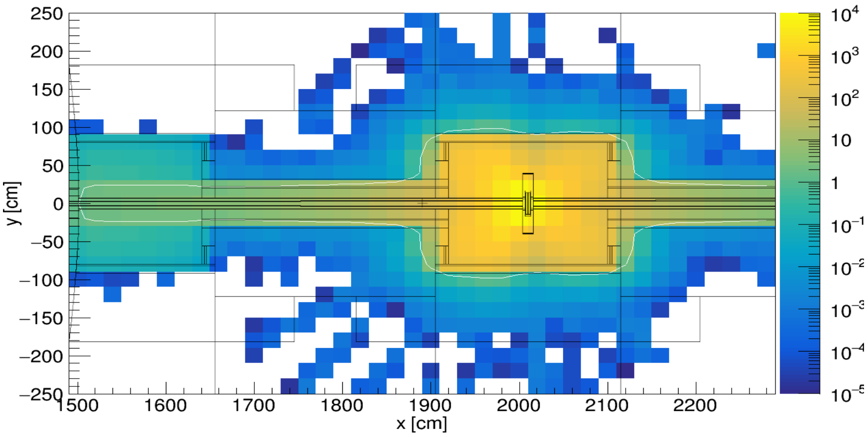

(b)

Figure 5.31: Neutron (a) and gamma (b) dose maps about the two chopper pits outside the bunker, due to a thermal neutron beam impinging on the blades of the sFOC chopper in a fully closed configuration.

5.2.5 Super-mirror for gamma doses

The purpose of the instrument guide is to transport neutrons along the entire length of the beam-line, till the sample position. In order to enhance the neutron flux at the sample, the guide substrate is sputtered with multilayers of Nickel-Titanium (Ni-Ti) so to exploit the optical properties of such material [66]. In fact, total reflections allow slow neutrons hitting the guide walls at low grazing angles to be reflected and thus transported more efficiently [67]. Because of their reflecting properties for neutrons, such guide coatings are also referred as "mirrors".

The smallest grazing angle at which total reflection happens is called "critical reflective angle". The critical reflective angle of Nickel coatings is addressed as "$m = 1$" [67]. Ni-Ti layers can provide critical reflective angles [68] m-times higher than that of bulk Nickel, even up to "$m = 8$" [69]. For that reason, Ni-Ti coatings are referred as "super-mirrors".

MCNP is not capable of adequately simulate the coherent scattering of slow neutrons with the guide walls [69, 70]. In fact, MCNP only consider the scattering on single particles, while the coherent scattering is described by neutron waves interacting with a lattice [69, 70]. Because of that, other codes for ray-tracing like McStas [71] are used for designing the neutron guides [70]. Also, gamma production due to reactions induced by slow neutrons are not correctly simulated in MCNP [69, 70].

The implementation of super-mirror capabilities in MCNP has been already investigated in the past [70]. In fact, it resulted in a patched version of MCNPX by F. Gallmeier [72]. Further studies focused on more recent version of MCNP and led to a patched version of MCNP6 that implements super-mirror capabilities [73, 74]. Such patched MCNP6 provides an enhancement over the patched MCNPX since it allows for a realistic gamma generation on mirror coatings. It also features particle splitting at mirror surface, so that particles are split into a reflected and a transmitted part with proper weights when interacting with mirrors.

5.2.6 Proposed shielding design for VESPA

The results shown in the previous paragraphs suggest that a proper shielding for VESPA can be made of chunks with different layers of ordinary concrete. They also suggest that the innermost layer of borated concrete is not mandatory. Hence, the instrument shielding can be build only with the steel layer and the ordinary concrete layer. The thickness of the latter can decrease along the length of the beam-line, so that the shielding structure can be tapered toward the cave.

The thickness of the ordinary concrete layer which was proposed for the design for the design of the shielding of VESPA are given in table 5.1.

The proposed geometry was tested with a set of simulations, that were

Position [m]	15-25	25-35	35-45	45-∼58
Concrete thickness [cm]	90	80	70	60

Table 5.1: Proposed ordinary concrete thickness for the guide shielding of VESPA.

performed using the patched MCNP6 version mentioned in paragraph 5.2.5. In fact, the purpose is to better evaluate the gamma dose rate map and to confirm that the borated concrete layer can be avoided.

The concrete layers in the MCNP model were changed according to the prescription given in table 5.1. The instrument guide out of the bunker wall was divided into several pieces, 1.5 m long each, in compliance to the guide design of the instrument [37]. The guide elliptical profile in each piece was approximated with planar surfaces. An additional layer of Ni-Ti was added to the borofloat substrate of each piece, and its internal surface was set to act as a supermirror in the patched MCNP6 simulation. The thickness of the Ni-Ti coating was set as shown in table 5.2.

m value	3.0	3.5	4.0	4.5	5.0
Layer thickness [μm]	3.4	3.8	4.9	6.7	9.2

Table 5.2: Ni-Ti layer thickness as a function of the m value.

The m-value profile of VESPA instrument is shown in figure 5.32. Both horizontal and vertical inner guide walls have the same profile.

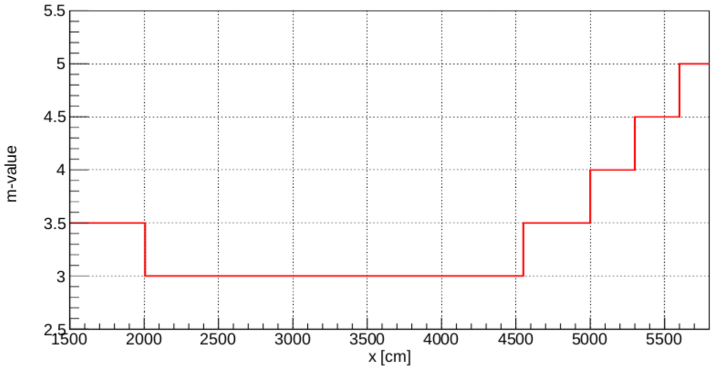

Figure 5.32: m-value profile of VESPA guide out of the bunker.

The results of the simulations are shown from figure 5.33 to figure 5.36 for the geometry with the borated concrete layer. Each neutron and photon map is now followed by the associated relative error map, where the white lines represent a 10% error.

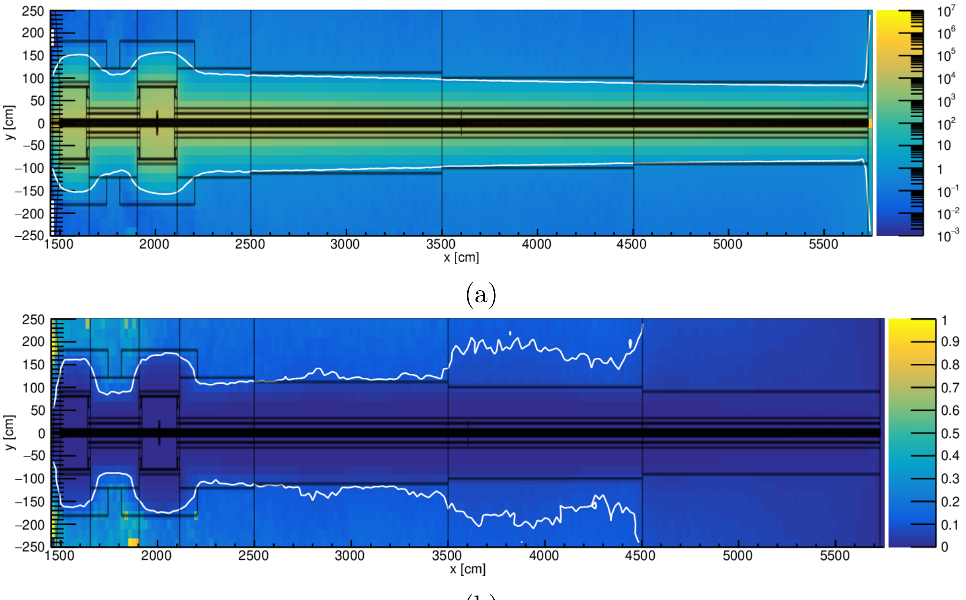

(a)

(b)

Figure 5.33: Top-view (a) and associated relative error map (b) of the neutron dose rate map for the tapered shielding with the borated concrete layer.

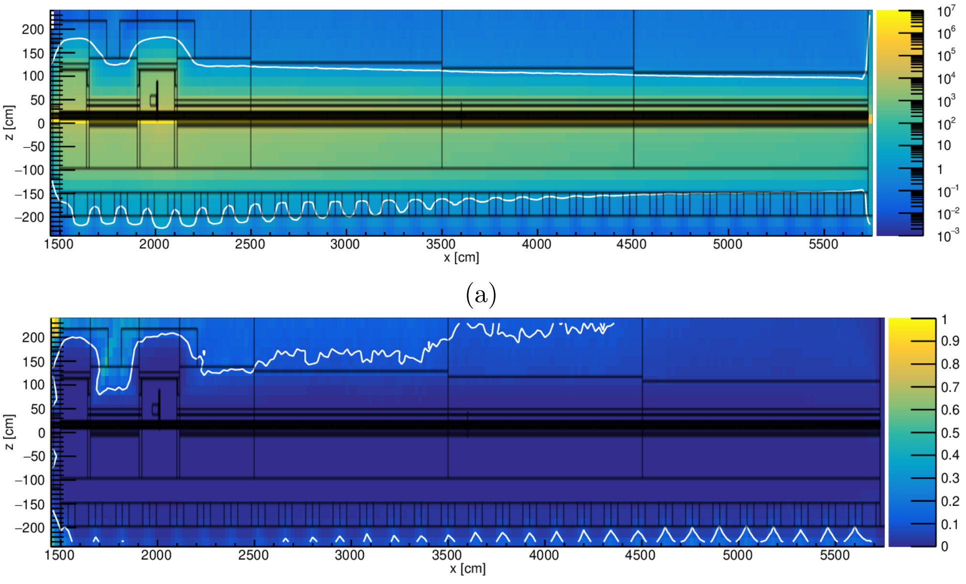

(a)

(b)

Figure 5.34: Side-view (a) and associated relative error map (b) of the neutron dose rate map for the tapered shielding with the borated concrete layer.

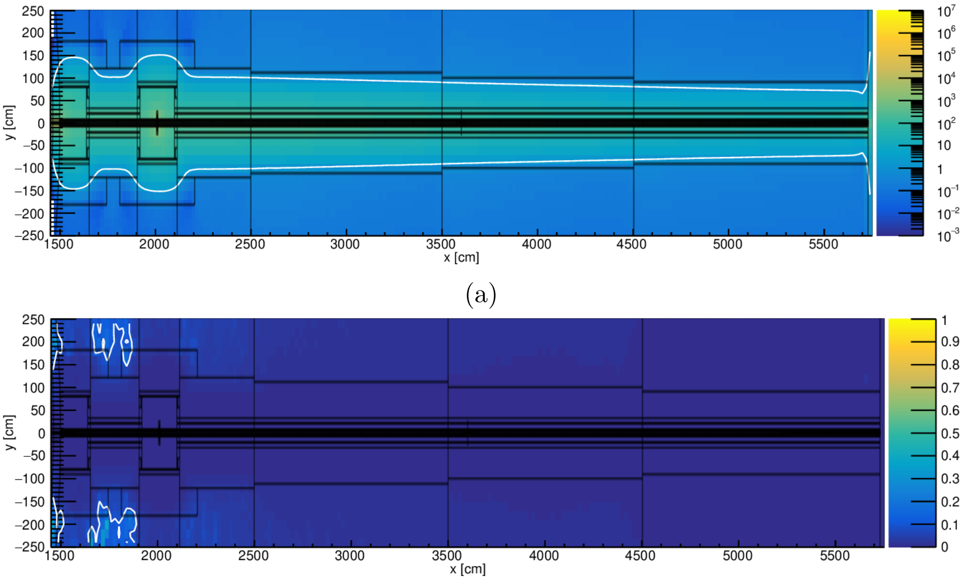

(a)

(b)

Figure 5.35: Top-view (a) and associated relative error map (b) of the photon dose rate map for the tapered shielding with the borated concrete layer.

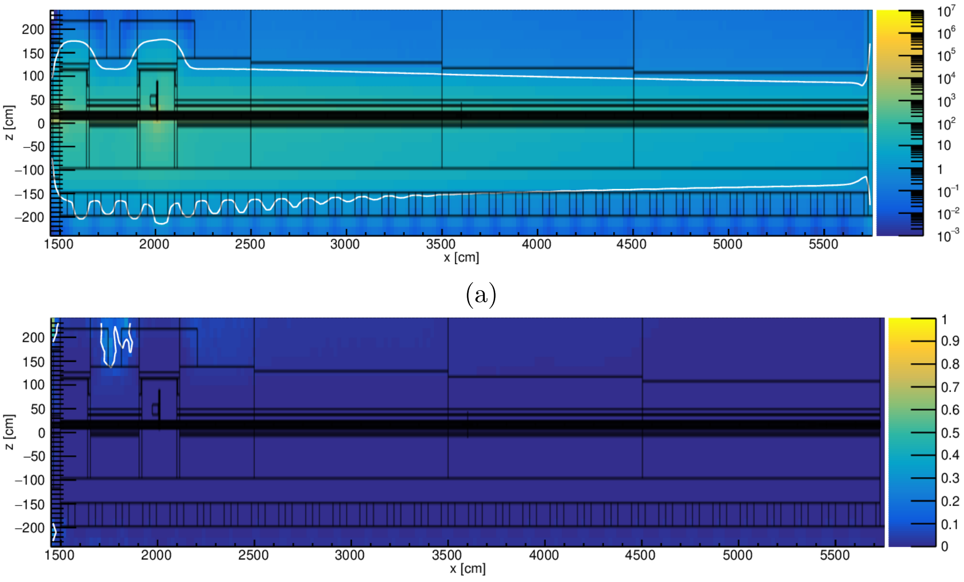

(a)

(b)

Figure 5.36: Side-view (a) and associated relative error map (b) of the photon dose rate map for the tapered shielding with the borated concrete layer.

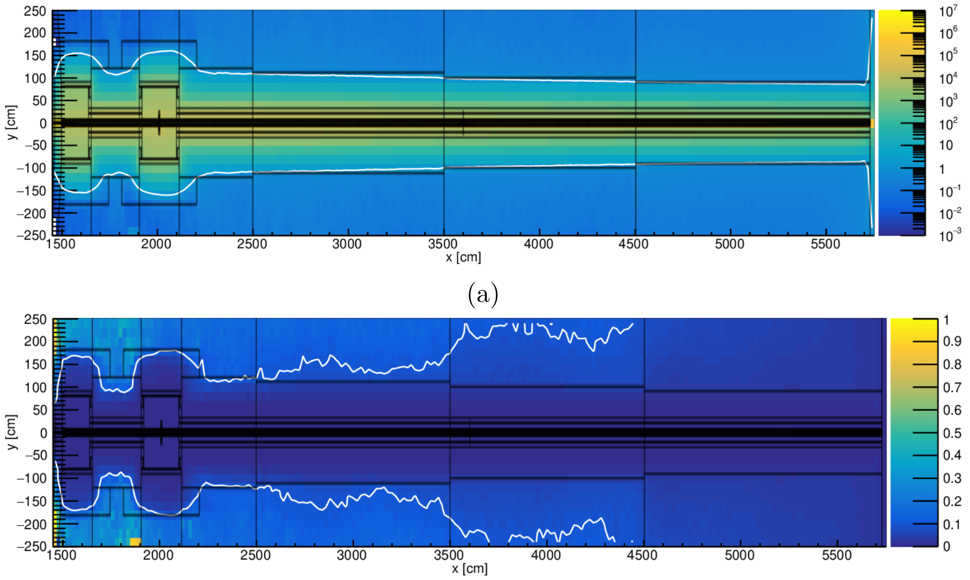

(a)

(b)

Figure 5.37: Top-view (a) and associated relative error map (b) of the neutron dose rate map for the tapered shielding without the borated concrete layer.

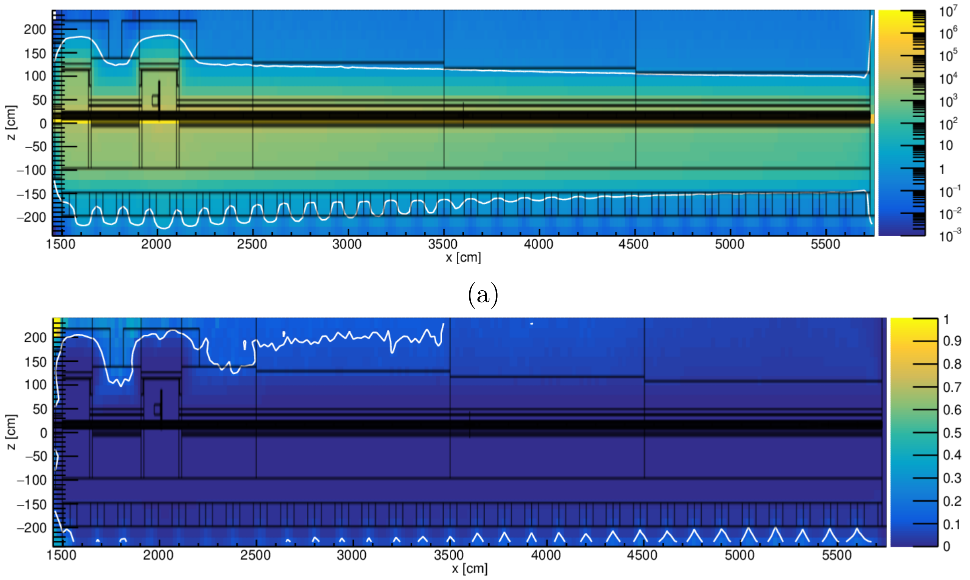

(a)

(b)

Figure 5.38: Side-view (a) and associated relative error map (b) of the neutron dose rate map for the tapered shielding without the borated concrete layer.

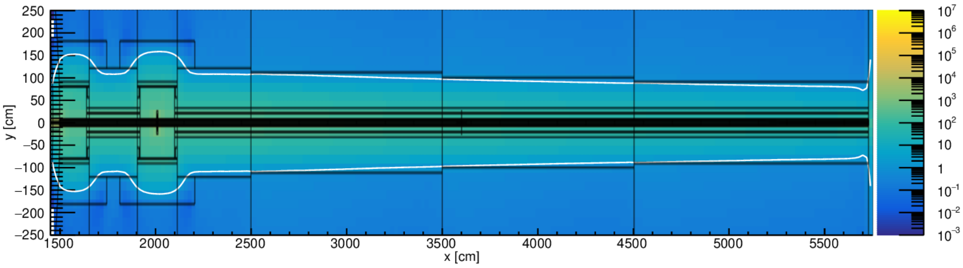

(a)

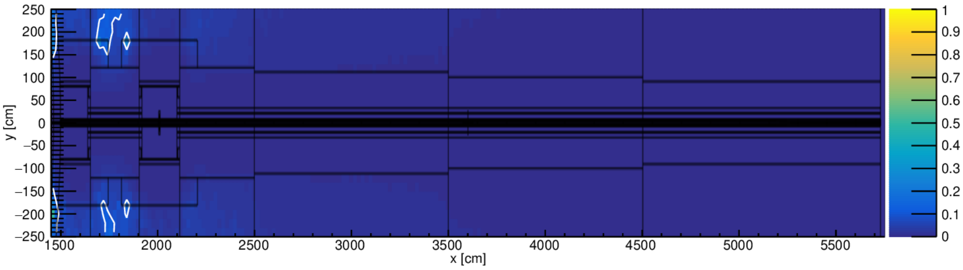

(b)

Figure 5.39: Top-view (a) and associated relative error map (b) of the photon dose rate map for the tapered shielding without the borated concrete layer.

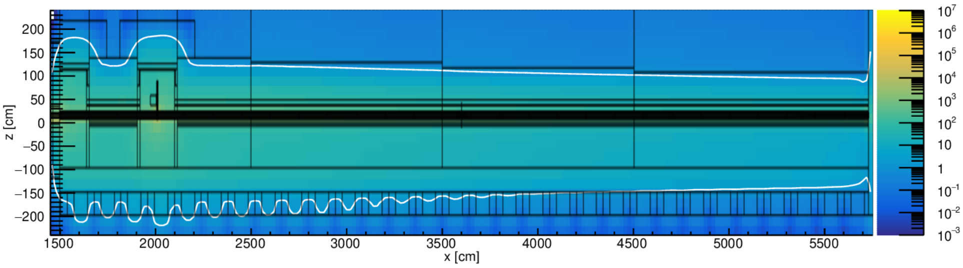

(a)

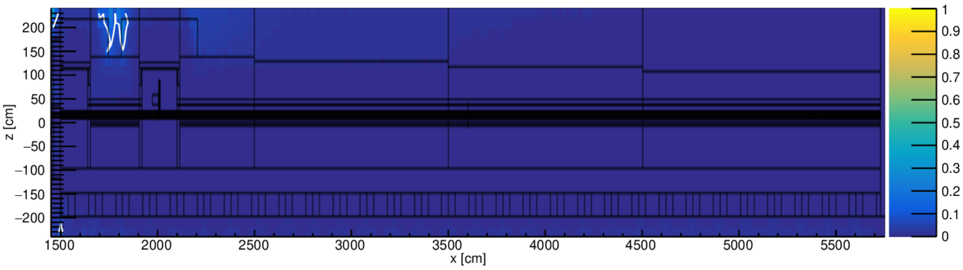

(b)

Figure 5.40: Side-view (a) and associated relative error map (b) of the photon dose rate map for the tapered shielding without the borated concrete layer.

The neutron and photon maps are in compliance with the results given in the previous paragraphs. Even using the patched version of MCNP6 for a more accurate estimation of the gamma dose, it is still of less concern respect to the neutron dose. This can be explained by the fact that VESPA is in direct line of sight with the moderator. Fast neutrons can find their way down the beam-line since the full beam never strikes against the guide wall, as would happen instead in a bending or curving guide geometry.

The results from the calculations show that a suitable shielding for VESPA can be built without the borated concrete layer. A steel layer of 10 cm and a layer of ordinary concrete with the thickness given in table 5.1 are sufficient to meet the limit of 1.5 μSv/h along the entire length of the instrument section in the hall.

All the simulations were performed considering the worst case scenario for the instrument considered in the Common Shielding project, with all the choppers in a full-open configuration. No accident scenario was taken into consideration, since they are to be considered in the risk assessment, that is beyond the scope of this thesis and the Common Shielding project. For there reasons, the proposed design was submitted and accepted as a preliminary design for VESPA [75].

Further simulations can focus on evaluating the effects of the choppers inside the bunker in a full-closed or even semi-closed configuration. They could also focus on a deep evaluation of the effects of the gaps between the guide pieces of 1.5 m length. Other materials could be considered, that could minimize the engineering efforts as well as the weight load on the floor and the structural load, which could lead to guide misalignments or could put a burden on maintenance operations.

5.2.7 Heavy concrete layer

Ordinary concrete is an inexpensive material but it's usually needed in massive quantities when used for shielding purposes [76]. A possible alternative could be to use high-density concrete compounds, which are enriched with iron ores [77], borated minerals or other metal-based minerals [76]. They have proven to have better dose attenuation capabilities compared to ordinary concrete, in spallation facilities [78]. The shielding of VESPA could benefit by replacing the ordinary concrete with some high-density concrete, since the resulting design could make use of thinner concrete layers.

The bunker wall at ESS is made of heavy concrete, which is a mixture of ordinary concrete and magnetite, a mineral ore [79]. It is known at ESS as "heavy concrete". Its detailed composition is given in appendix B.

A simulation was performed, in which the outer concrete layer in the shielding structure is replaced by heavy concrete. The thickness is set to 70 cm. Results for the neutron and photon dose maps are shown in figure 5.41 and in figure 5.42.

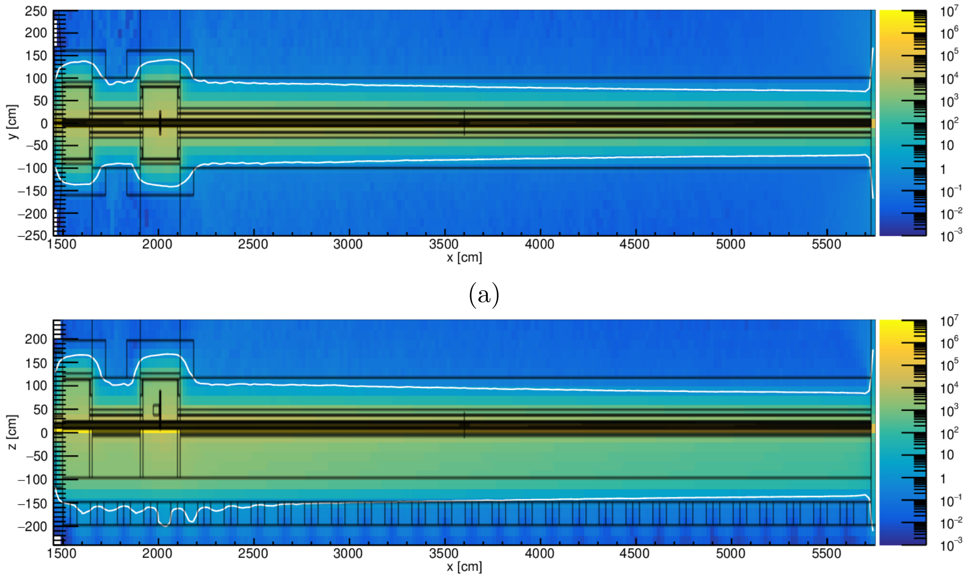

(a)

(b)

Figure 5.41: Top-view (a) and side-view (b) of the neutron dose rate map with a 70 cm thick heavy concrete layer.

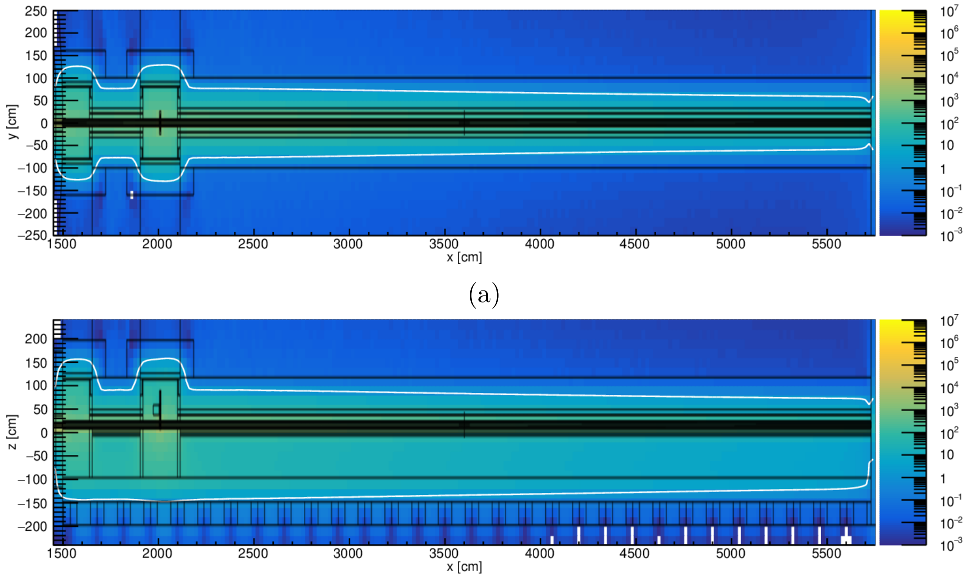

(a)

(b)

Figure 5.42: Top-view (a) and side-view (b) of the photon dose rate map with a 70 cm thick heavy concrete layer.

The isodose lines in the pictures suggest that a 70 cm thick layer of heavy concrete can meet the dose limit of 1.5 μSv/h for the entire beam-line. The design proposed for the shielding of VESPA make use of ordinary concrete layers, as given in paragraph 5.2.6. However, further calculations could show that a tapered shielding design using heavy concrete, like the one proposed with the ordinary concrete layer, could meet the dose requirement.

5.2.8 Guide gaps and steel activation

The instrument guide will be constituted of several guide pieces, 1.5 m long each. They will be place one after another, till the entire length of the instrument. However, a small gap between them can't be avoided. Such gaps can lead to a neutron leakage and, hence, an increased neutron dose can be observed locally. Furthermore, leaked neutrons could activate the steel layer to hazardous levels.

In order to quantify the effects of the guide gaps, a simple geometry was set up, which is shown in figure 5.43.

Only two guide pieces are modelled, with a constant cross section of $5 \times 5\,\mathrm{cm}^2$. The guide substrate is 1 cm thick and it is internally covered by a thin layer of Ni-Ti, 3.8 μm thick. The gap between the two guide pieces is 1 mm wide, which is conservative respect to the expected value of 0.2 mm [80] for VESPA. It was chosen so to allow a better comparison with analogous studies on other beam-lines, which is beyond the scope of this thesis and hence not reported here.

The common shielding design was used, including the innermost layer of borated concrete. At the time of performing these studies, more information about the manufacturing of such layer was available. According to that, the thickness for the borated concrete layer was set to 1.5 cm. The thickness of the next layer of steel was kept to 10 cm, while the thickness of the outer layer was set to 70 cm and its material was set to heavy concrete.

The guide gap is relevant especially for slow neutrons, because fast neutrons have a smaller chance to be captured by the borofloat substrate of the guide, due to the boron cross section [63]. Therefore, fast neutrons can travel across the substrate which is nearly transparent as the guide gap itself. On the other hand, slow neutrons can be captured and have a much higher chance of escaping from the gap. Slow neutrons also have a higher chance to interact with the steel layer and generate penetrating gammas.

Due to the relevance of slow neutrons, the source was set so to generate only the slow neutron region of one of the spectra calculated at the bunker wall exit. In particular, the highest spectrum of figure 4.11(b) was chosen. It is the spectrum of the angular binning $0.1 - 0.15°$ emitted by the candidate source term at the bunker wall exit with a fine binning. The picture in figure 5.44 show that spectrum and the region that was used for defining the source. The neutron current emitted by the source was set to 10^{10} n/sec,

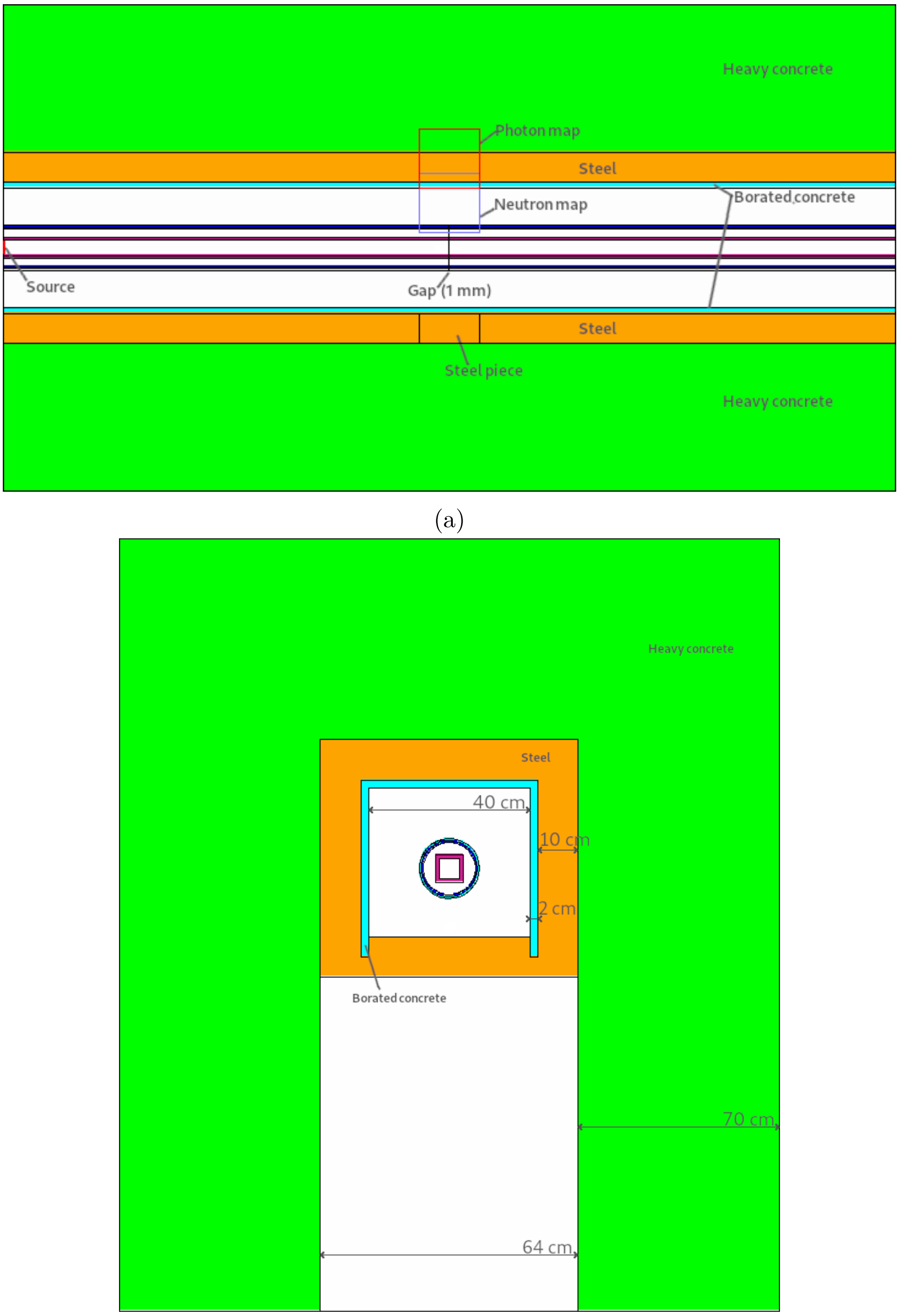

(a)

(b)

Figure 5.43: Top-view (a) and front-view (b) of the geometrical model used for studying the gaps between the guide pieces.

which is similar to the neutron current of $3.68 \cdot 10^9$ n/sec that was calculated for the chosen angular bin.

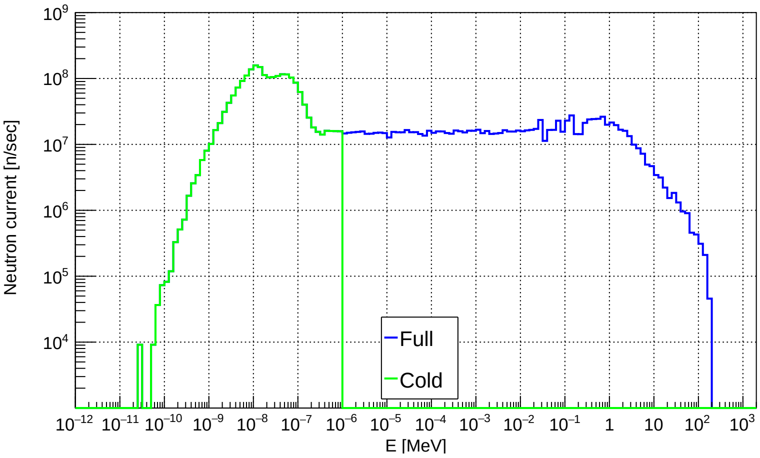

Figure 5.44: Neutron spectrum used to set the source for studying the effects of the guide gaps.

The source was set at one end of the geometry. It is a square surface of $5 \times 5\,\text{cm}^2$, centred at the guide opening and with its normal coincident with the guide axis. Neutrons are generated from the source surface with a starting position that is sampled uniformly. Their emission angle, instead, is sampled uniformly within a cone with a maximum divergence of 5° respect to the guide axis. Such value was chosen so to promote the scattering against the guide walls, that are set to act as supermirrors with a constant m-value of 3.5. That is almost the average m-value of VESPA guide in the East sector hall [37].

Two set of simulations were performed, using the patched MCNP6 version, one with and the other without the borated concrete layer. Neutron and photon flux maps were investigated in both sets, in two different positions on the edge of the inner shielding layers. The boundaries of those maps are shown in figure 5.43(a). The resulting flux maps, integrated over all energies, are shown in figure 5.45 and in figure 5.46.

The two sets of simulations were performed with the same number of primary particles. They also use the same weight windows calculated with ADVANTG [81].

The fact that neutron flux maps with and without the borated concrete layer in figure 5.45 show a different statistics is already a confirm of the effect of such layer in capturing slow neutrons. On the other hand, the similar photon flux maps suggest that the borated concrete layer is not mandatory for the shielding design of VESPA, as already shown in paragraph 5.2.3.

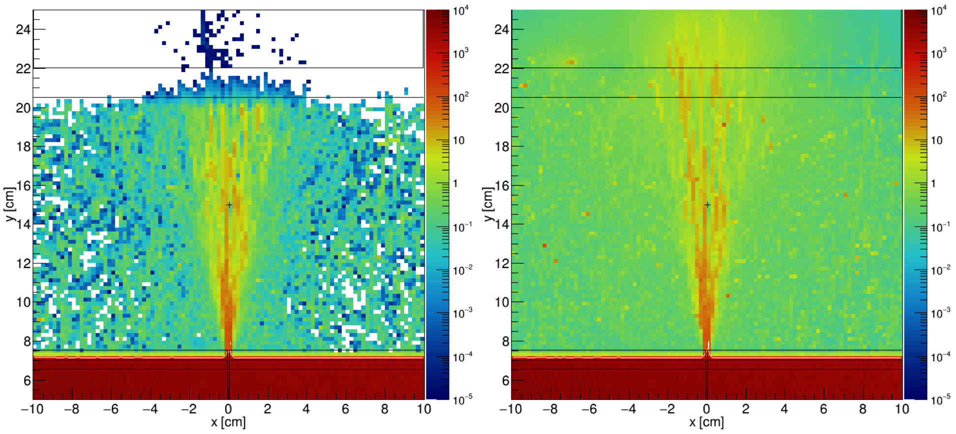

(a) (b)

Figure 5.45: Integral neutron flux map with (a) and without (b) the borated concrete layer.

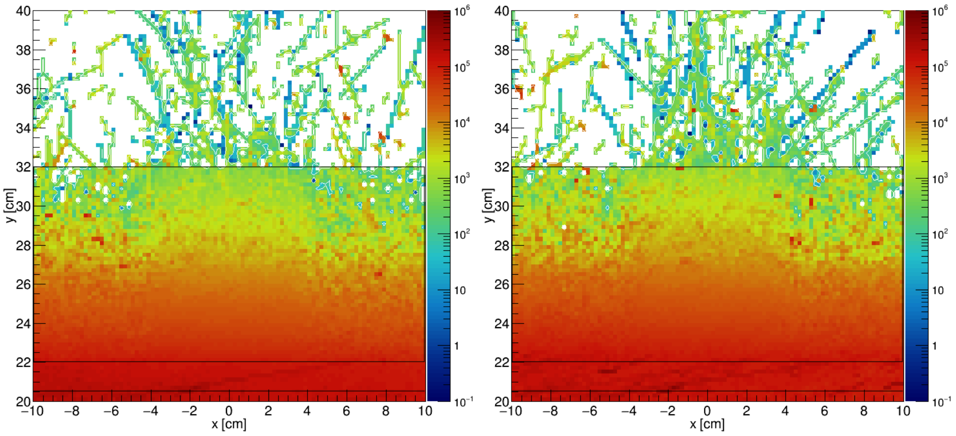

(a) (b)

Figure 5.46: Integral photon flux map with (a) and without (b) the borated concrete layer.

The steel activation in the gap region was calculated with a similar geometrical setup. The main difference is that the source was defined so to use the full spectrum of figure 5.44, in order to not underestimated the effects of fast neutrons.

Only one piece of the steel layer was considered, whose size is $10 \times 20 \times 20\,\mathrm{cm}^3$. It is shown in figure 5.43(a).

The volume averaged neutron flux spectrum in that steel piece, with and without the borated concrete layer, is shown in figure 5.47.

The neutron flux at the steel piece was used as an input for CINDER

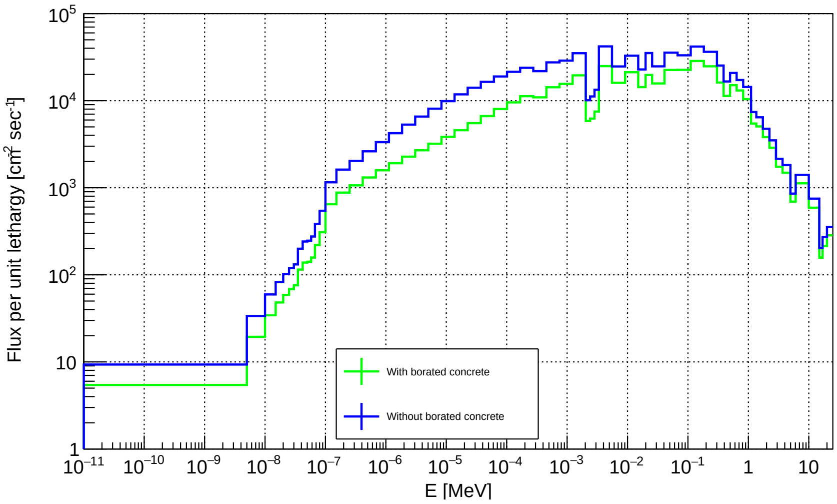

Figure 5.47: Neutron flux at the steel piece, with and without the borated concrete layer.

[82], in order to calculated a gamma source after 5400 h of irradiation time. That is the amount of time that ESS is expected to operate in one year.

The gamma source replaced the neutron source in the geometrical model and the MCNP simulation was run again. The result is the gamma dose rate map shown in figure 5.48, with and without the borated concrete layer, due to the gammas emitted by the activated steel piece. The white line is set at 1.5 μSv/h.

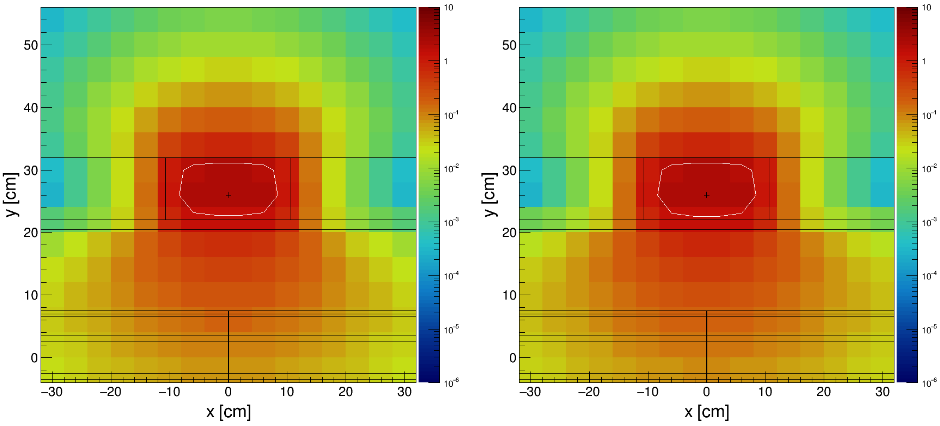

(a)

(b)

Figure 5.48: Dose rate maps due to the gammas emitted from the activated steel piece, with (a) and without (b) the borated concrete layer.

The dose maps due to gamma activation show that, without the borated concrete layer, the dose rate is slightly higher in that area where such layer is missing. However the difference is minimal and both cases meet the dose requirements.

The graph in figure 5.49 shows the activation of the selected steel layer block right after the irradiation ends (time-step: 0 h) and the residual activation at four different cumulative time-steps (after 1 h, 6 h, 1 d and 1 w after the irradiation ends). For each time-step, two couple of bars are plotted, one for the case with the borated concrete layer (in the foreground), the other for the case without that layer (in the background). It is clear from the picture, and it is in line with the expectations, that in the case in which the borated concrete layer is missing, and hence it can't act as shield for the steel layer, the latter show a higher activation.

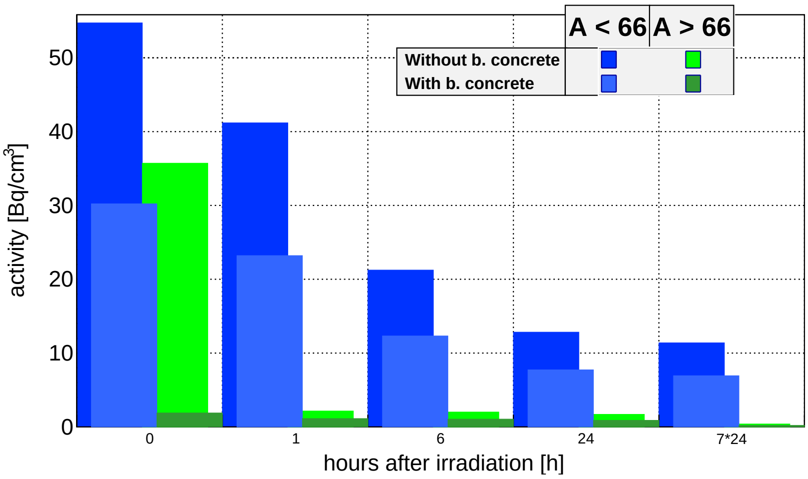

Figure 5.49: The residual activity of the steel slab at different cumulative time steps after 5400 h of irradiation.

The most abundant activated isotopes have mass numbers $A < 66$, as shown in the first bars in each time-step. The bars on the right, instead, show the activation for heavier isotopes, where the heaviest isotope is antimony Sb ($A \simeq 123$).

The residual activity right after the end of the irradiation leads to the dose maps given in figure 5.48. Although both of those maps show that the gamma dose of the steel slab meet the dose requirement, it must be noted that the most abundant isotopes in both cases (with and without the borated concrete layer) are mainly Mn$-$56, Cu$-$64, Fe$-$55 and Co$-$60. Among those, iron can be considered the less harmful. The half-life of its decay by electron capture is of $\sim 2.73\,\text{y}$, which is large if maintenance or decommissioning operations are considered. However it emits only a low energy gamma of $E \simeq 126\,\mathrm{keV}$, which is not to be considered an hazard, especially if compared to the gammas emitted by the other isotopes [83]. In fact, the other three isotopes emit gammas in the range of hundreds of keV (like the $\sim 847\,\mathrm{keV}$ from manganese) to a few hundreds of keV above 1 Mev, as in the case of Co−60. Among them, cobalt is indeed the most harmful, not only because it emits mainly gammas of $\sim 1173\,\mathrm{keV}$ and $\sim 1333\,\mathrm{keV}$, but also because it is a long-lasting isotope due to the long half-life of its β decay of $\sim 5.3\,\mathrm{y}$ [83]. In comparison, Mn−56 and Cu−64 have half-lives of $\sim 2.5\,\mathrm{h}$ and $\sim 12.7\,\mathrm{h}$ respectively, and hence they give a negligible contribution to the dose after a few days from the end of the irradiation. In addition, copper emits a high energetic gamma of $\sim 1345\,\mathrm{keV}$ only in a fraction of the cases (less than 0.5%). A cobalt source is a well-known radiation hazard [84, 85], but it must noted that the considered steel slab shows a low rate of decay a $\mathrm{Bq/cm^3}$. Considering the graph shown in figure 5.49, the radiation risk can be consistently reduced if handling operations will comprise of short exposure times after a few days after the irradiation, or if they will be driven remotely, which is the planned scenario at ESS.

Data about the gamma dose rate are not of direct interest for the shielding of the instrument. However, they are required to determine the procedures for the handling of VESPA shielding dismantling when the instrument will be decommissioned, at the end of his life-time. They are also needed so to define maintenance procedures during normal operations. These results show that the borated concrete layer is not crucial even for such procedures.

Chapter 6

Heavy Shutter

The heavy-shutter is a component of the instrument that prevents the neutron beam to reach the sample position during normal operations. It is a mandatory element because it allows to access the experimental cave of VESPA without having to switch off the entire ESS facility.

This chapter is about the calculations performed in order to provide a preliminary design of the heavy-shutter for VESPA.

6.1 Beam attenuator

The last part of VESPA beam-line, after the straight guide section investigated in the previous chapters, consists of the experimental cave, the sample preparation area and the hutch, as explained in paragraph 3.2.2. Of the two rooms of the experimental cave, the one in the bottom contains the spectrometer, while the one on top will be used to put the sample in position through a hole in the floor that interconnects the two rooms.

In order to access any of the two rooms of the cave for maintenance, normal operations or for any other reason, the neutron beam coming from the moderator has to be stopped so to not irradiated people. There's the need for a beam attenuator, placed in a feasible position along the beam, that stops or, at least, massively attenuates the beam.

6.2 Geometrical constraints

The position that was considered for VESPA heavy-shutter is at the end of the section inside the bunker, next to its wall, as shown in figure 3.5. Such position allows easy access to the instrument section in the hall, outside the bunker, during ESS normal operation. Also, it doesn't impact on the Common Shielding and, hence, it doesn't affect its design.

Due to the selected position, the heavy-shutter can be thought as a replacement of the bunker wall. It has to provide a similar attenuation power, so to reduce the dose rate below 3 μSv/h out of the bunker, in the instrument guide [17]. As for the studies for the beam-line shielding, such value has to be reduced by a factor of 2 when investigations are performed using MCNP code [15].

Since the bunker wall is designed to meet the required dose limit, it is then logical to assume that the heavy-shutter could be designed with the same parameters. That is, a 3.5 m long bulk of heavy concrete. However, this is an impracticable way due to the excessive length of such heavy-shutter, its weight loss and the subsequent burden in the design of an adequate handling system. Furthermore, the space available for the heavy-shutter in VESPA beam-line is at maximum $\sim$ 1.2 m long [40], due to a chopper close to the bunker wall. On the other hand, such bulk of heavy concrete would put a burden on the handling, maintenance, and so on.

The purpose of performing neutronic calculations for the heavy-shutter is to determine a suitable design, that can fit in the available space and that meets the required dose limit at the bunker wall exit. This requires to determine appropriate materials and geometry so to minimize the weight load, manufacturing and other engineering constraints.

6.3 Material selection

The selection of appropriate materials for the heavy-shutter is a crucial part in its design studies. They directly affect the dose rates and thus have to be chosen wisely. A good material is, in fact, a material which minimizes the length of the heavy-shutter while meeting the requirements for the dose rates, and that also minimizes the activation of the component.

A group of materials was tested in a simplified MCNP geometry that recalls the one typically used for transmission studies, as described in paragraph 1.6.1. A collimated neutron beam hits a bulk of a single material, 25 cm in length, and the transmitted flux at the opposite end is recorded. Neutron energy at the source is chosen according to the spectrum calculated in the guide section, after the fourth chopper, inside the bunker. The results are shown in figure 6.1, in which the source spectrum is the one detected after travelling in a void bulk. For that reason, it is labelled as "void".

According to the resulting spectra, there isn't one single material, among those that were tested, that is sufficient to attenuate neutrons of any energy. A good compromise can be to use at least two materials, one that mainly attenuates fast neutrons of energy above 1 MeV, the other for neutrons of lower energy. The transmitted spectra suggest that those materials can be copper and B_4C, respectively. In fact, the former is the one that leads to the smallest spectrum above $\sim$ 1 MeV, at high energy [86]. B_4C, instead, is the most efficient in stopping neutrons of energies below $\sim$ 1 eV.

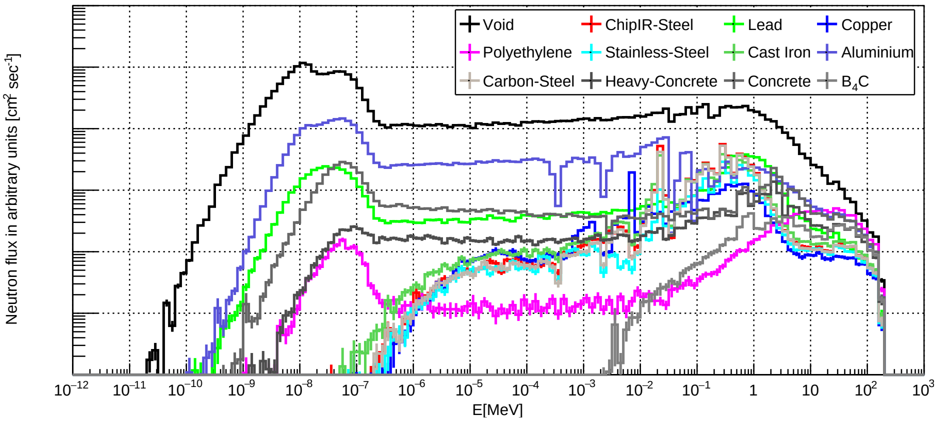

Figure 6.1: Neutron spectra transmitted after penetrating a 25 cm thick bulk of several materials.

6.4 Model

The transmitted spectra of figure 6.1 show that 25 cm of B_4C can heavily absorb neutrons of energy below 1 MeV. Thus, such thickness can be more than sufficient for VESPA heavy-shutter. The other candidate material, copper, also show a good capability in attenuating neutrons of energy below ~ 1 MeV. The coupled effect of the two materials can lead to the need of a smaller bulk of B_4C. For there reasons, the design that was investigated consists of a parallelepiped whose base is $20 \times 10\,\text{cm}^2$. It is made of a variable amount of copper, followed by 20 cm of B_4C, as shown in figure 6.2. The two materials are wrapped in a 1 cm steel casing. The entire object is placed so to have its axis in line with the guide axis. Also, the 1 cm was left between the internal surface of the bunker wall and the end of the heavy-shutter [38].

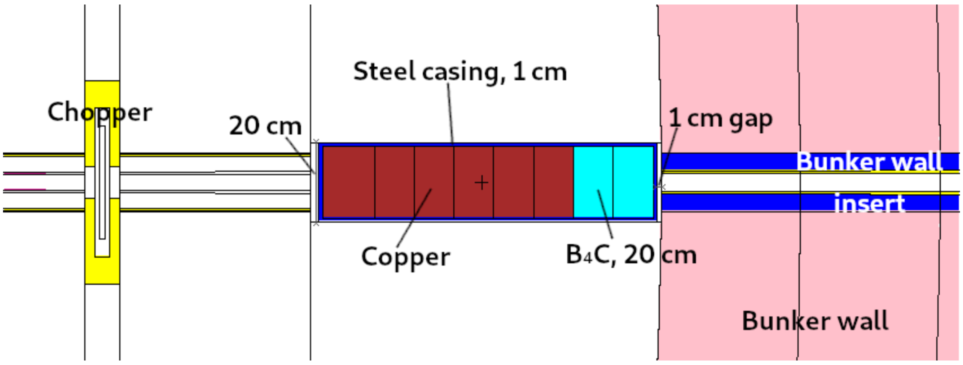

Figure 6.2: Top-view of the heavy-shutter design investigated for VESPA.

This design for a heavy-shutter closely recalls the one that is proposed for the TEST beam-line [87], which makes use of a bulk of high-density polyethylene, HDPE, instead of B_4C. The latter is used as a neutron window in the casing. The polyethylene that was tested in the previous paragraph, shows interesting absorbing properties in figure 6.1 for neutron of energy below 1 MeV. However, polyethylene is rich of hydrogen, which makes it more suitable as a moderator material. On the other hand, boron has a higher cross section for neutron capture followed by alpha emission than that of the radiative capture of hydrogen [63]. Thus, boron-enriched materials can be efficient neutron absorber, suitable for shielding applications.

Having slow neutrons in the bunker wall might not constitute an issue because of their small impact on the dose. Also, they might be absorbed by the steel in the bunker wall insert and, hence, not contributing to the dose at the bunker wall exit. However, the choice between B_4C and HDPE was mainly driven by the flammability of HDPE [88]. It was decided not to investigate on HDPE so to avoid any chance to discard the studies in the future, due to such concern.

6.5 Neutron and photon dose rates

A series of MCNP simulations was set up in order to determine the minimum amount of copper needed to match the requirement of $1.5\,\mu$Sv/h at the exit of the bunker wall. Since the purpose is to study a component inside the bunker, the calculations were set so to make use of the primary source from ESS, at the monolith entrance. They also make use of weight windows input files, produced by using the CombLayer model of VESPA and CombLayer code.

Due to the geometrical constraints described in paragraph 6.2, simulations started by considering a heavy-shutter of 110 cm. It is constituted of 88 cm of copper, followed by 20 cm of B_4C, wrapped in a 1 cm thick steel casing. The total length was chosen so to covers almost all the available space from the chopper to the bunker wall. At each simulation, the copper thickness was decreased by 5 cm, from 88 cm to 58 cm. The resulting neutron dose rates from each simulation, calculated at the bunker wall exit, are shown in figure 6.3.

The photon dose rate is not reported in the picture because it is compatible negligible in comparison to the neutron dose rate, since its value is on the order of $10^{-2}\,\mu$Sv/h at the exit of the bunker wall (15 m from the moderator centre). This can be attributed to the amount of B_4C that is shown to be sufficient for absorbing most of the neutron with energy lower than 1 MeV.

The results suggest that a 85 cm long heavy-shutter can be sufficient for VESPA. In particular, it could be made of 63 cm of copper, 20 cm of B_4C a

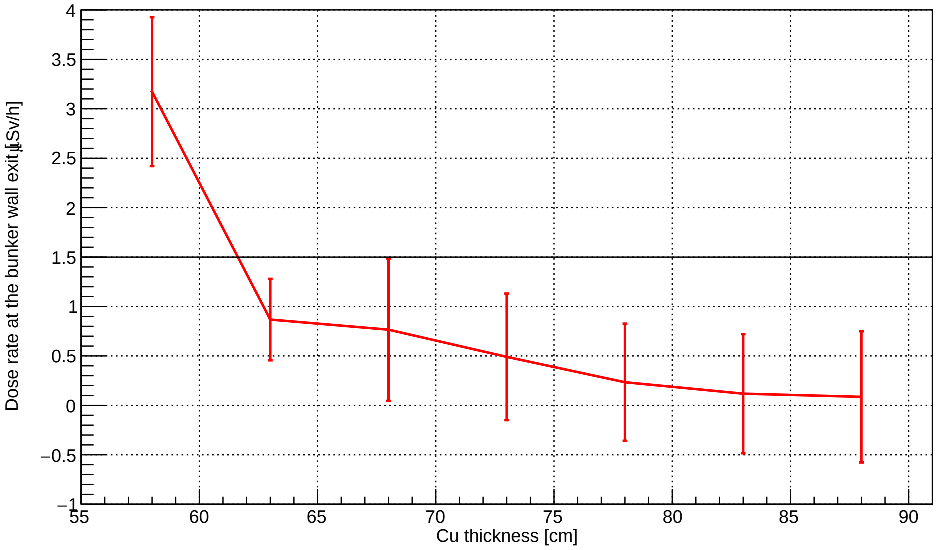

Figure 6.3: Neutron dose rates at the bunker wall exit, due to heavy-shutters with different thickness of copper.

1 cm thick steel casing. The complete neutron and photon dose rate maps for a 85 cm long heavy-shutter are shown in figure 6.4.

6.6 Future studies

The simulations performed so far set an upper limit to the length of the heavy-shutter for VESPA. However, further simulations should focus on improving the results, which are affected by significant relative errors. In particular this is true for the neutron dose rate maps that show an error of 27.84% inside the bunker wall feed-through, at the position in which the dose is 1.5 μSv/h.

The studies show that the photon dose rate is not of a concern for the heavy-shutter. However, activation analysis should be performed in order to determine the dose due to gammas emitted by the activated material. This is an important information to have for maintenance purposes. In fact, it is needed in order to estimate the required waiting time to access the section inside the bunker, after the neutron production is stopped at the ESS target. It is particularly crucial for VESPA because the activation of the heavy-shutter described in this chapter is rather sensible to the purity of copper [89].

Further simulations should also focus in refining the cross sectional shape of the heavy-shutter, and should consider additional wrapping materials that

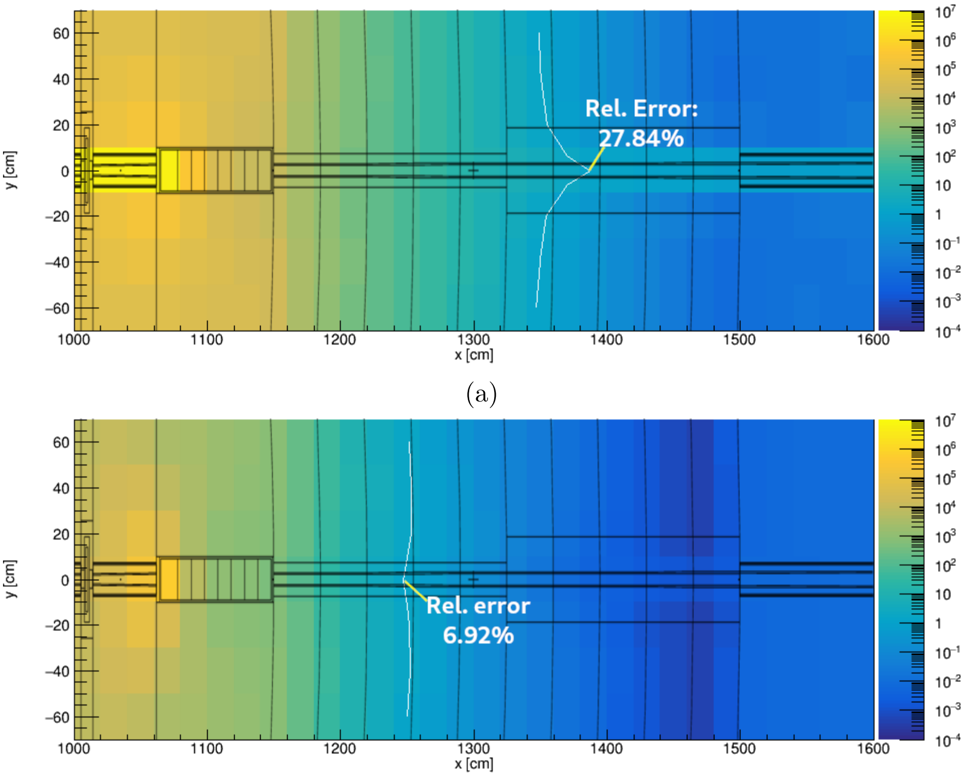

(a)

(b)

Figure 6.4: Top-view of the neutron (a) and photon (b) dose rate maps due to a 85 cm long heavy-shutter. White lines are iso-dose lines set at 1.5 μSv/h.

could help reducing neutron and photon leakage inside the bunker. In fact, neutrons scattered in the heavy-shutter could escape from it in slanting directions, and hence hit and eventually be absorbed in the surrounding objects inside the bunker. That could contribute to locally increase the dose rate and the activation of the materials inside the bunker. Also, an adequate wrapping of the heavy-shutter can sensibly reduce the waiting time for handling and maintenance.

Conclusions

The studies reported in this thesis were focused on designing an adequate shielding for the beam-line of VESPA. VESPA is one of the initial suite of 15 instruments that will be built at ESS. It is a medium instrument, in straight line of sight with ESS moderator and whose sample is at about 60 m from it. VESPA will be the only inverse geometry spectrometer fully dedicated to in-situ research at ESS, for chemical and material science applications.

The work on the shielding of the instrument was focused on designing an adequate shielding for the instrument in the section outside ESS bunker wall, till the sample position. The shielding has to meet the requirement set by ESS on the dose rate limits in the considered area.

Investigations were performed by using Monte-Carlo simulations. MCNP code was used as the main tool for such purpose. Other codes like ADVANTG, CombLayer and CINDER90 were also used to provide additional input files or to perform specific studies on material activation and particle tracks. The geometrical input files required for performing MCNP simulations were produced with the help of an existing model of the instrument, available in CombLayer, and with the help of engineering drawings and several instrument specifications.

VESPA joined the Common Shielding Project, which aims to standardize the shielding structure for all the instruments involved. It also provides a common work-team for presenting, discussing and validating the neutronic calculations. The project provided a standard an modular geometry for the beam-line shielding, that was tailored and investigated for the specific case of VESPA.

The challenging geometrical layout of the beam-lines respect to ESS facility, as well as the intrinsic complexity of the spallation reactions, put a burden on Monte-Carlo simulations. Additionally, the ultimate purpose of shielding studies is to largely attenuate the particle flux in some specific region. In order to overcome these issues, ESS provided a set of calculated neutron sources for several instruments.

A significant part of the thesis is focused on setting up a calculated neutron source by ESS. That primary source was used to define a secondary source at the entrance of ESS bunker wall. The latter was used for performing all the investigations on the shielding of VESPA, outside the bunker wall, till the sample position.

The investigations showed that the beam-line shielding is mainly driven by neutrons. This is in accordance with the expectations for a beam-line in straight line of sight with the moderator. The outcome is a proposed shielding design that was accepted within the Common Shielding Project and by the instrument team as the proposed design for the instrument. It was also presented in a conference and accepted for a paper that has been reviewed at the current time of writing.

The thesis ends with a set of studies on the heavy-shutter, which is an essential component for the instrument. In fact, its purpose is to stop the neutron beam from the moderator so to allow access to sample and for maintenance. The studies on the heavy-shutter allowed to determine an upper limit in the dimensions of the component. They proved that the available space for the heavy-shutter is sufficient for VESPA. However, more investigations are needed in order to refine its shape. There's also the need to produce activation analysis with the purpose to determine additional layers of materials that wrap the heavy-shutter so to self-shield the component and reduce side leakage.

The studies on the beam-lines shielding were performed considering the normal operational scenario of the instrument, with all the choppers in a fully-open configuration. Additional studies should focus on investigating the effects of choppers in fully-closed or semi-closed configurations, as well as considering accident scenarios. Future studies can also concentrate on investigating alternative materials that might reduce the size of the shielding structure and its weight load.

A possible and natural development of the work presented in this thesis is the study of the instrument cave. In fact, such component requires similar shielding studies and similar dose limit requirements. Studies on the cave depart from the Common Shielding Project, and might require a more strict care on the geometrical constraints due to the facility layout.

Appendix A

Fluence to dose conversion functions

The input values used for evaluating the effective doses from neutron and gamma fluences are reported in the following tables.

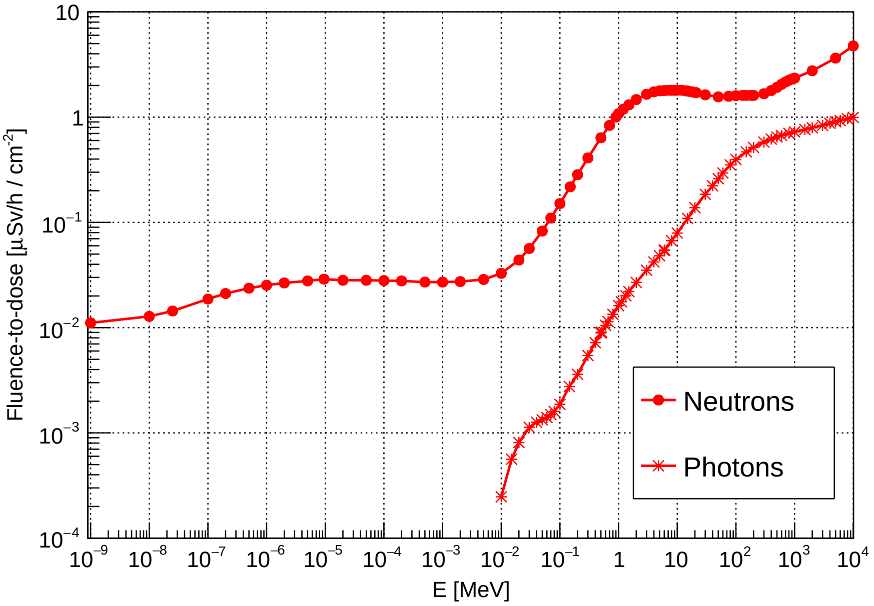

Figure A.1: Fluence to effective dose functions for neutrons and gammas.

E [MeV]	D/Φ [μSv/h/cm^2]
1.00E-9	1.11E-2
1.00E-8	1.28E-2
2.50E-8	1.44E-2
1.00E-7	1.87E-2
2.00E-7	2.11E-2
5.00E-7	2.37E-2
1.00E-6	2.53E-2
2.00E-6	2.66E-2
5.00E-6	2.78E-2
1.00E-5	2.82E-2
2.00E-5	2.82E-2
5.00E-5	2.82E-2
1.00E-4	2.80E-2
2.00E-4	2.78E-2
5.00E-4	2.71E-2
1.00E-3	2.71E-2
2.00E-3	2.74E-2
5.00E-3	2.87E-2
1.00E-2	3.28E-2
2.00E-2	4.39E-2
3.00E-2	5.65E-2
5.00E-2	8.28E-2
7.00E-2	1.10E-1
1.00E-1	1.51E-1
1.50E-1	2.18E-1
2.00E-1	2.84E-1
3.00E-1	4.10E-1
5.00E-1	6.37E-1
7.00E-1	8.35E-1
9.00E-1	1.00E+0
1.00E+0	1.08E+0
1.20E+0	1.19E+0
1.50E+0	1.31E+0
2.00E+0	1.47E+0
3.00E+0	1.65E+0
4.00E+0	1.74E+0
5.00E+0	1.78E+0
6.00E+0	1.79E+0
7.00E+0	1.80E+0
8.00E+0	1.80E+0
9.00E+0	1.80E+0
1.00E+1	1.80E+0
1.20E+1	1.80E+0
1.40E+1	1.78E+0
1.50E+1	1.77E+0
1.60E+1	1.76E+0
1.80E+1	1.74E+0
2.00E+1	1.72E+0
2.10E+1	1.71E+0
3.00E+1	1.63E+0
5.00E+1	1.56E+0
7.50E+1	1.58E+0
1.00E+2	1.60E+0
1.30E+2	1.61E+0
1.50E+2	1.61E+0
1.80E+2	1.61E+0
2.00E+2	1.61E+0
3.00E+2	1.67E+0
4.00E+2	1.79E+0
5.00E+2	1.92E+0
6.00E+2	2.05E+0
7.00E+2	2.16E+0
8.00E+2	2.24E+0
9.00E+2	2.30E+0
1.00E+3	2.35E+0
2.00E+3	2.76E+0
5.00E+3	3.64E+0
1.00E+4	4.75E+0

Table A.1: Neutron fluence to dose conversion factors.

E [MeV]	D/Φ [μSv/h/cm^2]
1.00E-2	2.47E-4
1.50E-2	5.62E-4
2.00E-2	8.10E-4
3.00E-2	1.13E-3
4.00E-2	1.26E-3
5.00E-2	1.33E-3
6.00E-2	1.40E-3
7.00E-2	1.49E-3
8.00E-2	1.60E-3
1.00E-1	1.87E-3
1.50E-1	2.69E-3
2.00E-1	3.60E-3
3.00E-1	5.44E-3
4.00E-1	7.20E-3
5.00E-1	8.89E-3
5.11E-1	9.07E-3
6.00E-1	1.05E-2
6.62E-1	1.14E-2
8.00E-1	1.34E-2
1.00E+0	1.62E-2
1.12E+0	1.76E-2
1.33E+0	2.01E-2
1.50E+0	2.20E-2
2.00E+0	2.69E-2
3.00E+0	3.51E-2
4.00E+0	4.21E-2
5.00E+0	4.82E-2
6.00E+0	5.40E-2
6.13E+0	5.47E-2
8.00E+0	6.70E-2
1.00E+1	7.92E-2
1.50E+1	1.09E-1
2.00E+1	1.38E-1
3.00E+1	1.85E-1
4.00E+1	2.23E-1
5.00E+1	2.60E-1
6.00E+1	2.95E-1
8.00E+1	3.52E-1
1.00E+2	3.96E-1
1.50E+2	4.68E-1
2.00E+2	5.15E-1
3.00E+2	5.80E-1
4.00E+2	6.19E-1
5.00E+2	6.48E-1
6.00E+2	6.70E-1
8.00E+2	7.02E-1
1.00E+3	7.24E-1
1.50E+3	7.63E-1
2.00E+3	7.92E-1
3.00E+3	8.35E-1
4.00E+3	8.75E-1
5.00E+3	9.04E-1
6.00E+3	9.29E-1
8.00E+3	9.65E-1
1.00E+4	9.94E-1

Table A.2: Photon fluence to dose conversion factors

Appendix B

Input materials

The following is the list of the all the materials used in the MCNP input files, with their detailed elemental composition. Each table represents a different material whose name is reported in the table header, along with the mass density used in units of g/cm^3. The subsequent lines in any table give information about a specific isotope that composes the given material, with its atomic fraction. It is intended that, for those element for which the mass number is not given explicitly, the natural atomic abundance is considered.

When available, the cross sections libraries from ENDF-VII dataset ([63]) were used, in compliance with the instruction given in [15].

Lead 11.34 g/cm^3	
Pb-204	1.420×10^{-2}
Pb-206	2.444×10^{-1}
Pb-207	2.241×10^{-1}
Pb-208	5.314×10^{-1}

Borofloat 2.23 g/cm^3	
B-10	8.541×10^{-3}
B-11	3.416×10^{-2}
Na-23	9.011×10^{-3}
Al-27	3.645×10^{-3}
Si-28	1.559×10^{-1}
Si-29	7.946×10^{-3}
Si-30	5.241×10^{-3}
S-32	7.355×10^{-1}
S-33	5.807×10^{-3}
S-34	3.291×10^{-2}
S-36	7.743×10^{-4}

CastIron 7.03049 g/cm^3	
C	7.627×10^{-2}
Si-28	6.165×10^{-2}
Mn-55	4.629×10^{-3}
Fe-54	5.025×10^{-2}
Fe-56	7.890×10^{-1}
Fe-57	1.823×10^{-2}

Borated Concrete 3.0942 g/cm^3	
H	1.237×10^{0}
B-10	9.226×10^{-1}
B-11	3.690×10^{0}
C-12	1.018×10^{-1}
O-16	4.049×10^{0}
Al-27	1.658×10^{-1}
Si-28	1.487×10^{0}
Ca-40	1.695×10^{-1}
Ca-44	5.242×10^{-3}

Nickel 8.90043 g/cm^3	
Ni-58	6.808×10^{-1}
Ni-60	2.622×10^{-1}
Ni-61	1.140×10^{-2}
Ni-62	3.634×10^{-2}
Ni-64	9.256×10^{-3}

Aluminium 2.64651 g/cm^3	
Al-27	9.340×10^{-1}
Mg-24	3.555×10^{-2}
Mg-25	4.501×10^{-3}
Mg-26	4.955×10^{-3}
Si-28	3.727×10^{-3}
Ti-48	1.494×10^{-3}
Cr-52	1.340×10^{-3}
Cr-53	1.717×10^{-4}
Mn-55	7.007×10^{-3}
Fe-56	3.675×10^{-3}

K-39	1.226×10^{-3}
K-40	1.578×10^{-7}
K-41	8.851×10^{-5}

Heavy concrete 3.848 g/cm^3	
H-1	1.022×10^{-1}
H-2	1.534×10^{-5}
O-16	5.569×10^{-1}
O-17	2.233×10^{-4}
Na-23	1.165×10^{-4}
Mg	2.368×10^{-3}
Al-27	5.507×10^{-3}
Si-28	1.921×10^{-2}
P-31	8.644×10^{-5}
S	9.185×10^{-4}
K	1.370×10^{-4}
Ca	2.796×10^{-2}
Ti	2.992×10^{-3}
Mn-55	4.386×10^{-4}
Fe-54	1.635×10^{-2}
Fe-56	2.578×10^{-1}
Fe-57	5.898×10^{-3}
Fe-58	7.864×10^{-4}

Tungsten 19.413 g/cm^3	
W-182	3.709×10^{-1}
W-183	2.003×10^{-1}
W-184	4.288×10^{-1}

Lead+Antimony 11.34 g/cm^3	
Sb-121	6.865×10^{-3}
Sb-123	5.135×10^{-3}
Pb-204	1.383×10^{-2}
Pb-206	2.381×10^{-1}
Pb-207	2.183×10^{-1}
Pb-208	5.177×10^{-1}

Nickel-Titanium 3.0942 g/cm^3	
Ti	3.829×10^{-1}
Ni	6.171×10^{-1}
Fe-54	1.805×10^{-3}
Fe-56	2.831×10^{-2}
Fe-57	6.542×10^{-4}
Fe-58	8.640×10^{-5}
Ti	3.829×10^{-1}
Ni	6.171×10^{-1}

Steel71 7.9995 g/cm^3	
C	1.200×10^{-3}
Si-28	3.500×10^{-3}
Cr	2.000×10^{-3}
Mn-55	6.000×10^{-3}
Fe-54	5.742×10^{-2}
Fe-56	9.013×10^{-1}
Fe-57	2.081×10^{-2}
Fe-58	2.770×10^{-3}
Ni-58	2.042×10^{-3}
Ni-60	7.867×10^{-4}
Ni-61	3.417×10^{-5}
Ni-62	1.090×10^{-4}
Ni-64	2.775×10^{-5}
Cu-63	1.383×10^{-3}
Cu-65	6.166×10^{-4}

Copper 8.91001 g/cm^3	
Cu-63	6.915×10^{-1}
Cu-65	3.085×10^{-1}

B_4C 2.50608 g/cm^3	
B-10	1.592×10^{-1}
B-11	6.408×10^{-1}
C	2.000×10^{-1}

Concrete 2.33578 g/cm^3	
H-1	1.036×10^{-1}
H-2	1.554×10^{-5}
O-16	5.848×10^{-1}
Na-23	1.397×10^{-2}
Mg	1.983×10^{-3}
Al-27	3.185×10^{-2}
Si-28	2.108×10^{-1}
Fe-57	8.587×10^{-5}
Cu-63	6.870×10^{-4}
Cu-65	3.435×10^{-4}
Zn	2.490×10^{-3}

ChipIRSteel 7.79997 g/cm^3	
B-10	4.083×10^{-5}
B-11	1.643×10^{-4}
C	5.540×10^{-3}
N-14	3.564×10^{-4}
Al-27	2.569×10^{-3}
Si-28	1.974×10^{-3}
Mn-55	4.038×10^{-3}
P-31	8.952×10^{-4}
S-32	6.567×10^{-4}
S-33	5.257×10^{-6}
S-34	2.968×10^{-5}
S-36	1.383×10^{-7}
Fe-54	5.724×10^{-2}
Fe-56	8.986×10^{-1}
Fe-57	2.075×10^{-2}
Fe-58	2.762×10^{-3}
Co-59	1.882×10^{-4}
Cu-63	9.054×10^{-4}
Cu-65	4.036×10^{-4}
Ni-58	6.433×10^{-4}
Ni-60	2.478×10^{-4}
Ni-61	1.076×10^{-5}
Ni-62	3.434×10^{-5}
Ni-64	8.741×10^{-6}
Cr-50	4.634×10^{-5}
Cr-52	8.936×10^{-4}
Cr-53	1.013×10^{-4}
Cr-54	2.522×10^{-5}
Mo-92	8.578×10^{-5}
Mo-94	5.347×10^{-5}
Mo-95	9.203×10^{-5}
Mo-96	9.642×10^{-5}
Mo-97	5.520×10^{-5}
Mo-98	1.395×10^{-4}
Mo-100	5.567×10^{-5}
Nb-93	5.969×10^{-5}
V-51	1.089×10^{-4}
Sn-112	4.791×10^{-7}

Stainless304	
7.967 g/cm^3	
C	3.626×10^{-3}
Si-28	1.938×10^{-2}
P-31	7.910×10^{-4}
S-32	5.093×10^{-4}
Cr	1.989×10^{-1}
Mn-55	1.982×10^{-2}
Fe-54	3.846×10^{-2}
Fe-56	6.083×10^{-1}
Fe-57	1.459×10^{-2}
Co-59	2.792×10^{-3}
Ni	9.276×10^{-2}
S-32	7.514×10^{-4}
K	9.244×10^{-3}
Ca	3.888×10^{-2}
Fe-54	2.461×10^{-4}
Fe-56	3.825×10^{-3}
Fe-57	8.758×10^{-5}
Fe-58	1.168×10^{-5}
Silicon	
2.33021 g/cm^3	
Si-28	9.223×10^{-1}
Si-29	4.683×10^{-2}
Si-30	3.083×10^{-2}
Sn-114	3.260×10^{-7}
Sn-115	1.679×10^{-7}
Sn-116	7.181×10^{-6}
Sn-117	3.793×10^{-6}
Sn-118	1.196×10^{-5}
Sn-119	4.242×10^{-6}
Sn-120	1.609×10^{-5}
Sn-122	2.287×10^{-6}
Ti-46	9.558×10^{-6}
Ti-47	8.619×10^{-6}
Ti-48	8.541×10^{-5}
Ti-49	6.268×10^{-6}
Ti-50	6.001×10^{-6}

List of Acronyms

CNR	Consiglio Nazionale delle Ricerche
ENDF	Evaluated Nuclear Data File
ESS	European Spallation Source
FOC	Frame Overlap Chopper
HDPE	High-Density PolyEthylene
HOPG	Highly Oriented Pyrolytic Graphite
ICRP	International Commission Radiological Protection
LIFO	Last In, First Out
MCNP	Monte Carlo N-Particle
NBEX	Neutron Beam Extraction
NBOA	Neutron Beam Optic Assembly
PSC	Pulse Shaping Choppers
sFOC	Sub-Frame Overlap Chopper
STFC	Science and Technology Facilities Council
TMRA	Target Monolith Reflector Assembly
VESPA	Vibrational Excitation Spectrometer using Pyrolytic-graphite Analyser
WFM	Wavelength Frame Multiplication

List of Figures

1.1 A uniformly generated random number selects the type of event that takes place, according to where its value lies in a unit line. 6
1.2 Sketch of a generic probability density function used in Monte Carlo simulations. 11
1.3 Sketch of the weight window technique. 17
1.4 Fluence to effective dose conversion functions for neutrons (a) and gammas (b). 20

2.1 Top view of the preliminary layout for the ESS facility. 23
2.2 Main phases of the construction plan of ESS. 23
2.3 Detail of the target wheel showing the disposition of the tungsten bricks [23]. 24
2.4 The butterfly moderator on the left and its location respect to the target wheel on the right [25]. 25
2.5 General layout (a) and a cut section (b) of the monolith. . . . 26
2.6 View of the TMRA and the beam-ports in the monolith. . . . 27
2.7 Top-view of ESS monolith. 27
2.8 Layout of a representative NBEX [27]. 28
2.9 Top-view of ESS bunker. 29
2.10 Top-view of ESS, showing the bunker, the instrument halls, the 16 instruments under construction and their relative disposition respect to the proton beam. 29
2.11 Possible layout of an instrument in the West sector 30

3.1 VESPA layout [31]. 33
3.2 Schematic drawing of VESPA beam-line axis that shows its direction respect to the proton beam axis and the E7 beam-port axis. The tilt of $0.9\,^{\circ}$ is about the green dot, which is at about $\sim 1\,\mathrm{m}$ from the moderator centre. Hence, the two angles of $66\,^{\circ}$ and $65.1\,^{\circ}$ do not share the same vertex [36]. . . 33
3.3 Schematic representation of the elliptical profile of the guide on the horizontal plane. 34

3.4 Layout of VESPA instrument showing the positions of its main components [33]. 34
3.5 Engineering design of VESPA inside the bunker [38]. 35
3.6 Size of the NBOA entrance and exit in the monolith [39]. . . 35
3.7 Design of the triple of double-disc PSCs inside the bunker. . . 36
3.8 (a) Current design for the hutch, cave and sample preparation area of VESPA [31]. (b) Concept design VESPA lower experimental cave, showing the Secondary Spectrometer and the sample insert from the upper cave [43]. 38
3.9 Overview (a) and a vertical section (b) of the Secondary Spectrometer. It is constituted of two symmetrical halves, each consisting of 6 diffraction modules and 7 vibrational spectrometer modules, one of which is shown in (c) [43]. 39
3.10 Top-views of VESPA MCNP model (a) and a detail of the area inside the bunker (b), from the dedicated branch of CombLayer [47]. 40
3.11 Side-view (a), Top-view (b) and a detail (c) of the first section of the MCNP model of VESPA, used for performing the calculations presented in this thesis. 42
3.12 Comparison between the engineering model (a, c) and the MCNP model (b, d) of the first triplet of choppers of VESPA inside the bunker. 43

4.1 The full suite of beam-lines for which ESS calculated the source terms. VESPA is not in that list, but it is added for reference. 46
4.2 MCNP model of the TMRA showing the position of ESS source term for a representative beam-line [51]. 46
4.3 The solid angle about a line parallel to the beam-line axis is subdivided into concentric cones. 47
4.4 Probability density function used for sampling the emission angle from the primary source term. 49
4.5 The neutron spectra used for sampling the initial energy of neutrons generated by the primary neutron source term. . . . 49
4.6 Neutron spectra in lethargy units produced by the primary source and the proton source, at 5.5 m from the monolith centre. 51
4.7 Graphs of the quantity ξ as a function of x when the sum of equation 4.5 is performed over all energies (a) and for energies above 1 eV (b). 53
4.8 Benchmark spectra of figure 4.6 on which a third curve in red is superimposed, which represent the spectrum calculated by the primary source term after being rescaled by $x = 0.9$ (a) and by $x = 1.13$ (b). 54

4.9 Sketch of the first section of VESPA beam-line showing the angular opening of the primary source term. 55
4.10 The angular distributions for the candidates source terms at the bunker wall exit (15 m) with a coarse binning (a), at the bunker wall exit (15 m) with a fine binning (b) and at the bunker wall entrance (11.5 m) with a fine binning (c). 58
4.11 Neutron spectra for the candidates sources at the bunker wall exit with a coarse binning (a), at the bunker wall exit with a fine binning (b) and at the bunker wall entrance with a fine binning (c). 59
4.12 The refined angular distributions for the candidates source terms at the bunker wall exit (15 m) with a coarse binning (a), at the bunker wall exit (15 m) with a fine binning (b) and at the bunker wall entrance (11.5 m) with a fine binning (c). 62
4.13 The six positions used for benchmarking the candidate secondary source terms with the primary source term. 63
4.14 Benchmark spectra for the candidate secondary sources at the bunker wall exit with a coarse binning (a), at the bunker wall exit with a fine binning (b) and at the bunker wall entrance with a fine binning (c). 64
4.15 Graphs of the quantities $\xi^{src,pos}$ as a function of $x^{src,pos}$ for the source at the bunker wall exit with a coarse binning (a), at the bunker wall exit with a fine binning (b) and at the bunker wall entrance with a fine binning (c). 65
4.16 Graphs of the minima $x^{src,pos}$ as functions of the positions along the beamline (a) and in the second chopper pit (b). . . 66
4.17 Gamma flux spectrum taken at 2 m from the moderator centre, on the surface area of VESPA primary source. 67
4.18 Top-view of the gamma dose rate map due to monochromatic gamma source of 10 MeV at the entrance of the bunker wall. The image shows one of the shielding geometry used in the Common Shielding project, later introduced in this thesis. . . 68

5.1 Engineering drawings of the preliminary shielding design of the guide section (a) and the chopper pit (b) in the short sector halls [60, 61]. 71
5.2 Engineering drawing of the guide shielding [62] showing the relevant geometrical parameters, with a detailed view of the region around the guide on the left. This picture is a vertical section of what is shown in figure 5.1(a). 72
5.3 Preliminary model top-view (a) and side-view (b) of the neutron dose rate map with a 60 cm thick concrete layer. 72

5.4 Preliminary model top-view (a) and side-view (b) of the photon dose rate map with a 60 cm thick concrete layer. 73
5.5 Preliminary model top-view (a) and side-view (b) of the neutron dose rate map with a 70 cm thick concrete layer. 73
5.6 Preliminary model top-view (a) and side-view (b) of the photon dose rate map with a 70 cm thick concrete layer. 74
5.7 Preliminary model top-view (a) and side-view (b) of the neutron dose rate map with a 80 cm thick concrete layer. 74
5.8 Preliminary model top-view (a) and side-view (b) of the photon dose rate map with a 80 cm thick concrete layer. 75
5.9 Preliminary model top-view (a) and side-view (b) of the neutron dose rate map with a 90 cm thick concrete layer. 75
5.10 Preliminary model top-view (a) and side-view (b) of the photon dose rate map with a 90 cm thick concrete layer. 76
5.11 Front-view of the preliminary Common Shielding model (a) and the definitive Common Shielding model (b) in MCNP, at 35 m from the bunker wall. 77
5.12 Common Shielding model top-view (a) and side-view (b) of the neutron dose rate map with a 60 cm thick concrete layer. 77
5.13 Common Shielding model top-view (a) and side-view (b) of the photon dose rate map with a 60 cm thick concrete layer. . 78
5.14 Common Shielding model top-view (a) and side-view (b) of the neutron dose rate map with a 70 cm thick concrete layer. 78
5.15 Common Shielding model top-view (a) and side-view (b) of the photon dose rate map with a 70 cm thick concrete layer. . 79
5.16 Common Shielding model top-view (a) and side-view (b) of the neutron dose rate map with a 80 cm thick concrete layer. 79
5.17 Common Shielding model top-view (a) and side-view (b) of the photon dose rate map with a 80 cm thick concrete layer. . 80
5.18 Common Shielding model top-view (a) and side-view (b) of the neutron dose rate map with a 90 cm thick concrete layer. 80
5.19 Common Shielding model top-view (a) and side-view (b) of the photon dose rate map with a 90 cm thick concrete layer. . 81
5.20 Common Shielding model front-view of the neutron dose rate taken at 1580 cm. 81
5.21 Common Shielding model (without the borated layer) top-view (a) and side-view (b) of the neutron dose rate map with a 60 cm thick concrete layer. 83
5.22 Common Shielding model (without the borated layer) top-view (a) and side-view (b) of the photon dose rate map with a 60 cm thick concrete layer. 83
5.23 Common Shielding model (without the borated layer) top-view (a) and side-view (b) of the neutron dose rate map with a 70 cm thick concrete layer. 84

5.24 Common Shielding model (without the borated layer) top-view (a) and side-view (b) of the photon dose rate map with a 70 cm thick concrete layer. 84
5.25 Common Shielding model (without the borated layer) top-view (a) and side-view (b) of the neutron dose rate map with a 80 cm thick concrete layer. 85
5.26 Common Shielding model (without the borated layer) top-view (a) and side-view (b) of the photon dose rate map with a 80 cm thick concrete layer. 85
5.27 Common Shielding model (without the borated layer) top-view (a) and side-view (b) of the neutron dose rate map with a 90 cm thick concrete layer. 86
5.28 Common Shielding model (without the borated layer) top-view (a) and side-view (b) of the photon dose rate map with a 90 cm thick concrete layer. 86
5.29 The thermal neutron flux, below 1 eV, crossing the entrance of the sFOC. This spectrum was used to set up a fictive thermal source at the same position. 87
5.30 Side-view of the sFOC chopper in a fully closed configuration in the MCNP model, also showing the position of the fictive thermal neutron source at its entrance. 88
5.31 Neutron (a) and gamma (b) dose maps about the two chopper pits outside the bunker, due to a thermal neutron beam impinging on the blades of the sFOC chopper in a fully closed configuration. 88
5.32 *m*-value profile of VESPA guide out of the bunker. 90
5.33 Top-view (a) and associated relative error map (b) of the neutron dose rate map for the tapered shielding with the borated concrete layer. 91
5.34 Side-view (a) and associated relative error map (b) of the neutron dose rate map for the tapered shielding with the borated concrete layer. 91
5.35 Top-view (a) and associated relative error map (b) of the photon dose rate map for the tapered shielding with the borated concrete layer. 92
5.36 Side-view (a) and associated relative error map (b) of the photon dose rate map for the tapered shielding with the borated concrete layer. 92
5.37 Top-view (a) and associated relative error map (b) of the neutron dose rate map for the tapered shielding without the borated concrete layer. 93
5.38 Side-view (a) and associated relative error map (b) of the neutron dose rate map for the tapered shielding without the borated concrete layer. 93

5.39 Top-view (a) and associated relative error map (b) of the photon dose rate map for the tapered shielding without the borated concrete layer. 94
5.40 Side-view (a) and associated relative error map (b) of the photon dose rate map for the tapered shielding without the borated concrete layer. 94
5.41 Top-view (a) and side-view (b) of the neutron dose rate map with a 70 cm thick heavy concrete layer. 96
5.42 Top-view (a) and side-view (b) of the photon dose rate map with a 70 cm thick heavy concrete layer. 96
5.43 Top-view (a) and front-view (b) of the geometrical model used for studying the gaps between the guide pieces. 98
5.44 Neutron spectrum used to set the source for studying the effects of the guide gaps. 99
5.45 Integral neutron flux map with (a) and without (b) the borated concrete layer. 100
5.46 Integral photon flux map with (a) and without (b) the borated concrete layer. 100
5.47 Neutron flux at the steel piece, with and without the borated concrete layer. 101
5.48 Dose rate maps due to the gammas emitted from the activated steel piece, with (a) and without (b) the borated concrete layer. 101
5.49 The residual activity of the steel slab at different cumulative time steps after 5400 h of irradiation. 102

6.1 Neutron spectra transmitted after penetrating a 25 cm thick bulk of several materials. 106
6.2 Top-view of the heavy-shutter design investigated for VESPA. 106
6.3 Neutron dose rates at the bunker wall exit, due to heavy-shutters with different thickness of copper. 108
6.4 Top-view of the neutron (a) and photon (b) dose rate maps due to a 85 cm long heavy-shutter. White lines are iso-dose lines set at 1.5 μSv/h. 109

A.1 Fluence to effective dose functions for neutrons and gammas. 112

List of Tables

2.1 Main ESS parameters. 24

4.1 LOKI source terms calculated by ESS. 48
4.2 The two angular binning investigated for calculating the secondary source term. 56

5.1 Proposed ordinary concrete thickness for the guide shielding of VESPA. 90
5.2 Ni-Ti layer thickness as a function of the m value. 90

A.1 Neutron fluence to dose conversion factors. 113
A.2 Photon fluence to dose conversion factors 114

Bibliography

[1] G. Knoll, *Radiation Detection and Measurement.* Wiley, 2000.

[2] E. Lewis and W. J. Miller, *Computational methods of neutron transport.* 1984.

[3] A. Haghighat, *Monte Carlo methods for particle transport.* CRC Press, 2015.

[4] "A General Monte Carlo N-Particle (MCNP) Transport Code." `https://mcnp.lanl.gov/`.

[5] Los Alamos National Laboratory, *MCNP Users Manual - Code Version 6.2*, 2017.

[6] N. Petoussi-Henss *et al.*, "Conversion coefficients for radiological protection quantities for external radiation exposures," *Annals of the ICRP*, vol. 40, no. 2-5, pp. 1–257, 2010.

[7] F. Attix, *Introduction to Radiological Physics and Radiation Dosimetry*, ch. 2. A Wiley-Interscience publication, Wiley, 1986.

[8] X-5 Monte Carlo Team, *MCNP — A General Monte Carlo N-Particle Transport Code, Version 5*, 2008.

[9] M. DeGroot and M. Schervish, *Probability and Statistics (4th Edition).* Pearson, 2011.

[10] J. Taylor, *Introduzione all'analisi degli errori. Lo studio delle incertezze nelle misure fisiche.* Collana di fisica. Testi e manuali, Zanichelli, 1986.

[11] J. Shultis and R. Faw, *An MCNP primer.*

[12] X-5 Monte Carlo Team, *MCNP — A General Monte Carlo N-Particle Transport Code, Version 5*, ch. 2. Los Alamos National Laboratories, 2005.

[13] J. Hendricks and R. Schwarz, "MCNP6 intermediate workshop." 2018.

[14] J. Spencer *et al.*, “Weight window based variance reduction introduction & overview,” 5 2018.

[15] G. Muhrer and F. Javier, “ESS procedure for designing shielding for safety,” tech. rep. Internal ESS document.

[16] G. Muhrer and F. Javier, “Definition of Supervised and Controlled Radiation Areas,” tech. rep., European Spallation Source. Internal ESS document.

[17] F. Zoë and M. Hartl, “NSS zoning document - part I (safety),” tech. rep., European Spallation Source. Internal ESS document.

[18] ESS, “ESS website.” `https://europeanspallationsource.se/`.

[19] C. Vettier *et al.*, “Progress for the European Spallation Source in Scandinavia,” *Nuclear Instruments and Methods in Physics Research Section A: Accelerators, Spectrometers, Detectors and Associated Equipment*, vol. 600, no. 1, pp. 8–9, 2009.

[20] L. Zanini *et al.*, “The neutron moderators for the European Spallation Source,” *Journal of Physics: Conference Series*, vol. 1021, p. 012066, 05 2018.

[21] S. Peggs, “ESS Technical Design Report,” 2013.

[22] R. Costa, “Preliminary Safety Analysis Report (PSAR),” tech. rep., European Spallation Source. Internal ESS document.

[23] R. Linander, “The ESS target design and beam raster system,” february 2017.

[24] D. Filges and F. Goldenbaum, *Handbook of Spallation Research: Theory, Experiments and Applications.* 2010.

[25] F. X. Gallmeier, “Overall efficiency of neutron sources.” `https://slideplayer.com/slide/12966590/`, February 2016.

[26] G. Scionti, “Neutronic design for an irradiation module at ESS for fusion and industrial material studies,” Master’s thesis, 2015.

[27] B. Jönsson, “Neutron beam extraction (NBEX),” january 2018.

[28] L. Zanini *et al.*, “Neutronic design of the bunker wall and roof,” tech. rep., European Spallation Source. Internal ESS document.

[29] ESS, “VESPA main page at ESS.” `https://europeanspallationsource.se/instruments/vespa`.

[30] M. Zanetti *et al.*, “Neutronic developments on TOSCA and VESPA: Progress to date,” *Physica B: Condensed Matter*, vol. 562, pp. 107 – 111, 2019.

[31] D. Colognesi *et al.*, “Concepts of Operations for the VESPA Instrument,” tech. rep., European Spallation Source. Internal ESS document.

[32] A. Fedrigo *et al.*, “VESPA: The vibrational spectrometer for the european spallation source,” *Review of Scientific Instruments*, vol. 87, p. 065101, 06 2016.

[33] C. Lopez, “VESPA choppers,” tech. rep., European Spallation Source. Internal ESS document.

[34] L. del Rosso. Private communication, 2019.

[35] V. team, “ESS Instrument Construction Proposal - VESPA,” tech. rep., European Spallation Source, april 2015. Internal ESS document.

[36] D. Colognesi *et al.*, “Preliminary System Design Description for the VESPA instrument,” tech. rep., European Spallation Source. Internal ESS document.

[37] L. del Rosso, “Report on the optics refinement,” tech. rep., june 2019. Internal VESPA document.

[38] F. Masi. Private communication, 2019.

[39] M. Chowdhury, “VESPA neutron guide NBOA specification,” tech. rep., Science & Technology Facilities Council Rutherford Appleton Laboratory. Internal ISIS document.

[40] L. D. Fresco. Private communication, 2019.

[41] G. Laszlo, “Heavy-shutter Statement of Work,” tech. rep. Internal ESS document.

[42] D. Colognesi, “System requirements specification for the VESPA instrument,” tech. rep., European Spallation Source. Internal ESS document.

[43] M. Zanetti, “VESPA Secondary Spectrometer & Block House.” Internal VESPA document, November 2018.

[44] H. Tsige-Tamirat *et al.*, “Use of McCad for the conversion of ITER CAD data to MCNP geometry,” *Fusion Engineering and Design*, vol. 83, no. 10, pp. 1771 – 1773, 2008. Proceedings of the Eight International Symposium of Fusion Nuclear Technology.

[45] S. Ansell, “CombLayer github repository.” `https://github.com/SAnsell/CombLayer`.

[46] S. Ansell, "CombLayer - A fast parametric MCNP(X) model constructor," in *JAEA-Conf–2015-002*, (Japan), pp. 148–154, 2016.

[47] G. Scionti, "VESPA branch of CombLayer github repository." `https://github.com/SAnsell/CombLayer/tree/Vespa`.

[48] N. Cherkashyna *et al.*, "NOSG phase 2 guidelines for designing instrument shielding for radiation safety," tech. rep., European Spallation Source. Internal ESS document.

[49] F. X. Gallmeier *et al.*, "Neutron beam-line shielding calculations at the SNS," *Nuclear Instruments and Methods in Physics Research Section A: Accelerators, Spectrometers, Detectors and Associated Equipment*, vol. 562, no. 2, pp. 946 – 949, 2006. Proceedings of the 7th International Conference on Accelerator Applications.

[50] T. Liang *et al.*, "Monte Carlo shielding evaluation of a CSNS Multi-Physics instrument," *Nuclear Engineering and Technology*, 2019.

[51] V. Santoro *et al.*, "Source term for shielding of bunker and beam-lines at ESS," tech. rep., European Spallation Source. Internal ESS document.

[52] F. X. Gallmeier, "Source terms for neutron beam line shielding and activation calculations," 2005.

[53] V. Santoro. Private communication, 2019.

[54] V. Santoro, "Status of neutronics calculations for the common shielding project." Presentation during IKON 18, February 2020.

[55] ESS, "Common Shielding Project - Preliminary Design Review." `https://indico.esss.lu.se/event/1183/`.

[56] M. Harada *et al.*, "Shielding design of a neutron beam line ""NOBORU"" at JSNS/J-PARC," *Pro Nucl Sci Techn*, vol. 1, pp. 94–97, 2011.

[57] I. Popova *et al.*, "Shielding analyses for VISION beam line at SNS," *Progress in Nuclear Science and Technology*, vol. 4, pp. 178–181, 2014.

[58] N. Fomin *et al.*, "Fundamental neutron physics beam-line at the spallation neutron source at ornl," *Nuclear Instruments and Methods in Physics Research Section A: Accelerators, Spectrometers, Detectors and Associated Equipment*, vol. 773, pp. 45–51, 2015.

[59] D. D. DiJulio *et al.*, "A polyethylene-B_4C based concrete for enhanced neutron shielding at neutron research facilities," *Nuclear Instruments and Methods in Physics Research Section A: Accelerators, Spectrometers, Detectors and Associated Equipment*, vol. 859, pp. 41–46, 2017.

[60] S. Kudumovic, "Standard Shielding Neutronics Kick-0ff." `https://indico.esss.lu.se/event/1094/`.

[61] S. Kudumovic, "Preliminary Design Report - Common Shielding Project," tech. rep., European Spallation Source. Internal ESS document.

[62] S. Kenad. Internal ESS document.

[63] "Evaluated Nuclear Data File (ENDF)." `http://www.nndc.bnl.gov/exfor/endf00.jsp`.

[64] A. Monterrosa *et al.*, "Boron Use and Control in PWRs and FHRs," *Department of Nuclear Engineering, UC Berkeley, Report UCBTH-12-007*, 2012.

[65] International Atomic Energy Agency, *Database of prompt gamma rays from slow neutron capture for elemental analysis*. International Atomic Energy Agency, 2007.

[66] F. Mezei, "Novel polarized neutron devices: supermirror and spin component amplifier," *Communications on Physics (London)*, vol. 1, no. 3, pp. 81–85, 1976.

[67] C. Cooper-Jensen *et al.*, ""m = 1" coatings for neutron guides," in *Journal of Physics: Conference Series*, vol. 528, p. 012005, IOP Publishing, 2014.

[68] Z. Zhang, P. Lei, J. Zhu, X. Wang, and Z. Wang, "Ni/ti multilayer supermirrors for neutron optics,"

[69] R. Kolevatov *et al.*, "Neutron absorption in supermirror coatings: Effects on shielding," *Nuclear Instruments and Methods in Physics Research Section A: Accelerators, Spectrometers, Detectors and Associated Equipment*, vol. 922, pp. 98 – 107, 2019.

[70] E. Klinkby *et al.*, "Interfacing MCNPX and McStas for simulation of neutron transport," *Nuclear Instruments and Methods in Physics Research Section A: Accelerators, Spectrometers, Detectors and Associated Equipment*, vol. 700, pp. 106–110, 2013.

[71] K. Lefmann *et al.*, "McStas, a general software package for neutron ray-tracing simulations," *Neutron news*, vol. 10, no. 3, pp. 20–23, 1999.

[72] F. X. Gallmeier *et al.*, "Implementation of neutron mirror modeling capability into MCNPX and its demonstration in first applications," *Nuclear Technology*, vol. 168, no. 3, pp. 768–772, 2009.

[73] M. Magan, "Detailed Supermirror physics in MCNP6," October 2019.

[74] M. Magan *et al.*, “Ms. Ref. No.: NIMA-D-19-00551R1: Supermirror physics with event biasing in MCNP6,” *Nuclear Instruments and Methods in Physics Research Section A*. Currently under review.

[75] K. Andersen. Private communication with VESPA team, November 2019.

[76] O. Koichi *et al.*, “Development of Novel Neutron Shielding Concrete,” *Nuclear Technology*, vol. 168, no. 2, pp. 545–552, 2009.

[77] I. I. Bashter, “Calculation of radiation attenuation coefficients for shielding concretes,” *Annals of nuclear Energy*, vol. 24, no. 17, pp. 1389–1401, 1997.

[78] F. X. Gallmeier *et al.*, “Neutron beam-line shielding calculations at the SNS,” *Nuclear Instruments and Methods in Physics Research Section A: Accelerators, Spectrometers, Detectors and Associated Equipment*, vol. 562, no. 2, pp. 946–949, 2006.

[79] G. Aprigliano. Private communication, September 2019.

[80] L. del Rosso, “Guide geometry - summary datafile,” tech. rep., 2019. Internal VESPA document.

[81] N. E. Agency, “IAEA web-page for ADVANTG.”
`https://www.oecd-nea.org/tools/abstract/detail/ccc-0831/`.

[82] F. X. Gallmeier *et al.*, “The CINDER’90 transmutation code package for use in accelerator applications in combination with MCNPX,” tech. rep., Oak Ridge National Lab.(ORNL), Oak Ridge, TN (United States). Spallation . . . , 2010.

[83] Centers for Disease Control and Prevention, “Radioisotope Brief: Cobalt-60.”
`https://www.cdc.gov/nceh/radiation/emergencies/isotopes/cobalt.htm#content`.

[84] United States Environmental Protection Agency, “Radionuclide Basics: Cobalt-60.”
`http://nucleardata.nuclear.lu.se/toi/`.

[85] S. Chu *et al.*, “The Lund/LBNL Nuclear Data Search.”
`https://www.epa.gov/radiation/radionuclide-basics-cobalt-60`.

[86] A. Sullivan, *A Guide to Radiation and Radioactivity Levels Near High Energy Particle Accelerators*. Nuclear Technology Publishing, 1992.

[87] V. Santoro, “Heavy Shutter, Bunker insert and neutronics for the test beam line.” Presentation during IKON 13, September 2017.

[88] M. J. Whiteley and P. Wei-Ping, “A study of the flammability of chlorinated polyethylene under pyrolysis conditions,” *Thermochimica Acta*, vol. 166, pp. 27–39, 1990.

[89] V. Santoro *et al.*, “Study of neutron shielding collimators for curved beam-lines at the European Spallation Source,” in *Journal of Physics: Conference Series*, vol. 1046 of *Journal of Physics: Conference Series*, IOP Publishing, 6 2018.

Acknowledgements

The doctorate has been a unique experience, one of those that will leave its traces in my life forever. I couldn't have imagined that I would have reached this in my life. I had to dramatically change my being for becoming a PhD student. I had to pack all my stuff, make them fit in a single hand luggage and start travelling.

It's been a very long journey.

Now that it has come to an end, I realize that my inner strength was not enough to bear it on its own. Thankfully, I've always found the way to get back on my feet. There are a lot of people that I have to thank for that, people that I met during this long journey. Maybe they will never truly realize what they did for me. Simply having them at my side some now and them, or getting a even a quick smile gave me the strength I needed.

Agneta Carlekrantz
Alfonso Policicchio
Andrea Smeriglio
Antonio Bianchi
Antonio De Bonis
Antonio Palamara
Antonio Sannia
Barbara Belmonte
Beate Linnenberg
Bengt Jönsson
Bogdan Cadar
Carlo Poselle Bonaventura
Caroline Prabert
Carmen Vaccaro
Cecilia Maiano
Chiara Perri
Clara Ines Lopez
Claudia Scatigno
Dalila Onorati
Daniele Colognesi
Davide Micieli
Enrica Barrilli
Eugenio Abritta
Federico Malara
Federico Masi
Francesca Bax
Francesco Colao
Francesco Valentino
Giovanni Borrello
Giovanni Giacobino
Giovanni Murrone
Giuseppe Aprigliano
Giuseppe Conte
Giuseppe Gorini
Giuseppe Nicoletta
Inga Tejedor
Inger Hallström
Inglis Persson
Ioan Sandu
John Hendricks
Karin Vandenbor
Ken Andersen

Konstantin Batkov
Laura Longo
Leonardo del Rosso
Lorenzo Di Fresco
Louise Wijkström
Luca Zanini
Luigina Sciommarella
Manuel Bussoli
Marco Turano
Maria Barca
Maria Bisi
Maria Tolf
Marica Rebai
Matteo Zanetti
Max Sokolov
Michela Dell'Anno Boulton
Monika Hartl
Mostafa Jamalipour
Nataliia Cherkashyna
Nicola Montano
Nicolò Borghi
Orazio La Rocca
Oreste De Luca
Per Hallström
Philip Bentley
Pierfrancesco Ulpiani
Raffaele Agostino
Raffaele Filosa
Rasmus Johansson
Riccardo Anfossi
Riccardo Barberi
Riccardo Bevilacqua
Roberta Cattaneo
Roberto Senesi
Rocco Cristofaro
Saeid Pirani
Sara Giannone
Sara Miceli
Sara Stelitano
Sauro Carlotti
Saverio Ardovino
Senad Kudumovic
Sharon Di Spena
Stefano Bellissima
Stefano Dianetti
Steven Lilley
Stuart Ansell
Thomas Miller
Tina Nordqvist
Triestino Minniti
Valentina Santoro
Valentina Stranieri
Valeria Loise
Valerio Scacco
Vincenzo Bellucci
Vincenzo Formoso
Yong Joong Lee
Zvonko Lazic

Thank you for being kind to me.
Thank you for being who you are.
Thank you.